MOLECULAR DYNAMICS SIMULATIONS OF NANOMETER SIZED DEVICES BASED ON CARBON NANOTUBES

By

SUNITA NEGI

Institute for Plasma Research, Bhat, Gandhinagar,

Gujarat, INDIA

A thesis submitted to the

Board of Studies in Physical Sciences

In partial fulfillment of requirements

For the Degree of

DOCTOR OF PHILOSOPHY

of

HOMI BHABHA NATIONAL INSTITUTE

November 2010

Homi Bhabha National Institute

Recommendations of the Viva Voce Board

As members of Viva Voce Board, we certify that we have read the dissertation prepared by "**Sunita Negi**" entitled "**Molecular Dynamics Simulations of nanometer sized devices based on Carbon Nanotubes**" and recommend that it may be accepted as fulfilling the dissertation requirement for the Degree of Doctor of Philosophy.

..... **Date:**

Chairman - Prof. Abhijit Sen
Institute for Plasma Research
Bhat, Gandhinagar, Gujarat - 382428, India

..... **Date:**

Guide - Dr. Shashank Chaturvedi
Bhabha Atomic Research Center
Autonagar, Visakhapatnam - 530012, Andhra Pradesh, India

..... **Date:**

Member 1 - Dr. Manoj Warrier
Bhabha Atomic Research Center
Autonagar, Visakhapatnam - 530012, Andhra Pradesh, India

..... **Date:**

Member 2 - Dr. Daniel Raju
Institute for Plasma Research
Bhat, Gandhinagar, Gujarat - 382428, India

I hereby certify that I have read this dissertation prepared under my direction and recommend that it may be accepted as fulfilling the dissertation requirement.

Guide - Dr. Shashank Chaturvedi
Date: **Place:**

CERTIFICATION FROM GUIDE

This is to certify that the viva voce of **Ms. Sunita Negi** took place on 26th April 2011 in the Institute for Plasma Research, Bhat, Gandhinagar, Gujarat in the presence of all the following doctoral committee members and the external referee **Prof. BALASUBRAMANIAN SUNDARAM**.

Prof. Abhijit Sen (Chairman)

Dr. Shashank Chaturvedi (Guide)

Dr. Manoj Warrier (Member)

Dr. Daniel Raju (Member)

The corrections as indicated in the thesis evaluation report of both the referees, have been incorporated in this copy of the thesis.

(Dr. Shashank Chaturvedi)
Guide

STATEMENT BY AUTHOR

This dissertation has been submitted in partial fulfillment of requirements for an advanced degree at Homi Bhabha National Institute (HBNI) and is deposited in the Library to be made available to borrowers under rules of the HBNI.

Brief quotations from this dissertation are allowable without special permission, provided that accurate acknowledgement of source is made. Requests for permission for extended quotation from or reproduction of this manuscript in whole or in part may be granted by the Competent Authority of HBNI when in his or her judgment the proposed use of the material is in the interests of scholarship. In all other instances, however, permission must be obtained from the author.

Signature of the Candidate

Sunita Negi

DECLARATION

I, Sunita Negi, hereby declare that the investigation presented in the thesis has been carried out by me. The work is original and has not been submitted earlier as a whole or part for a degree/diploma at this or any other Institution/University.

Signature of the Candidate

Sunita Negi

I would like to dedicate this thesis

to my father

Acknowledgments

I would like to express my deep gratitude to my thesis supervisor **Dr. Shashank Chaturvedi** for his constant support and guidance during these years. I am thankful to him for his encouragement to pursue research in the field of computational nanoscience which was a new field for both of us. He always helped me with his invaluable advice. He is a great physicist and a very good mentor. He helped me to understand and solve the physics problems with the numerical methods. I sincerely appreciate his way of thinking and solving the physics problems. He has a very good approach which makes every task, research related or otherwise easier for him. I have learned so much from him, even while I know that I still have to learn a lot more.

I would like to express my humble thanks to Prof. P. K. Kaw, Director of IPR and Prof. Abhijit Sen for giving me this opportunity to carry out this research at IPR and for their extended support through out my thesis work. Next I would like to thank my doctoral committee, HBNI for reviewing my work and giving the necessary guidance. For the same reason I would like to thank Dr. R. Ganesh chairman academic committee and other members of the academic committee and Dr.P.Vasu chairman previous academic committee and other members of the previous committee for their assessment and support.

Special thanks to Dr. Manoj Warrier for his kind assistance. I thank him for giving some very insightful discussions on molecular dynamics method. I appreciate his help while learning some new scientific soft-wares also. He was easily available whenever a discussion was needed.

I acknowledge Dr. R. Ganesh for giving valuable comments in my final review which improved my thesis work and also for becoming the signing authority for me when Dr. Shashank Chaturvedi moved to BARC, Vizag.

Deep appreciation also goes to Dr. Danial Raju for his valuable discussions on data analysis techniques.

I would like to acknowledge Prof. Kai Nordlund for the use for his code HcPar-

Cas. I also thank the reviewers of all our papers, who gave their valuable comments to improve our work.

I would like to extend my gratitude to all my group members who presently constitute the Computational Analysis Division, BARC, Vizag. All of them helped me during my Phd. in some way or the other, specially during my BARC, Vizag visit.

I would like to thank my fellow research scholars as Sharad, Shekar, Jugal, Satya, Puraram, Sita, Prabal, Deepak, Ujjwal, Ashwin, Gurudatt, Tayab, Vikram, Kshitish, Susheel, Sanat, Rameshwar, Pravesh, Manjit, Sayak, Aaditya, Soumen, Illiyas, Vikram (Jr.) for making the research scholar room an exciting place to work. Special thanks to Vikrant, Kishor, Maya and Subhash for their kind support and help during this period. I would also like to thank all my seniors without mentioning the individual names as the list is very long.

I also thank all the IPR library staff members, Computer Centre members and all other members from the administrative staff for making the things easier for me during my stay in IPR.

I am happy to thank my friends Pratibha, Geetanjali, Smita, Sanjeev, Vinay, Himanshu, Mamta, Yashi and Saurabh for their moral support during this period.

Finally I would like to acknowledge my family for showing their constant support always, specially during my Phd. Special thanks to my mother for standing by me always and my brother (Vijay) and my sister-in-law (Shashi) for their love and affection. I also thank my elder sisters Santoshi and Tannu and my brother-in-law Rakesh and Vikash for their moral support. Finally to the little angels of the family Deepak, Ragini, Aditi, Vatsal and Shiven for their love and affection.

Sunita Negi

Gandhinagar

List of Publications

Peer Reviewed Journals:

1. "**Molecular Dynamics Simulations of a Carbon Nanotube interacting with a Graphite surface**",
   S. Negi, M. Warrier, S. Chaturvedi and K. Nordlund, *Journal of Computational and Theoretical Nanoscience* **(5)** (2008) 1-6.

2. "**Molecular Dynamic simulations of a double-walled carbon nanotube motor subjected to a sinusoidally varying electric field**"
   S. Negi, M. Warrier, S. Chaturvedi and K. Nordlund, *Journal of Computational Material Science* **44** (2009) 979-987.

3. "**Normal Mode analysis of a Single Walled Carbon Nanotube based on Molecular Dynamic : A Singular Value Decomposition study**",
   S. Negi and S. Chaturvedi, *International Journal of Nanoscience* **(9)** No. 5 (2010) 1-16.

4. "**Determination of useful parameter space for a double-walled carbon nanotube motor subjected to a sinusoidally varying electric field**",
   S. Negi, M. Warrier and S. Chaturvedi, *Computational Material Science* **(50)** (2010) 761-770.

International Conferences Proceedings:

1. "**Molecular Dynamics Simulations of a Carbon Nanotube interacting with a graphite surface.**",
   S. Negi, M. Warrier, S. Chaturvedi and K. Nordlund, *MESODIS 2006 (International Workshop on the physics of Mesoscopic and Disoredered Materials),*

IITK, Kanpur, India, December 04-08, 2006.

2. "**Molecular Dynamics Simulations of a Carbon nanotube based motor subjected to a sinusoidally varying electric field.**",
   S. Negi, M. Warrier and S. Chaturvedi, *ICANAT 2008, International Conference on Advances in Nanotechnology, Mats University, Raipur, India, November 06-08, 2008.*

3. **Molecular Dynamics Simulations of a Carbon nanotube based motor stimulated by an externally applied sinusoidally varying Electric Field.**,
   S. Negi, M. Warrier and S. Chaturvedi, *Conference on Computational Physics, 23rd - 26th June, 2010, Trondheim, Norway.*

4. **Determination of useful parameter space for a double-walled carbon nanotube based motor subjected to a sinusoidally varying electric field.**,
   S. Negi, M. Warrier and S. Chaturvedi, *International Conferene on Molecular Materials, MOLMAT 2010, July 05-08, 2010, Montpellier, France.*

5. **Molecular motor based on a Double Walled Carbon nanotube - A Molecular Dynamics Study.**,
   S. Negi, M. Warrier and S. Chaturvedi, *ICTP International Workshop on Nano-Opto-Electro-Mechanical Systems, September 06-10, 2010, ICTP, Trieste, Italy.*

National Conferences Proceedings:

1. "**Simulations of a Double Walled Carbon nanotube based motor.**",
   S. Negi, M. Warrier and S. Chaturvedi, *PSSI 2007, National Symposium on Plasma Science and Technology, Insitute for Plasma Research, Gandhinagar,*

Gujarat, India, December 06-10, 2007.

2. "**Simulations of a Double Walled Carbon nanotube based motor.**",
   S. Negi, M. Warrier and S. Chaturvedi, *52nd DAE Solid State Symposium, University of Mysore, Manasagangotri, Mysore, India, December 27-31, 2007.*

3. "**Locked states observed in the rotation of a Carbon Nanotube based motor.**",
   S. Negi, M. Warrier and S. Chaturvedi, *PSSI 2008, National Symposium on Plasma Science and Technology, Bhabha Atomic Research Center, Mumbai, India, December 10-13, 2008.*

SYNOPSIS

Carbon nanotubes have become very important in molecular research because of the potential applications of nanomachines in the field of computing, electronics, robotics and drug delivery. The high tensile strength and strong mechanical properties of these nanotubes make them a promising candidate for future nanomachinery. These nanometer devices, either alone or attached to a propeller, are a bright candidate for future machines which could be used for medical applications. Nanometer-sized devices, especially nanomotors, based on carbon nanotubes, are of interest for their novel applications in drug delivery techniques.

Earlier workers have reported the results of Molecular Dynamics (MD) simulations of electrically-driven nanomotors based on double-walled carbon nanotubes (DWNT). The inner and outer CNTs are called the "shaft" and "sleeve' respectively. Those studies broke new ground and yielded interesting insights into the atomistic level behavior of such nanomotors. However, those studies either did not consider certain aspects of nanomotor operation, or did not investigate them in sufficient detail. Some of those limitations have been addressed in the present thesis. In this thesis, we report on classical molecular dynamics simulations of a nanomotor based on a DWNT. Four major problems have been examined.

Firstly, during MD simulations of a DWNT-based motor with the sleeve held fixed, we found that distortion of the shaft at high electric fields leads to highly non-ideal behavior of the motor, such as 'locked states' in the rotation of the shaft inside the fixed sleeve. These results are in contrast to earlier MD results of other workers, which had indicated both motor-like and oscillatory motion of the nanomotor at the same electric field amplitudes. The frequency of shifts between the observed locked states correspond to the frequency of the applied electric field. An explanation has been given for these locked states in terms of the radial shape variations of the shaft and shifts in the centroid of the shaft inside the fixed sleeve. In the other set of simulations, where both the shaft and sleeve are free to move, the usual pendulum- and motor-like behavior is observed. A simple theoretical model is also given and we see that the motion of the shaft and the sleeve obtained from this model matches reasonably well with the MD results, although there are differences of detail.

Secondly, we have obtained, for the first time, the complete set of the characteristic modes of a single-walled carbon nanotube (SWNT) and a DWNT, using the novel technique of singular value decomposition (SVD) analysis on our molecular

dynamics data. Good agreement is observed between the calculated frequency of radial breathing modes (RBM) and published experimental measurements, as also the inverse scaling of this frequency with tube diameter. A few other important modes are obtained which are classified into two different classes, one having $m_z = 0$, i.e., axial uniformity, and the other class having $m_\theta = 0$, with $m_z = 1$ and 2, i.e., azimuthal uniformity. For the available cases, the frequencies of the above mentioned modes matches well with those in the literature. We also study, for the first time, the problem of resonant excitation of the SWNT. External excitation produced at one of the mode frequencies shows a significant and steady increase in the amplitude of centroid displacement. Excitation at the second harmonic frequency leads to an initial increase in displacement amplitude, but eventual saturation. These conclusions are important for the application of carbon nanotubes as nanomotors. Similar to the characteristic mode study of an SWNT, the characteristic modes of a DWNT are also studied. The RBM frequency is observed to be upshifted in the case of a DWNT. Also the frequencies of a few other modes are observed to be slightly different in this case. For some of the modes, multiple peaks are seen at more than one frequency point.

It can be shown by simple arguments that only certain combinations of the frequency and amplitude of the applied electric field should be able to produce pure motor-like motion in the nanomotor. Thirdly, therefore, we have determined the useful region in frequency-amplitude space for producing pure motor-like motion in the nanomotor. We have developed a theoretical model which yields the nominal operating point in amplitude-frequency space. We then study the full parameter space around this operating point using molecular dynamics simulations. For a given frequency, electric field amplitudes below a threshold are not able to overcome the potential energy barriers due to interaction of the rotating shaft with the frozen sleeve. This is then followed by a range of amplitudes where unidirectional motion is observed. At still higher amplitudes, distortion of the shaft increases the potential energy barriers to levels higher than those that can be overcome by the electric field. Hence we get three regions during the amplitude scan, only one of which is useful for a nanomotor. For a given amplitude, as the frequency is varied, more complex behavior is obtained, which can be broken up into four regions. At low frequencies (Region-1), large distortion of the shaft leads to an increase in potential energy barriers, hindering rotation. Over an intermediate range (Region-2), unidirectional

motion is observed, since shaft distortions are smaller than in Region-1. This is followed by an anomalous region (Region-3), where resonant excitation of a characteristic mode of the shaft leads to very large distortions, which greatly enhance the barrier. Finally, in Region-4, the distortion again starts falling off with rise in frequency. However, the frequency is now so high that the shaft cannot complete a full rotation before the field reverse sign. Hence unidirectional rotation is not obtained. A detailed physical explanation has been provided for the anomalous behavior in Region-3, in terms of resonant excitation of a characteristic mode.

Depending on the application, some part of the nanomotor must be attached to a surface, e.g. electrical contact for an electrically-driven motor. We must understand the behaviour of such "joints". Fourthly, therefore, we have made a start in this area by examining the interaction of an SWNT with a graphite surface. At a fixed temperature of 100 K, nanotubes of larger diameters are observed to acquire a large contact area on the top of the graphite surface. The tubes are seen to deform to have a larger contact area with the graphite surface and thus have larger binding energy with the surface. The variation of the binding energy per unit length along the axis of the CNT, obtained from our MD calculations, matches well with the Molecular Mechanics (MM) results of other workers. The contact area between the nanotube and the graphite surface is observed to become progressively smaller as the temperature is increased. This is because at higher temperatures, the atoms acquire higher kinetic energies, because of which they can overcome the interactions between the tube and the graphite. We also study the effect of the separation distance between neighboring nanotubes on the contact area between the tube and the graphite surface. All nanotubes having an intial separation greater than 6.9213 Å are observed to show qualitatively good flattening over the graphite surface.

Contents

List of Figures

List of Tables

Chapter 1

Introduction

There's Plenty of Room at the Bottom – Richard Feynman

Carbon nanotubes (CNT) first discovered by Iijima [1] have now become very important in molecular research because of their potential application for future electrical and mechanical devices [2]. A CNT is a tubular structure made up of carbon atoms. A CNT structure is described by a pair of integers (n,m). Depending on these integers (n,m), the tube is characterized as arm-chair, zig-zag or chiral. The symmetry and electronic properties of a Single-Walled carbon nanotube (SWNT) are completely described by these integers [3].

In the past few years the field of carbon nanotubes and nanomachines/nanodevices based on them have attracted many researchers because of the various potential applications of them in the field of computing, electronics, robotics, drug delivery etc. Some of the potential applications of carbon nanotubes are discussed below.

1.1 Applications of Carbon nanotubes

1.1.1 Electrochemical devices

Carbon nanotubes serve as a large number of electrochemical devices. Because of the high electrochemically accessible surface area of porous nanotube arrays, high electronic conductance and useful mechanical properties these tubes are attractive as electrodes for devices that can be used in electrochemical double layer charge

injection [4–6]. Examples include "super-capacitors" made up of carbon nanotubes. In contrast to the ordinary planar sheet capacitors these super-capacitors offer capacitance's typically between 15 and 200 F/g and result in large amount of charge injection when only a few volts is applied [4–7]. A large number of carbon nanotube based electrochemical bio-sensors are discussed in the review [8].

1.1.2 Hydrogen Storage

Carbon nanotubes are predicted as a good candidate for hydrogen storage. [9] reported on the hydrogen adsorption and storage inside single and multi-walled carbon nanotubes. They predicted that hydrogen exists as H_2 molecules inside CNTs and the storage capacity of hydrogen is limited by H_2 molecules inside the tube. Also the storage capacity increases linearly with the tube diameter in case of a single walled carbon nanotube. Whereas this capacity is independent of the tube diameter in a multi-walled nanotube. Yuchen Ma et.al [10] studied the hydrogen storage inside SWNT using Molecular Dynamics (MD) and ab-initio electronic calculations. They showed that hydrogen atoms with kinetic energy of 16-25 eV penetrate inside the CNT and form hydrogen molecules. Gradually these molecules condense to form liquid hydrogen inside the tube. The Molecular Mechanics (MM) results in [11] seem to indicate that high hydrogen content in the nanotubes can not be achieved through physisorption.

1.1.3 Nanometer-Sized Electronic Devices

Carbon nanotubes can be used as field emission electron source [12, 13] for flat panel displays [14], lamps [15], gas discharge tubes providing surge protection [16] and x-ray [17] and microwave generators [18]. A potential field applied between a carbon nanotube-coated surface and an anode produces high local fields as a result of the small radius of the nanofiber tip and the length of the nanofiber. Unlike for ordinary bulk metals, nanotube tip electron emission arises from discrete energy states rather than the continuous electronic bands [19]. With crossed SWNTs, three and four terminal electronic devices have been made [20] also a nonvolatile memory that functions like an electromechanical relay [21]. Integrated nanotube devices involving two nanotube transistors have also been reported [21, 22].

1.1.4 Electromechanical Devices

Tuzan et. al [23] simulated a nanomotor made up of two concentric carbon nanotubes one placed inside another stimulated by an external electric field. Motor like behavior is observed in combination to the usual pendulum like motion when this motor is stimulated by an external electric field.

Srivastava [24] simulated a carbon nanotube based gear as shown in Fig.1.1. A benzene molecule is attached to the gear and is powered by a laser. When the phases of the applied laser and of the nanotube are properly matched, unidirectional motion with accelerating and decelerating angular velocities is seen. The dynamics of

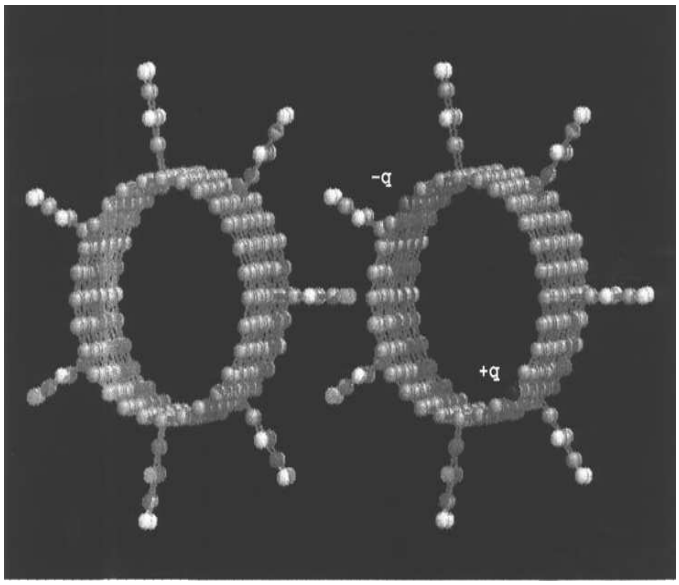

Figure 1.1: A Carbon nanotube based gear with positive and negative charges. The figure is adapted from [24].

an ion-driven nanomotor mimicking the F_0 part of the ATPs molecule in presence of and absence of an electric field is studied by [25]. They show that the motion of such a motor is controlled by the parameters such as positive ions placed inside the stator part of the motor, the density of the positive ions and the strength and the frequency of the applied field.

Servantie et. al [26] studied the drag force acting between two coaxial CNTs in such a system when they are set into relative angular motion. They studied the role of translational sliding motion and dynamic friction for axial rotation of the inner

nanotube in a Double-Walled carbon nanotube (DWNT) system using MD. They showed that the dynamic friction is linear in angular velocity for a wide domain of armchair-armchair, zigzag-armchair and zigzag-zigzag double walled CNT's. A gigahertz actuator based on multi-walled carbon nanotube encapsulating potassium ions was studied in [27].

Experimentally, a novel method of construction and successful operation of a fully synthetic nanoscale actuator incorporating a rotatable metal plate is reported in [28]. A multi-walled CNT serves as a key motion-enabling element in this nano-electromechanical system (NEMS). The device fully integrates electronic control and its mechanical response. A similar NEMS is reported in [29] where the rotating plate is attached to an inner multi-walled nanotube (MWNT) shell that turns inside outer shells fixed to two anchor pads. Huaming et. al [30] showed their interest for the application of such nanodevices for drug-delivery.

The present thesis focuses on the dynamics of a double-walled carbon nanotube based motor stimulated by an external electric field.

This chapter will give an introduction to the structure and some of the physical properties of the carbon nanotubes such as its vibrational properties. Many of the properties of a Single-Walled carbon nanotubes can be derived by zone-folding of the electronic and physical properties of the 2-D graphite [31]. Therefore we first give the notation used to describe graphite and the carbon nanotubes and then the respective unit cell and phonon dispersion relations are explained. In a later part of this chapter, we explain in detail the problem studied in this thesis.

1.2 Graphite

Graphite is a layered material. In each layer called a graphene, the carbon atoms are arranged in a hexagonal lattice with separation distance of 1.42 Å, and the distance between planes is 3.35 Å. So graphene is an one-atom-thick planar sheet of sp^2 bonded carbon atoms that are densely packed in a honeycomb crystal lattice. It can be visualized as an atomic-scale chicken wire made of carbon atoms and their bonds.

1.2.1 Unit Cell of graphene

The unit cell of a 2D graphene sheet consists of 2 carbon atoms as shown in Fig. 1.2(a). The Brillouin zone of the 2D graphene sheet is as shown in Fig. 1.2(b). The figure is adapted from [32].

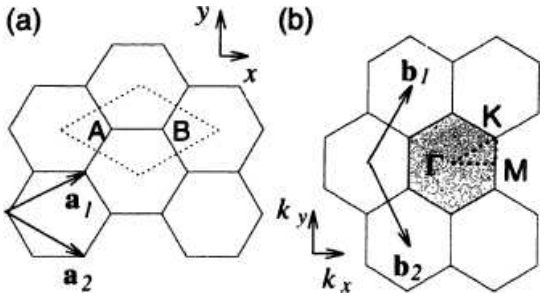

Figure 1.2: (a) The unit cell and (b) Brillouin zone of two dimensional graphite are shown as the dotted rhombus and the shaded hexagon, respectively. $\vec{a}_i$, and $\vec{b}_i$, (i = 1,2) are unit vectors and reciprocal lattice vectors, respectively. Here Γ, K and M are the high symmetry points in the reciprocal lattice.

1.2.2 Phonon Dispersion relation for 2D graphite sheet

The vibrational motion of a system of particles is often resolved in terms of its phonon modes. The phonon modes give the information about the lattice vibrations. These modes are often called as 'normal modes' of the system as they are the intrinsic modes of the system. These modes can give us information about various physical properties of the system for example its specific heat.

The phonon dispersion relation of a 2D graphite sheet is emperically obtained by fitting the force constant parameters [33] as explained in [31] to the neutron scattering data. The force constant parameters for a 2D graphene sheet are as given in Table 1.1 and the corresponding phonon dispersion curves plotted along the high symmetry point in Fig. 1.3 as adapted from [31].

1.3 Carbon Nanotubes

A Single-Walled carbon nanotube can be viewed as a single graphene sheet, one atom thick, rolled up into a seamless cylinder. Depending on the way the graphene

Radial	*Tangential*	
$\phi_r^1 = 36.50$	$\phi_{ti}^1 = 24.50$	$\phi_{to}^1 = 9.82$
$\phi_r^2 = 8.80$	$\phi_{ti}^2 = -3.23$	$\phi_{to}^2 = -0.40$
$\phi_r^3 = 3.00$	$\phi_{ti}^3 = -5.25$	$\phi_{to}^3 = 0.15$
$\phi_r^4 = -1.92$	$\phi_{ti}^4 = 2.29$	$\phi_{to}^4 = -0.58$

Table 1.1: Force constant parameters for 2D graphite in units of dyne/cm. Here the subscripts r, ti and to refer to radial, transverse in-plane and transverse out-of-plane respectively.

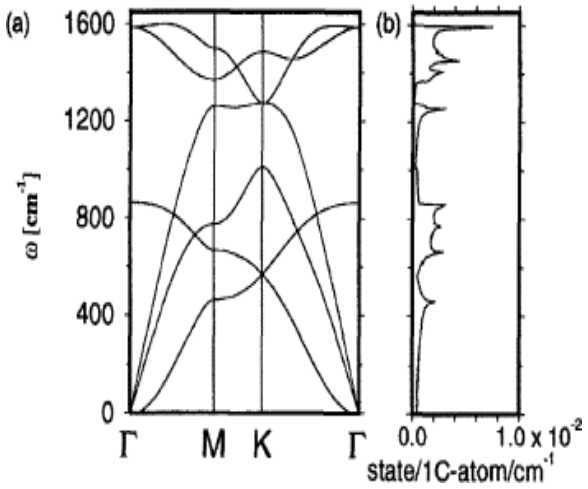

Figure 1.3: (a) The phonon dispersion curves, plotted along high symmetry directions, for a 2D graphene sheet, using the set of force constants in Table 1.1 (b) The corresponding density of states vs phonon energy for phonon modes in units of $states/1C-atom/cm^{-1} \times 10^{-2}$. The figure is adapted from [33]

sheet is rolled the SWNT is characterized as arm-chair, zig-zag or chiral tubes. The electrical and mechanical properties of these carbon nanotubes depend upon their type [31]. In the next few subsections we explain the basic notation used to describe the structure of a carbon nanotube as in [32].

1.3.1 Notation

Fig. 1.4, reproduced from [32], shows the rectangle of the graphene sheet which can be oriented to produce different types of nanotubes. The chiral vector $\mathbf{C_h}$ for the

nanotube is defined as:

$$\mathbf{C_h} = n\mathbf{a_1} + m\mathbf{a_2} \tag{1.1}$$

Where the vectors $\mathbf{a_1}$ and $\mathbf{a_2}$ are the lattice translation vectors of the graphite. Here n and m are two integers which describe the chiral vector $\mathbf{C_h}$. The chiral vector $\mathbf{C_h}$ connects two crystallographically equivalent sites O and A on the two dimensional graphene sheet where a carbon atom is located at the vertex of the honeycomb structure. The length of the translation vector T can be obtained by traveling a way from point O (at right angles to $\mathbf{C_h}$) until one reaches an equivalent site to O. A nanotube is a cylinder made by joining the line OB to the parallel line AB' in the Fig. 1.4. The unit cell shown in the Fig. 1.4 is for a (4,2) carbon nanotube.

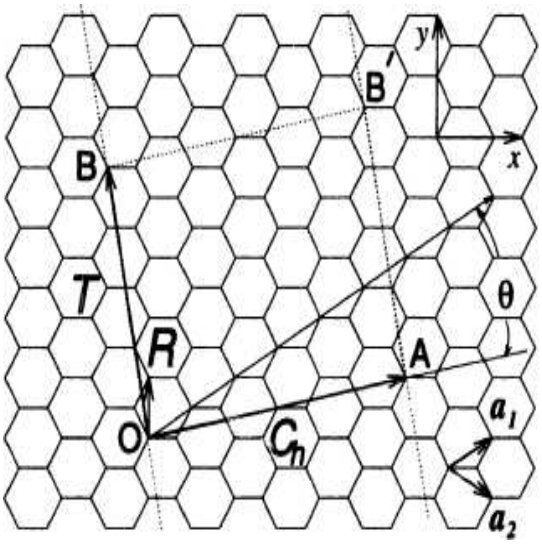

Figure 1.4: The unit cell of the carbon nanotube is the rectangle OAB'B here. When the point O is connected to point A, and B to B', a nanotube is constructed. In this rectangle $\vec{OA}$ and $\vec{OB}$ define the chiral vector $\mathbf{C_h}$ and the translation vector $\mathbf{T}$ of the nanotube respectively. This figure is adapted from [31]

Depending on the way of folding and the integers (n,m) the type of the nanotube will be different. In our simulations, we have used mainly arm-chair and zig-zag type of nanotubes. Fig. 1.5 shows a (5,0) SWNT and a (5,0)@(15,0) DWNT used in our simulations.

The diameter of the nanotube d_t is given as

$$d_t = |\mathbf{C_h}|/\pi = \sqrt{3}a_{c-c}\frac{\sqrt{(m^2 + mn + n^2)}}{\pi} \tag{1.2}$$

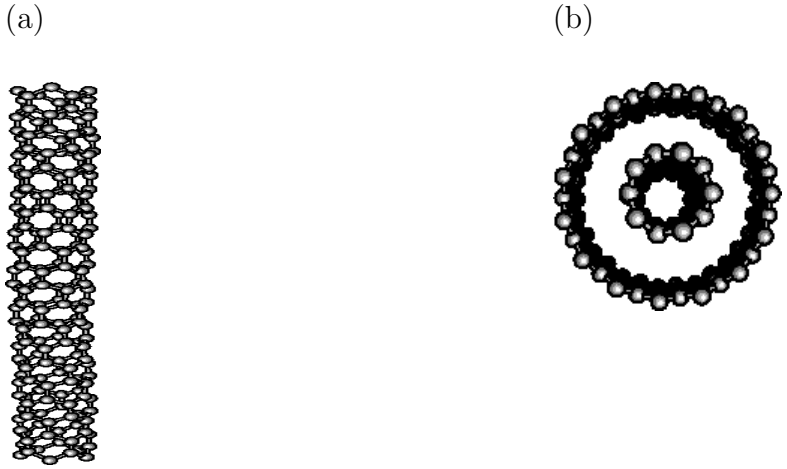

Figure 1.5: (a) A (5,0) Single-Walled carbon nanotube (SWNT) (b) A (5,0)@(15,0) Double-Walled carbon nanotube (DWNT)

Where C_h is the length of the chiral vector $\mathbf{C_h}$ and a_{c-c} defines the length of the carbon-carbon bond length. The chiral angle θ is given as:

$$\theta = tan^{-1}\left[\frac{\sqrt{3}m}{(m+2n)}\right] \tag{1.3}$$

When the angle θ is zero in the Fig. 1.4, it results in a zigzag nanotube and when θ is 30 deg, then it results in an armchair nanotube. Any angle of θ between 0 and 30 deg gives rise to chiral nanotubes.

1.3.2 Unit cell of a Carbon nanotube

The unit cell of a carbon nanotube is defined as the rectangle OBB'A. It can also be defined in terms of its basis vectors $\mathbf{a_1}$ and $\mathbf{a_2}$. As shown in Fig. 1.4, a_1 and a_2 are the two basis vector of the carbon nanotube unit cell in the real space. b_1 and b_2 are the reciprocal lattice vectors. The real space basis vector are given as:

$$a_1 = \left(\frac{\sqrt{3}a}{2}, \frac{a}{2}\right), \qquad a_2 = \left(\frac{\sqrt{3}a}{2}, \frac{-a}{2}\right) \tag{1.4}$$

where a = -a_1 = -a_2 = $1.42 \times \sqrt{3} = 2.46$ Å is the lattice constant of the 2D graphite. The basis vector b_1 and b_2 of the reciprocal lattice are given by:

$$b_1 = \left(\frac{2\pi}{\sqrt{3}a}, \frac{2\pi}{a}\right), \qquad b_2 = \left(\frac{2\pi}{\sqrt{3}a}, \frac{-2\pi}{a}\right) \tag{1.5}$$

corresponding to a lattice constant of $4\pi/\sqrt{3}a$ in reciprocal space. As shown in Fig.1.2 the high symmetry points Γ, K and M are the center, the corner and the center of the edge respectively.

The translation vector of the nanotube is given as the vector $\vec{OB}$ in Fig. 1.4 and is given as:

$$\mathbf{T} = t_1 a_1 + t_2 a_2 \ = (t_1, t_2) \tag{1.6}$$

where t_1 and t_2 are defined as:

$$t_1 = \frac{(2m+n)}{d_R}, \qquad t_2 \ = \ \frac{-(2m+n)}{d_R} \tag{1.7}$$

Where d_R is the greatest common divisor of $(2n+m, 2m+n)$ and is given as:

$$d_R \ = \ d, \ if \ n-m \ is \ not \ a \ multiple \ of \ 3d, else \tag{1.8}$$

$$d_R \ = \ 3d, \ if \ n-m \ is \ a \ multiple \ of \ 3d \tag{1.9}$$

where d is the greatest common divisor of (n,m). The magnitude of the translation vector is given as:

$$|T| = \sqrt{3}L/d_R \tag{1.10}$$

where L is the length of the chiral vector $C_h = \pi \ d_t$ and d_t is the nanotube diameter.

The unit cell of the nanotube is defined as the area under the rectangle defined by vectors T and C_h. The number of hexagons, N in one unit cell of the nanotube is defined as:

$$N = \frac{2(m^2+n^2+nm)}{d_R} \tag{1.11}$$

In the unit cell addition of a single hexagon to the honeycomb structure leads to addition of two carbon atoms. Thus the unit cell of a carbon nanotube is defined by the vector $\mathbf{C_h}$ and $\mathbf{T}$. Similarly the reciprocal space is defined by the vectors K_1 and K_2 defined as:

$$K_1 = \frac{1}{N}(-t_2 b_1 + t_1 b_2) \tag{1.12}$$

$$K_2 = \frac{1}{N}(m b_1 - n b_2) \tag{1.13}$$

Where b_1 and b_2 are the reciprocal lattice vectors of a two dimensional graphene sheet.

In the next section we explain the phonon dispersion relation of a carbon nanotube. Because of the similarity in the local structure of the carbon nanotube and the graphene sheet, the electron and the phonon relation of a CNT can be obtained from that of a graphene sheet by using zone-folding techniques [31].

1.3.3 Phonon dispersion relation of a Carbon nanotube

As explained in subsection 1.2.2 the phonon modes give the information about the lattice vibration of the system. As the main aim of this thesis is to study the atomistic behavior of the carbon nanotube based devices, the phonon modes would be helpful to study this behavior in terms of various modes and their frequencies. The phonon branches of a CNT would give the information about the propagation of waves in the system.

In the following subsection we explain the phonon dispersion relations of a carbon nanotube as given in [31]. Because of the symmetry in the structure the phonon dispersion relation of an SWNT is obtained by folding the phonon dispersion curves of a 2D graphene layer as discussed in subsection 1.2.2. Since there are 2N carbon atoms in the unit cell of a carbon nanotube, there will be a total of 6N phonon dispersion relations. These phonon relations are for the x, y and z vibrations for each atom and are folded into the one-dimensional Brillouin zone of a carbon nanotube along the vector K_2. The phonon dispersion relations of a carbon nanotube also depend on (n,m) and the diameter of the the tube, d_t, since the phonon wave vector in the circumferential direction becomes discrete for vector K_1.

The one-dimensional phonon energy dispersion relation $\omega_{1D}^{m\mu}(k)$ for the nanotubes as in [31] is given by,

$$\omega_{1D}^{m\mu}(k) = \omega_{2D}^{m}\left(\frac{kK_2}{|(K_2|) + \mu K_1}\right) \tag{1.14}$$

where m = 1,...6, μ = 0,...,N-1 and $-\pi/T <$ k $< \pi/T$. The phonon dispersion branches calculated for a (10,10) nanotube by [31] is shown in Fig. 1.6. Here T denotes the magnitude of the unit vector along the length of the nanotube. For the 2N = 40 carbon atoms per circumferential strip for the (10,10) nanotube, they have 120 vibrational degrees of freedom, but because of mode degeneracies there are only 66 distinct phonon branches, of which 12 modes are non-degenerate and 54 are doubly degenerate. The distinct phonon branches can also be obtained by point group theory for atoms in the unit cell [31].

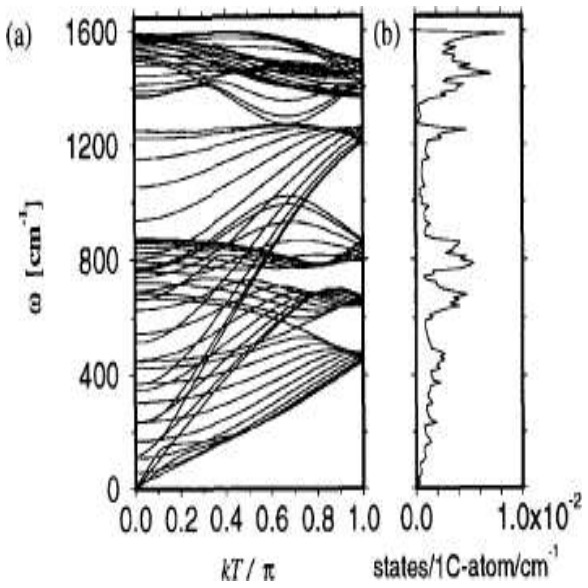

Figure 1.6: (a) The calculated phonon dispersion relations of an armchair carbon nanotube with c_h = (10,10). The number of degrees of freedom is 120 and the number of distinct phonon branches is 66. (b) Phonon density of states of (10,10) nanotubes. The figure is adapted from [33].

1.4 Major issues with CNT-based nanomotors

As discussed in subsection 1.1.4, one of the potential applications of a carbon nanotube is its use as an electromechanical device or a motor. But there are several major issues related to the nanomotors examined by Tuzan, Servantie etc. Some of these issues are listed below:

1. Non-ideal behavior of the inner CNT (shaft) when it rotates inside a static outer CNT (Sleeve). For example, the DWNT configurations is likely to undergo large distortions due to the application of a large electric field. How do these distortions affect the performance of the motor?

2. When a nanomotor shaft is attached to a device like a rotating blade (e.g. in a propeller), the non-ideal motion of the shaft is likely to produce non-ideal motion of the propeller. This motion is likely to be related to the intrinsic (characteristic) modes of the system. These modes must be determined.

3. For a given nanomotor configuration, are there any limits to its operation in terms of the applied electric field and its frequency?

4. For practical applications, such a nanomotor would have joints when attached to a propeller. How would these joints behave at different temperatures?

5. Charges could be placed on certain atoms of the nanomotor by attaching groups with different electronegativities. What kind of charge distribution would be produced by attachment of specific groups, and how would this charge distribution change as a function of time in a functioning nanomotor?

6. A nanomotor is likely to be immersed in a fluid. How would the presence of the fluid affect the behavior of the nanomotor, especially if the fluid enters the inter-CNT gap?

7. In the case of an electrically-driven nanomotors, a strong electric field may be required to produce differential rotation of the two CNTs. Getting such a high amplitude electric field of terahertz frequency is an open issue.

8. Would the high amplitude electric field affect the inter-particle interactions?

9. In case of a nanomotor attached to a propeller, the distortions produced in the shaft would also produce distortions of various kinds in the propeller. These distortions must be studied.

In the present thesis, we focus on items 1-4 above.

1.5 Overview of the problem

In the present work, we computationally study the behavior of a double-walled carbon nanotube based motor in the presence of an external electric field. Tuzan [23] performed simulations of such a motor using MD with an empirical Lennard-Jones 6-12 potential for the intertube interaction (i.e for interaction between the two nanotubes) and a three body interaction term for the intratube interaction (interactions within the carbon nanotube). However we use the Brenner potential [34] for intratube interactions which is an empirical many body potential that can simulate hydrocarbons very well. For the intertube interactions we use Nordlund's long range interaction potential [35]. Unit positive and negative charges are assumed on atom number 1 and 6 of the shaft and an external electric field of the form $qE_a cos(\omega_E t)$ is applied on the shaft (inner CNT) as seen in Fig.1.7. In the presence

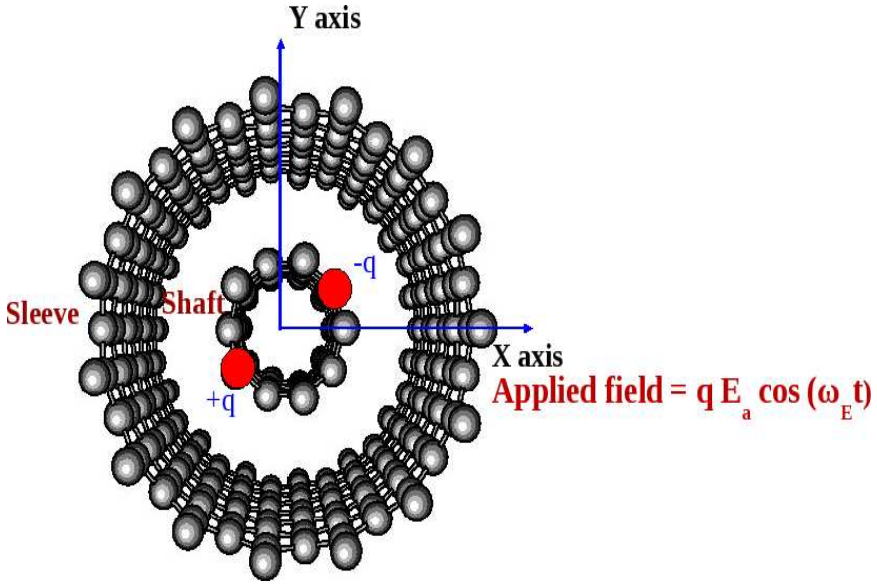

Figure 1.7: End-on view of the DWNT configuration. A sinusoidally varying electric field is applied to atom no. 1 and 6 in the x direction at time t = 0 sec. The line joining the two diametrically opposite atoms no. 1 and 6 makes an angle of 20 deg with the direction of applied electric field (X axis).

of an external electric field, the two charged atoms experience equal and opposite forces, which make the shaft to rotate inside the sleeve (outer CNT). Tuzan had studied the case of both the shaft and the sleeve moving. The case of a static sleeve was not studied. Also, the intertube separation used by Tuzan was more than the actual separation distance found in case of a DWNT [36, 37]. For a nanometer-sized motor made up of carbon nanotubes, where a propeller can be attached to it, we expect the shaft to exhibit unidirectional motor-like motion inside a static sleeve like an ideal motor. Therefore, we also perform the simulations where the sleeve is held fixed and the shaft is made to rotate inside this static sleeve.

Below we give the typical physical parameters of the nanomotor studied in this thesis:

- Diameter - The typical diameter of the carbon nanotubes used in our simulations ∼4-10 Å.
- Forces - In such nano-systems made up of carbon nanotubes the forces are of the order of pico-newtons.
- Time-scales - The typical time scales of interest are few pico-seconds since we

have to cover atleast few cycles of the applied electric field period.

- Electric field - Electric fields with amplitude $\sim(10^9 - -10^{10})$ V/m and frequency $\sim(10^{10}$–$10^{12})$ rad/sec are studied.

- Magnetic field - The typical atomic velocities in these systems are observed to be $\sim$100 m/sec. A simple calculation shows that the magnetic fields produced by the charge movement will thus be negligible.

1.6 Method of simulation

The main aim of this thesis is the study of a nanomotor based on a double-walled carbon nanotube, driven by an externally-applied time-harmonic electric field. The behavior of such a device depends sensitively upon inter-atomic interactions. Such interactions, acting on picosecond time-scales, lead to non-rigid behavior of both the inner and outer CNTs. This means that the components of this motor cannot be modelled as rigid elements, and the behavior of individual atoms must be taken into account. Hence it is necessary to perform atomistic simulations of such a system, i.e., molecular dynamics (MD).

Starting from a state of rest, we expect the nanomotor to exhibit some transients and then settle down to motor-like motion. These transients are likely to die out over a period that is related to the period of the applied field, as well as the time periods of the characteristic modes of the motor. Hence we expect that the simulation should be run for a few nanoseconds. Furthermore, in order to get the ensemble average of a physical quantity, we would need a significant number of atoms to be simulated. Within molecular dynamics, there is a choice of two methods:

- Classical Molecular Dynamics : The aim of classical molecular dynamics is to model the detailed microscopic dynamical behavior of many different types of systems. It computes the time evolution of a system solving Newton's force equations, given the interaction between the species. The details of this technique will be discussed in the next chapter.

- Ab-initio Molecular Dynamics (DFT) : This is the most popular extension of classical molecular dynamics which includes first-principle derived potential functions. This is assumed to be the most accurate way of doing molecular

dynamics simulations but has a major drawback i.e, its computational cost. The details of Ab-initio MD are discussed in [38].

Ab-initio MD would be the most accurate way of simulating such systems. However, the heavy computational load associated with ab-initio simulations makes nanosecond simulations impractical with our resources. Hence we have made use of classical MD simulations.

We use the HCParCas code using the Brenner potential [34] to account for the intratube interactions (interactions within a nanotube) with Nordlund's long range interaction term [35] to account for the intertube interactions (interactions between two nanotubes).

1.7 Outline of the thesis

The outline of the thesis is as follows. In the next chapter we discuss the computational technique in detail, covering MD as well as the application of Singular Value Decomposition (SVD) to the analysis of MD results. The MD simulations of a double-walled carbon nanotube based motor are discussed in Chapter 3. We are interested in understanding the behavior of nano devices in the presence of an external electric field. Therefore, it is important to understand the inherent motion of such systems. This inherent motion of the system can be resolved in terms of the characteristic modes of the system. Chapter 4 examines the characteristic modes of single and double walled carbon nanotubes. In Chapter 5 we determine the useful operating parameter space for a DWNT based motor. The interactions of carbon nanotubes with a graphite surface are discussed in Chapter 6. Finally we summarize the results of the thesis and discuss the future scope in Chapter 7.

Chapter 2

Simulation Technique

If we were to name the most powerful assumption of all, which leads one on and on in an attempt to understand life, it is that all things are made of atoms, and that everything that living things do can be understood in terms of the jigglings and wigglings of atoms – Richard Feynman

In this chapter we give an overview of the computational techniques, viz., Molecular Dynamics (MD) and the Singular Value Decomposition (SVD) analysis of MD results.

2.1 Molecular Dynamics

Molecular Dynamics is a numerical way of solving the the N body problem. The basic idea is to calculate how a system of particles evolves in time. The method was first used with a realistic potential by Alder and Wainwright in 1959 to calculate the vibrations of atoms in molecules.
Consider a set of atoms at positions r_i and some interaction model which gives us the potential energy of the system ϕ_{ij}. The most intuitive method to study microscopically the motion of such a collection of atoms and their interactions amongst themselves is to solve the N-body force equation:

$$m_i \ddot{\vec{r_i}} = \sum_{j=1}^{N} (-\nabla \phi_{ij}) \tag{2.1}$$

where $\vec{r_i}$ is the position vector of a particle denoted by i, m_i is the mass of the i^{th} particle and ϕ_{ij} is the inter-atomic potential between the i_{th} and the j_{th} particle. MD

solves the above equations numerically, since even for a small N, or for a complicated ϕ_{ij}, the above equation is not analytically solvable. MD algorithm is as follows:

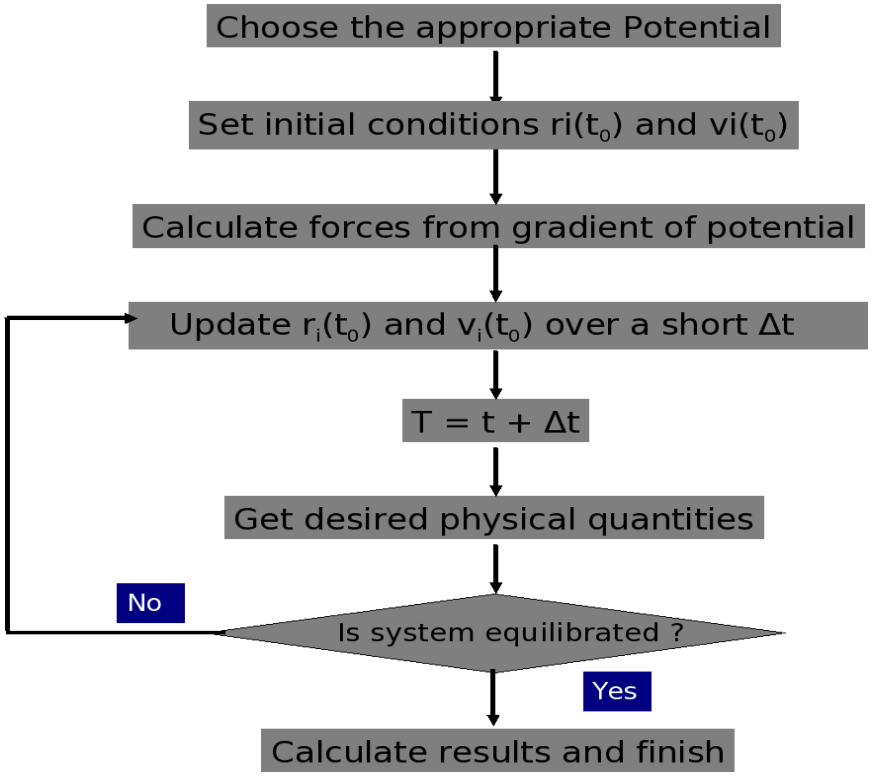

Figure 2.1: Algorithm of the Molecular Dynamics (MD) scheme.

2.1.1 Choice of MD Time step

The most commonly used time steps in the MD simulations is assumed to be on the order of femtoseconds. MD uses a Taylor's expansion as follows to solve the Eqn.2.1:

$$r(t+\delta t) = r(t) + v(t)\delta t + \frac{1}{2}a(t)(\delta t)^2 + .. \tag{2.2}$$

$$v(t+\delta t) = v(t) + a(t)\delta t + \frac{1}{2}b(t)(\delta t)^2 + .. \tag{2.3}$$

$$a(t+\delta t) = a(t) + b(t)\delta t \tag{2.4}$$

where r is the position, v is the velocity and a is the acceleration of the particle. The neglect of higher order terms is justified if the acceleration of the particle does not change significantly during a timestep. Now, the acceleration depends upon the gradients of the potential energy of the system with respect to individual atom

coordinates. The timestep must, therefore, be small enough so that these gradients do not change significantly during a single timestep δt.

According to a simple thumb rule, as discussed in [39], it is assumed that a particle can move at most $(1/20)^{th}$ of the distance between two neighboring atoms in a time step of δt. As an example from [39] the inter-atomic distance in a graphene plane is 1.4 Å and the typical velocity of an interstitial hydrogen atom which is equilibrated with a graphene plane at 900 K is 0.047 Å / femtosecond. Therefore the time step in this case becomes 1.5 femtosecond.

Another way to cross-check the suitability of the timestep is to check for energy conservation in a simulation where there is no energy exchange with the surroundings, i.e., in an isolated system. Also, the overall simulation results should not change significantly due to changes in the timestep.

Keeping in mind the above criteria, we choose a time step of 0.1 femtosecond in most of our simulations. In some cases, where bigger timesteps were used, a detailed explanation has been provided.

2.1.2 Ensembles used

An ensemble is a collection of all possible systems which have different microscopic states but have an identical macroscopic or thermodynamic state. There exist different ensembles with different characteristics [40]:

- Microcanonical ensemble (NVE) : The thermodynamic state characterized by a fixed number of atoms (N), a fixed volume (V) and a fixed energy (E). This corresponds to an isolated system like an isolated CNT, for example, which is neither going to gain nor loss energy or particles with the surrounding.

- Canonical Ensemble (NVT): This is a collection of all systems whose thermodynamic state is characterized by a fixed number of atoms (N), a fixed volume (V) and a fixed temperature (T). An example is a system at room temperature, 300 K, which can exchange energy with a thermostat to maintain the temperature. However no exchange of particles occur.

- Isobaric-Isothermal Ensemble (NPT): This ensemble is characterized by a fixed number of atoms (N), a fixed pressure (P) and a fixed temperature (T) which means that the volume of the system changes to maintain the pressure. Also the thermostat maintains the temperature.

- Grand canonical Ensemble (mVT): The thermodynamic state for this ensemble is characterized by a fixed chemical potential (m), a fixed volume (V) and a fixed temperature T which means that both particles and energy can be exchanged. An example of this is an impurity atom in a semiconductor which can exchange electron from the conduction band.

2.1.3 Potential used

The potential function in MD is a set of parameters e.g bond angles, bond lengths etc, which defines the interactions between a set of atoms. These interaction parameters can be obtained theoretically or from experiments, or a combination of both. The Brenner potential [34] is used in this work for the intratube interactions (interactions within a nanotube), along with Nordlund's long range interaction term to account for the inter-tube interactions (interactions between nanotubes) [35]. The Brenner potential is a reactive empirical many body bond-order potential energy expression. Bond order potential means that the chemical bond depends on the local bonding environment, including the number of bonds and possibly also angles and bond lengths. It takes into account the number of neighbors an atom has in its surroundings within a cutoff distance. Examples include the Tersoff potential [41], the Brenner potential [34] and the second-moment tight-binding potentials [42].

These potentials have the advantage over conventional molecular mechanics force fields in that they can, with the same parameters, describe several different bonding states of an atom, and thus to some extent may be able to describe chemical reactions correctly. The potentials were developed partly independently of each other, but share the common idea that the strength of a chemical bond depends on the bonding environment, including the number of bonds and possibly also angles and bond length. More details about this potential can be found in [34]. In the past few years, this potential has been used extensively for the study of carbon-nanotube based systems.

Nodlund's potential [35] is a radial potential which is used to define the interaction between two carbon nanotubes or between one carbon nanotube and a graphite surface. The typical cut off distance used in this potential is 4.2 Å.

2.1.4 Boundary conditions

In most of the MD simulations, the atoms are arranged in a simulation 'box' which has a size $L_x L_y L_z$, the three parameters representing the dimensions in the x, y and z directions. There are different ways of handling atoms crossing the boundary, appropriate to the problem. In some cases, atoms on the box/cell boundary are kept free (free boundaries). This would work if one wants to do an MD simulations of an isolated system like an isolated molecule or a system in vacuum. For a system which is essentially infinitely long in a given dimension, periodic boundary conditions (PBC) can be used. PBC are implemented using the minimum image convention method which is explained later.

The PBC boundary condition is implemented following the algorithm as in [39]:

- During the simulation, when an atom which crosses over a cell boundary it is assumed to come back from the other side using the PBC as shown in the figure below:

  This can be implemented using a simple algorithm as given in [39] which

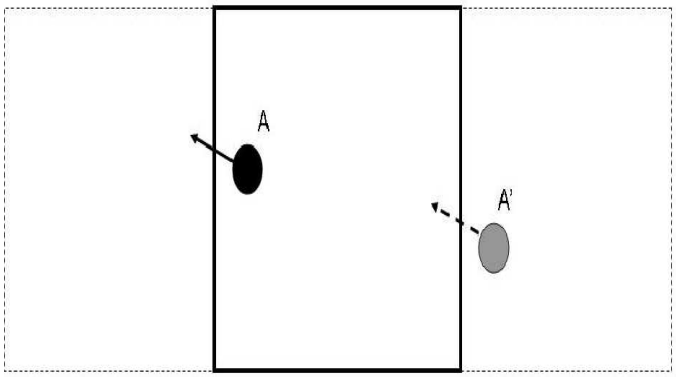

Figure 2.2: Implementation of periodic boundary conditions in MD algorithm.

calculates the present coordinate 'x' of the atom and compares it with the size of the simulation box 'xsize' as follows:
if (periodicx) then
if (x < -L_x/2.0) x = x + L_x
if (x > L_x/2.0) x = x - L_x
end if
and same for y and z coordinates. Note that, here the simulation box size varies from -L_x/2 to L_x/2.

- Also when the distance between any two atoms is calculated, the periodic boundaries have to be taken into account: The box shown with the solid line

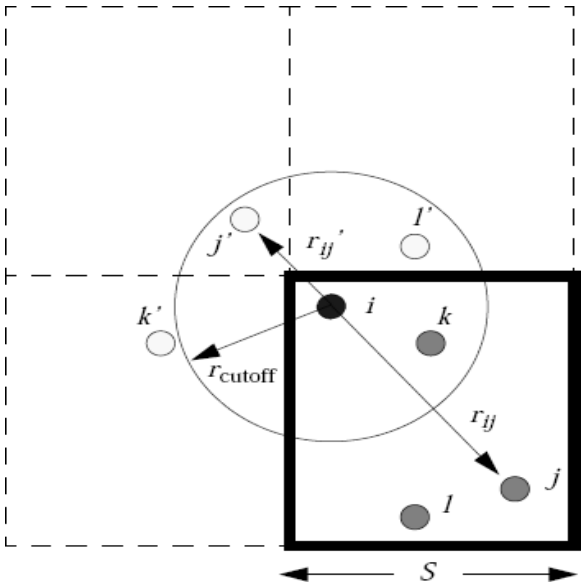

Figure 2.3: Implementation of periodic boundary conditions in MD algorithm using minimum image convention. This figure is adapted from [40]

is the simulation cell, with atoms i, j, k and l. This figure is adapted from [39] which explains the method of minimum image convention. Minimum image convention means that the periodic boundary conditions are used in such a way, which calculates forces on each atom over and above periodic handling of any atomic border crossings. Because of the PBC considered here, all the atoms in the simulation will have image atoms in the neighboring cells like j', k' and l'. Suppose we want to calculate the distance between the atoms i and j then we would choose $r_{ij'}$ instead of r_{ij} because $r_{ij'} < r_{ij}$ and similarly for y and z coordinate. The algorithm is adapted from [39]: if (periodicx) then
dx = x(j) - x(i)
if (dx < L_x/2.0) dx = dx - L_x
if (dx > - L_x/2.0) dx = dx + L_x
endif
and similarly for y and z coordinates. This way we get a simulation cell with infinite number of image cells in the directions of periodicity X and Y in this case.

2.1.5 Integration Schemes

Various integration schemes are used in an MD simulation to integrate the equation of motion of the atoms. The most commonly used are Leap-frog, Verlet, Velocity Verlet and Predictor corrector method. All integration schemes assume that the atom positions, velocities and accelerations can be approximated by a Taylor series expansion as in [40]:

$$r(t+\delta t) = r(t) + v(t)\delta t + \frac{1}{2}a(t)(\delta t)^2 + .. \tag{2.5}$$

$$v(t+\delta t) = v(t) + a(t)\delta t + \frac{1}{2}b(t)(\delta t)^2 + .. \tag{2.6}$$

$$a(t+\delta t) = a(t) + b(t)\delta t \tag{2.7}$$

where r is the position, v is the velocity and a is the acceleration of the particle.

Verlet algorithm

To derive the Verlet algorithm one can write [40]:

$$r(t+\delta t) = r(t) + v(t)\delta t + \frac{1}{2}a(t)(\delta t)^2 \tag{2.8}$$

$$r(t-\delta t) = r(t) - v(t)\delta t + \frac{1}{2}a(t)(\delta t)^2 \tag{2.9}$$

summing these two equations, one gets

$$r(t+\delta t) = 2r(t) - r(t-\delta t) + a(t)(\delta t)^2 \tag{2.10}$$

The Verlet algorithm uses positions and accelerations at time t and the positions from time $t-\delta t$ to calculate new positions at time $t+\delta t$. The Verlet algorithm uses no explicit velocities. The advantages of the Verlet algorithm are, i) it is straightforward, and ii) the storage requirements are modest . The disadvantage is that the algorithm is of moderate precision.

Velocity Verlet algorithm

This algorithm yields positions, velocities and accelerations at time t. There is no compromise on precision. The equations are as follows [40]:

$$r(t+\delta t) = r(t) + v(t)\delta t + \frac{1}{2}a(t)(\delta t)^2 + ... \tag{2.11}$$

$$v(t+\delta t) = v(t) + \frac{1}{2}[a(t) + a(t+\delta t)\delta t \tag{2.12}$$

Thus the velocities are used explicitly in the velocity-verlet algorithm.

Leap-frog algorithm

The leap-frog algorithm uses the equations [40]:

$$r(t+\delta t) = r(t) + v(t+\frac{1}{2}\delta t)\delta t \tag{2.13}$$

$$v(t+\frac{1}{2}\delta t) = v(t-\frac{1}{2}\delta t) + a(t)\delta t \tag{2.14}$$

In this algorithm, the velocities are first calculated at time $t + 1/2\delta t$; these are then used to calculate the positions, r, at time $t + \delta t$. In this way, the velocities leap over the positions, then the positions leap over the velocities. The advantage of this algorithm is that the velocities are explicitly calculated, however, the disadvantage is that they are not calculated at the same time as the positions. The velocities at time t can be approximated by the relationship:

$$v(t) = \frac{1}{2}[v(t-\frac{1}{2}\delta t) + v(t+\frac{1}{2}\delta t)] \tag{2.15}$$

Predictor-Corrector algorithm

The HcParCas code uses the Predictor-Corrector (PC) integration scheme. This scheme proceeds in two steps, firstly the predictor step predicts the approximate values of certain quantities like position and velocities then the corrector step corrects these predicted values. In short the steps of a PC scheme can be described as follows [43]:

- In the Predictor step from the positions and their time derivatives, known at time t, one can predicts the same quantities at time $t+\delta t$ by means of a Taylor expansion.
- Secondly the force is computed taking the gradient of the potential at the predicted positions. The quantities computed in such will be different than the predicted values.
- In the Corrector step the difference of these quantities calculated above is used to correct the positions and velocities of the atoms.

2.1.6 Thermostat

The initial velocities in an MD simulation are set by assuming a Maxwell-Boltzmann distribution which will be explained in the next section. This is done by choosing a

Gaussian distributed random number which is then multiplied by the mean square velocity in each direction. Since we are considering a driven system, we expect it to gain energy from the applied field and hence it can acquire a high temperature. Therefore it becomes very crucial to maintain the temperature of the system throughout the simulation. This high temperature can be obtained from the velocities of the particles.

We also want to make sure that the total momentum of the system remains equal to zero which means that the center of mass of the system should not move throughout the simulation. Thus by choosing the initial velocities for all the atoms we have fixed the temperature of our system and also the total energy of the system. But this process of fixing the temperature cannot be used at each step since it will fix the temperature rigidly. Also in this method of fixing the temperature, the normal fluctuations of the system will also be suppressed. That is why different temperature control schemes are used to maintain the temperature of the system more accurately equal to the desired temperature. The various schemes are:

- Berendsen's thermostat
- Noose Hover thermostat
- Langevin thermostat

Berendsen's thermostat [44] is used in the HcParCas code, used in this work. In this scheme the system is coupled to a heat bath at some temperature. All the velocities are scaled at each time step by a factor λ given as in [39]:

$$\lambda = \sqrt{1 + \frac{\delta t}{\tau_T}(\frac{T_0}{T} - 1)} \tag{2.16}$$

Where δt is the time step, $\tau(T)$ is the time constant for temperature control and has to be greater than $100\delta t$. T_0 is the desired temperature and T is the current temperature. Thus Berendsen's thermostat is maintained by scaling the velocities for a specified number of MD steps. The details of the Nose-Hover and Langevin thermostats can be found in [45].

2.1.7 Barostat

Similar to Berendsen's thermostat, Berendsen's pressure control is also implemented. Here the atomic positions are changed, and the system size is scaled at each time

step by a factor μ given by [39]:

$$\mu = [1 - \beta\frac{\delta t}{\tau_P}(P_0 - P)]^{1/3} \tag{2.17}$$

where τ_P is the time constant for pressure control which should be greater than $100\delta t$. P_0 is the desired pressure and P is the current pressure. β is the isothermal compressibility.

2.1.8 Initializing atom velocities

The initial atom velocities of the atoms are generated according to the Eqn.2.18 which match a Maxwell-Boltzmann distribution. This Maxwell-Boltzmann distribution correspond to a desired temperature. The distribution is given as:

$$P(v_{i\alpha}) = \sqrt{\frac{m_i}{2\pi K_B T}} exp\left[\frac{-1}{2m_i(v_{i\alpha})^2 K_B T}\right] \tag{2.18}$$

where α = x, y, z. As explained in the subsection 2.1.6 certain parameters are to be chosen to scale the positions and velocities of the atoms. We choose the parameters suitably so that the velocity distribution is close to a Maxwellian distribution. In order to check this, the velocity distribution obtained during the NPT relaxation of the entire DWNT assembly is monitored throughout the simulation. Fig. 2.4 (i) shows the cumulative velocity distribution plotted as a function of E/kT, at intervals of 20 ps. Here, kT is the temperature and E is the kinetic energy. The theoretical expression for maxwellian velocity distribution is also shown on the same figure. A fair match can be seen. Defining the temperature as two-thirds of the average kinetic energy per particle, we can study its temporal evolution through the NPT relaxation. This is shown in Fig. 2.4 (ii). The temperature settles down to the desired temperature of 0.025 eV (300 K) at ∼5000 fs.

One more point which should be kept in mind before starting an MD simulation is that the the total momentum of the cell should be zero to prevent the entire cell from moving i.e

$$P = \sum(m_i v_i) = 0 \tag{2.19}$$

2.2 Singular Value Decomposition (SVD)

Another computational technique which is used in this work is Singular Value Decomposition (SVD). We use SVD on our MD data to extract the characteristic

(i) (ii)

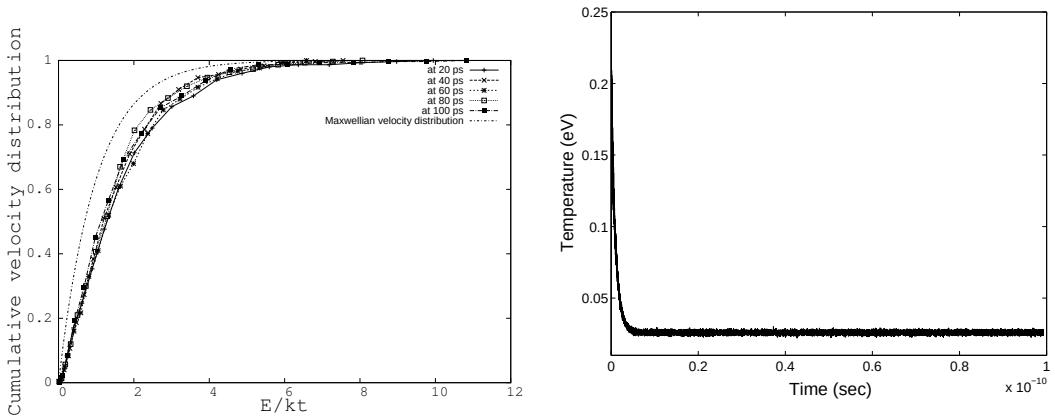

Figure 2.4: (i) Cumulative velocity distribution. (ii) Temperature (eV) during the NPT relaxation (Note here that the temperature stabilizes to the desired temperature of 300 K (0.025 eV) at 5000 fs.

modes of a Single-Walled carbon nanotube and a Double-Walled carbon nanotube. SVD help us to extract all of the characteristic modes of the system in the order of their hierarchy. The details of the SVD technique are discussed below.

SVD is a powerful technique for solving sets of equations involving matrices that are either singular or numerically close to singular, where methods such as Gaussian-elimination or lower-upper (LU) decomposition fail to give satisfactory results. This method can readily be applied to problems where the number of equations is either more or less than the number of unknowns. It is also the method of choice for solving linear least-squares problems [46]. Details of the SVD method are available in [46]. Its application to the determination of mode structures in fusion plasma devices, including important features and limitations, is described in [47]. In the following subsection, we give a brief description of the method and its application to the modal analysis of MD simulation results.

2.2.1 SVD method

Let us consider a physical quantity 'x' simultaneously measured at 'm' different positions (coordinates), and sampled at 'n' different times with a sampling interval t_s. The matrix representation of the above observation can be generally expressed

by a rectangular array, $x_{ij} = x_j[(i-1)t_s]$, where the row index 'i' refers to time and the column index 'j' to the coordinate. The SVD of the matrix x_{ij} is expressed as

$$X = USV^T \tag{2.20}$$

where superscript 'T' refers to the transpose of a vector. Here, **U** is a n×m matrix and **V** is a m×m square matrix, both of which have orthogonal columns so that $UU^T = VV^T = I$ (identity matrix). **S** is a diagonal matrix i.e. $S_{ij} = \delta_{ij}s_i$, the quantities $s_{ii} \geq 0$ being called 'singular values'. The SVD is an analogue of the similarity transformation which diagonalizes a square matrix. The products SU are analogues of eigenvalues, while the V columns $v^j = V_{ij}$ are the analogues of the eigenvectors. Therefore Eqn.2.20 is equivalent to the representation $X_{ij} = U_i^k s_k V_j^k$.

The vectors $\mathbf{v}^j$, called the principal axes, form an orthonormal basis on which the signal is decomposed. Since this basis diagonalizes the covariance matrix, it can be expected that it describes better the features of the whole signal, compared to other possible bases chosen a priori, such as the Fourier basis [47]. This is confirmed by the fact that, in practice, most of the **SU**s are very small compared to a few dominant ones. This explains why SVD is well known in the context of signal processing as a noise-filtering technique [47].

The projections of X along **V** (i.e. the product **SU**) are the principal components (PC) of **X**. They give the time evolution of the signal along the corresponding principal axes. This means that the original time series **x(t)** is now described as a sum of time series $x((i-1)t_s) = \sum_j u_i^j s_j \mathbf{v}^j$, each along the new coordinate axis $\mathbf{v}^{(j)}$. It is also possible to disregard as noise the components with **SU** below a given leve [47]. Since **S** corresponds to singular values, it is justifiable to assume that **U** is a representative of time bases.

Only the singular value **S** represents the amplitude of a mode. This has been confirmed by performing the following exercise. Consider an artificially generated signal having the form given in [47]

$$\begin{aligned} X_{ij} &= (1/\sqrt{N}) \sum_l a_l cos[2\pi m_l (j-1)/M \\ &\quad -2\pi\nu_l t_s (i-1)] \end{aligned} \tag{2.21}$$

This is a superposition of cosinusoids of mode number m_l, having the frequencies ν_l with amplitudes a_l, respectively, sampled at M equispaced coordinates with a timestep t_s. The indices 'i' and 'j' have their usual meaning. We have performed

SVD for a superposition of three cosinusoids having the same m_l but different a_l and ν_l. We find that doubling the amplitudes a_l doubles the singular values, leaving the basis vectors unchanged.

Now the matrix $\mathbf{X}_{ij}$ has been decomposed into three parts – time ($\mathbf{U}$), amplitude ($\mathbf{S}$) and space ($\mathbf{V}$). We have already seen that $\mathbf{U}$ and $\mathbf{V}$ are simply the basis functions and only the singular value $\mathbf{S}$ represents the amplitude. Hence, in the rest of the thesis, we treat the variation of S-values of different modes as representative of their respective strengths.

2.2.2 Conversion of SVD results to get distorted CNT shapes

Each set of three consecutive elements of the $\mathbf{V}$-vector corresponds to the change in x, y and z coordinates of one carbon atom, due to a particular mode. Let V_{kx}(i), V_{ky}(i) and V_{kz}(i) refer to the x, y and z displacements of the i^{th} atom due to the k-th mode. We can then write:

$$X_{distorted,i}(t) = Scale_k(t) * V_{kx}(i) + X_{original,i} \tag{2.22}$$

where $X_{original,i}$ is the x-coordinate of the i^{th} atom before starting the MD simulation, $X_{distorted,i}$ is the distorted x-location of the i^{th} atom due to this mode. Similar relations apply for the y- and z-directions. The scale factor is given by

$$Scale_k(t) = U_k(t)S_k \tag{2.23}$$

where S_k is the amplitude of the k-th mode as yielded by SVD, and U_k is the time series associated with the mode. The combined effect of 'N' modes on the ith atom can be obtained by superposition:

$$X_{distorted,i}(t) = \sum_{k=1}^{N} Scale_k(t) * V_{kx}(i) + X_{original,i} \tag{2.24}$$

The distorted positions can be used to compute the time series of average values, e.g., the average radius of a single ring of the SWNT, or the azimuthal rotation of each ring, the axial motion of each ring, and so on.

2.2.3 Advantages of SVD

A major advantage of SVD analysis is that is separates out modes in descending order of their amplitudes. This means that even fairly weak modes can be identified.

Note, however, that for a given initial perturbation, only certain modes may be strong enough to be isolated. If the intention is to study the evolution of a specific spatial mode, the MD simulation can be started to excite that particular distortion in the SWNT, so that that mode becomes stronger. In the present work, we study the modes of an SWNT and a DWNT using SVD analysis on the MD results. This method offers three advantages:

- Firstly, it can, in principle, resolve the modes of a system in order of the hierarchy, including the associated frequencies as well as spatial distortions.
- Secondly, it can handle small as well as large-amplitude perturbations given to the system to excite these modes, i.e., SVD can identify an-harmonic behavior as well.
- Thirdly, while the present study covers only SWNTs and DWNTs, it can readily be extended to much more complex structures.

Other techniques to extract the characteristic modes of a carbon nanotube and their differences with the SVD technique will be discussed in detail in Chapter 4.

Chapter 3

Molecular Dynamic simulations of a double-walled carbon nanotube motor subjected to a sinusoidally varying electric field

3.1 Introduction

As explained in Chapter 1, one potential application of carbon nanotubes is in the field of nanomachines or nanodevices. This field has attracted many researchers because of the various potential applications of nanomachines in the field of computing, electronics, robotics and drug delivery [23, 24, 28, 29, 48]. These nanometer devices, either alone or attached to a propeller, are a bright candidate for future machines which could be used for medical applications [30, 49, 50]. Our interest is in nanometer-sized devices, especially nanomotors based on CNTs, which are of interest for applications in novel drug delivery techniques [30]. Such nanometer systems need stimulation by an external medium like a laser [23], gas [51] or ion-gradient [25].

Tuzan et. al [23] studied the laser excitation of such a nanometer-scale motor, consisting of a DWNT. Such a configuration is revisited in this work where the inner CNT behaves as a "shaft" while the outer CNT serves as a "sleeve", as shown in Fig. 3.1. Two diametrically-opposite atoms on the shaft are assumed to carry unit electric charges with opposite sign. Such a situation could be created by the presence of two dopant atoms, one with a smaller electronegativity than carbon on

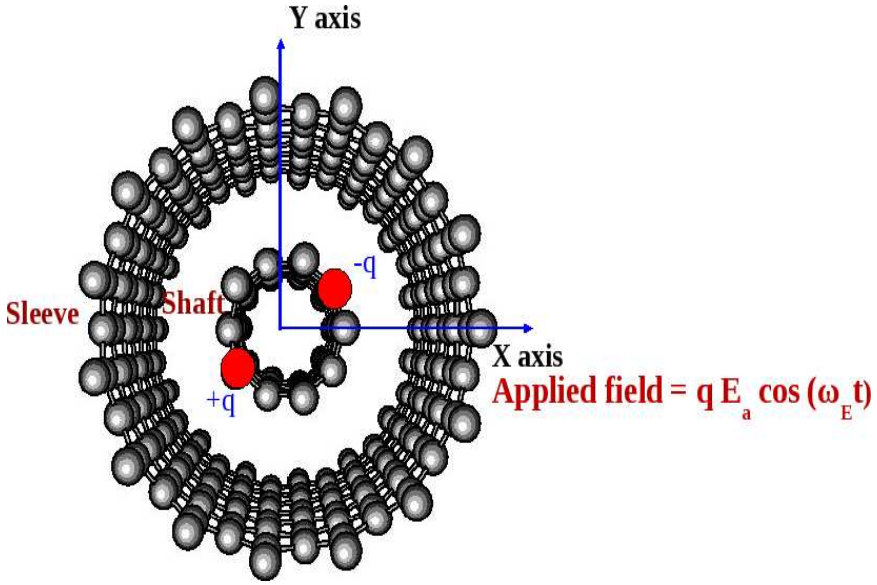

Figure 3.1: End-on view of the DWNT configuration. A sinusoidally-varying electric field having only an x-component, is applied to the system. Two diametrically-opposite atoms on the first ring, nos. 1 and 6, are assumed to have equal but opposite electric charges. At t=0, the line joining the two diametrically opposite atoms no. 1 and 6 makes an angle of 20 deg with the direction of applied electric field (X axis).

one side and the other with a higher electronegativity than carbon on the other side of the shaft. When the system is exposed to a large-amplitude, linearly polarized electric field, the force acting on the two charged atoms produces a torque, leading to rotation of the shaft about its axis.

Tuzan [23] performed simulations of such a motor using molecular dynamics with an empirical Lennard-Jones 6-12 potential for the intertube interaction (i.e for interaction between the two nanotubes) and a three-body interaction term for the intratube interaction (interactions within the carbon atoms within a nanotube). In their studies, the sleeve was held fixed – configurations with both the shaft and sleeve moving were not explored. Also, the DWNT considered in Tuzan's [23] work did not satisfy the conditions of a 'real' DWNT, since the gap between the two carbon nanotubes was greater than that observed experimentally [36, 37]. Servantie et al. [26] studied the drag force between two coaxial CNTs when they are set into relative angular motion, making use of the Brenner potential [34] for intra-tube interactions and the Lennard-Jones (LJ) potential for interactions between the tubes. They studied the role of translational sliding motion and dynamic friction for axial rotation of the inner nanotube in DWNT systems using MD and showed that the dy-

namic friction is linear in angular velocity for a wide domain of armchair-armchair, zigzag-armchair and zigzag-zigzag double walled CNT's.

We use the Brenner potential, which is a reactive, empirical, many body potential-energy expression that can model intramolecular chemical bonding in a variety of small hydrocarbons [34] to model the DWNT configuration shown in Fig. 3.1. The inter-tube interactions are simulated by Nordlund's long-range interaction correction [35]. Apart from the cases studied in [23] where the shaft was moving and the sleeve was held fixed, we also study the cases where both the shaft and the sleeve are moving.

3.2 Description of the simulations

SWNT in zig-zag configurations (5,0) and (15,0), of lengths 9.94 and 12.52 Å respectively are used in our simulations as shaft and sleeve. The co-ordinates used and the end-on configuration of the nanomotor are shown in Fig. 3.1. Both the shaft and the sleeve are centered about a common rotational axis (**Z** axis).

3.2.1 Initializing atomic positions and velocities

The initial positions of the shaft and the sleeve are generated using the method as in [52]. Berendsen's temperature [44] and pressure controls are used to scale the atomic velocities and positions respectively. The scaling parameters are chosen in such a way that the velocity distribution is close to the desired Maxwellian. In order to check this effect, we monitor the velocity distribution obtained during the NPT relaxation of the entire DWNT assembly as discussed in the last chapter and make sure that it is close to the desired Maxwellian distribution. The temperature is also observed to be at 300 K as explained in Chapter 2.

3.2.2 Equilibration of the structure

After placing the shaft inside the sleeve, the structure is equilibrated at a temperature of 300 K and zero pressure, using Berendsen's temperature and pressure control [44] with a time constant of 500 fs for simulations of 100 ps. The equilibrated structure is found to have a shaft and a sleeve of diameter 4.55 Å and 12.04

Å respectively. This is calculated at the end of the NPT relaxation run, and the radius of each CNT is calculated as the mean radius measured from the instantaneous centroid of that CNT. Thus we find a radial gap of 3.74 Å between shaft and the sleeve at the end of the NPT relaxation. Given the difference in the potentials with other workers, this is fairly close to the standard 3.4 - 3.6 Å gap reported for normal DWNTs [36, 37]. Before starting a real MD simulation, after the NPT relaxation we make sure that the total energy and the pressure of the system is close to the desired value as explained in appendix A.

3.2.3 Periodic boundary conditions used

Periodic boundary conditions (PBC) are used along the **Z** axis for all atoms in the simulation, be it those of the shaft or sleeve. This is because we want the structure to repeat along the length of the CNT to get an infinite length structure. PBC's are imposed through minimum image convention method which calculates forces on each atom over and above periodic handling of any atomic border crossings as explained in Chapter 2.

3.2.4 Application of an external field

After relaxation of the DWNT structure, unit positive and negative charges are assumed on two diametrically opposite first and sixth atoms of the inner nanotube as shown in Fig. 3.1. The line joining these two atoms is observed to make an angle of 20 degree with the X axis. An external electric force of the form:

$$qE_a\ cos(w_E t), \tag{3.1}$$

is applied to the already existing inter-atomic potential force term for the two charged atoms, where ± q is unit charge assigned to atoms 1 and 6, and E_a denotes the applied electric field strength. Simulations for a field strength in the range of 3×10^8 V/m - 3×10^9 V/m are performed. ω_E is the frequency ($= 2.045 \times 10^{10}$ rad/sec) of the applied field. MD time step of 0.1 femto-second is used and the simulations are run for 800 ps.

The applied field produces an equal and opposite force on the two charged atoms which produces a torque on the two atoms and induces rotations in the system.

These rotations are however not rigid body rotations since we see some distortions in the shape of the shaft due to the high amplitude electric field acting on it and the effect of these distortions will be taken into consideration when we explain our results in the later sections. The instantaneous value of the angular velocity (rad/sec) for both the shaft and the sleeve are calculated as:

$$\omega(t) \;=\; \frac{L_z(t)}{I_z(t)} \tag{3.2}$$

where $L_z(t)$ and $I_z(t)$ are the instantaneous angular momentum and moment of inertia of the shaft about the z-axis. These terms, in turn, are defined as:

$$L_z(t) \;= \sum_{i=1}^{N} I_{i,z}(t)\omega_{i,z}(t) \tag{3.3}$$

and

$$I_z(t) \;=\; \sum_{i=1}^{N} M_i R_i(t)^2 \tag{3.4}$$

where N is the number of atoms in the shaft, M_i is the mass of the $i-th$ atom, $R_i(t)$, $\omega_{i,z}(t)$ and $I_{i,z}$ are the instantaneous values of the radial location, angular velocity and moment of inertia of the i_{th} atom, measured with respect to the instantaneous centroid of the shaft. All the above mentioned quantities are calculated at every timestep in the MD simulation, making use of instantaneous velocities and coordinates of all atoms in the shaft.

3.2.5 Types of simulations performed

Two sets of simulations are performed. In the first case both the shaft and the sleeve are allowed to move. In the second set of simulations the shaft is kept free to move but the sleeve is held fixed. Two locked states are observed for angular rotation of the shaft in the fixed sleeve case, caused by minor shape changes of the shaft due to the effect of the applied electric field on the atoms with assigned charges. The simulation results for the values of drag co–efficient are in the range reported by Servantie [26]. All these simulations are performed using the NVT ensemble in the MD simulations as we expect the nanomotor to be in thermal equiliibrium with the surroundings. Finally we simulate the effect of the absence of heat losses (or the effect of insufficient heat losses) for the nanomotor configuration by doing an NVE MD study, without temperature control.

3.3 Case 1 : Both shaft and sleeve moving

3.3.1 Molecular Dynamics results

In this case rotary behavior is observed for a very small period of time accompanied with the usual pendulum like oscillations. The typical angular velocities (in rad/sec) for the shaft and the sleeve for an applied field of 3×10^9 V/m and angular frequency of 2.045×10^{10} rad/sec are as shown in Fig. 3.2.

(i) (ii)

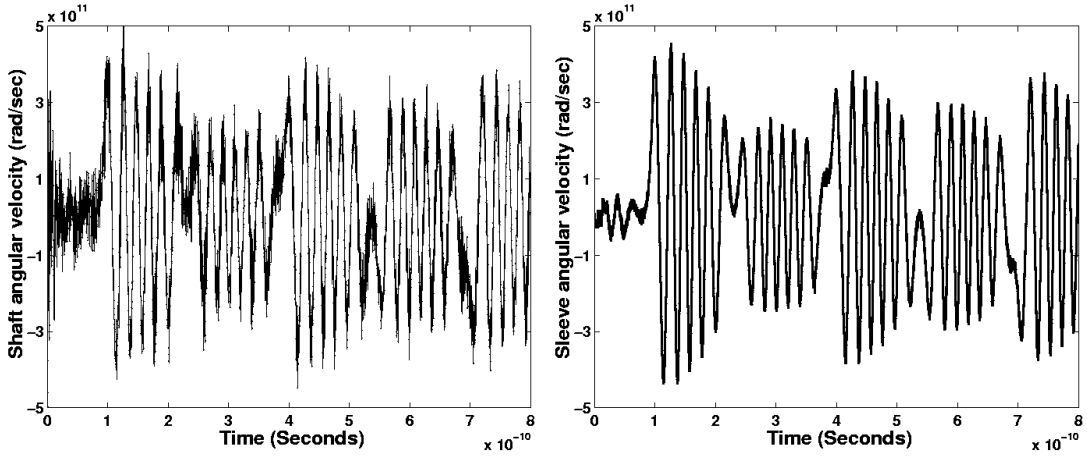

Figure 3.2: (i) Angular velocity (rad/sec) of shaft (ii) Angular velocity (rad/sec) of sleeve.

In Fig. 3.2 we see that there is no significant angular velocity gain in the first 100 ps for both, the shaft and the sleeve. This is because, initially the shaft and therefore the sleeve, due to the drag forces, are accelerated through only 20 degrees to align with the electric field directed along the **X** axis and oscillate around it. For the shaft, we see some thermal fluctuations present in this period. Note that the angular velocity in Fig. 3.2 is plotted using a moving window average over 1000 MD data points because of large number of data points obtained from MD. The total angular momentum for the motor is plotted in the Fig. 3.3.

The momentum values oscillating between both positive and negative values indicate a pendulum like behavior and decaying and then building up of angular momentum without change of sign indicates a motor like behavior. This motor like behavior is observed only when the electric field changes sign as is seen in

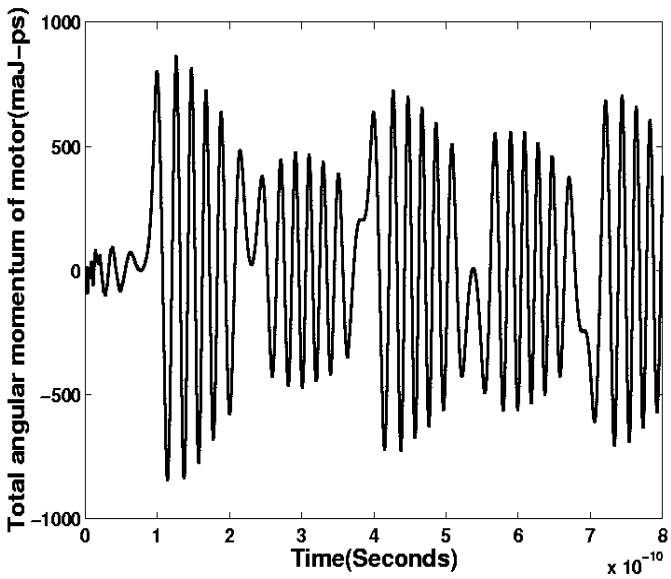

Figure 3.3: Total angular momentum (maJ-ps) of the motor at 300 K for a simulation run for 800 ps.

Fig. 3.4 where we plot the angular orientation, θ, of the shaft-sleeve configuration as a function of time.

As explained before, the atoms with charges show angular oscillations around the direction of the electric field. The frequency of the electric field is much lesser than the oscillation frequency of the shaft and the sleeve. When the electric field changes sign, depending on their phase of oscillation, the shaft-sleeve configuration flips either clockwise or anti-clockwise, to align with the changed direction of the electric field. Increasing the frequency of the applied electric field to 2.045×10^{11} rad/sec makes these flips faster.

3.3.2 Effect of field amplitude on shaft angular velocity

To see the effect of field amplitude on the shaft frequency a set of simulations are done by varying the amplitude of the applied electric field. Fig. 3.5 shows the temporal variation of the angular velocity of the shaft for three different amplitudes of the applied electric field, viz., 3.2×10^9, 3.4×10^9 and 3.6×10^9 V/m. We see that the amplitude of angular velocity increases monotonically with the amplitude of the applied field.

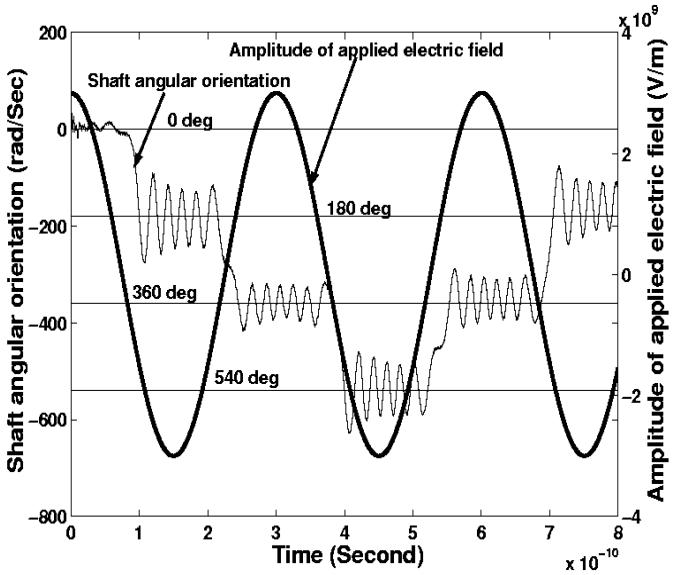

Figure 3.4: Temporal variation of the shaft angular orientation (θ) inside the sleeve and the scaled applied electric field (Applied electric field amplitude is 3×10^9 V/m here).

3.3.3 Theoretical model results

The motion of the system is now solved by a set of three coupled ordinary differential equations (ODE) using the fourth order Runga-Kutta method for the case where both the shaft and the sleeve are free to move. The model generally follows the ODE model used by [26] with some modifications. We also take into account the time variation of the moment of inertia of both shaft and the sleeve. The drag force acting between the shaft and the sleeve is given in terms of the difference of the angular velocities of the shaft and the sleeve as in the model of [26]. The model is as follows:

$$\frac{d}{dt}(I_1\omega_1) = -\tau_{12} + E_a cos(w_E t) \times 2qR_a sin(\theta_E) \quad (3.5)$$

$$\frac{d}{dt}(I_2\omega_2) = \tau_{12} \quad (3.6)$$

$$\frac{d}{dt}(\theta_E) = \omega_1 \quad (3.7)$$

$$\tau_{12} = k\,(\omega_1 - \omega_2) \quad (3.8)$$

Where, τ_{12} is the drag force acting between the shaft and the sleeve, k is the drag coefficient, R_a is the shaft radius and q is the unit electronic charge. E_a and ω_E are the amplitude and frequency of the applied electric field and θ_E is the angle which the line joining the two charged atoms make with the electric field. The initial value

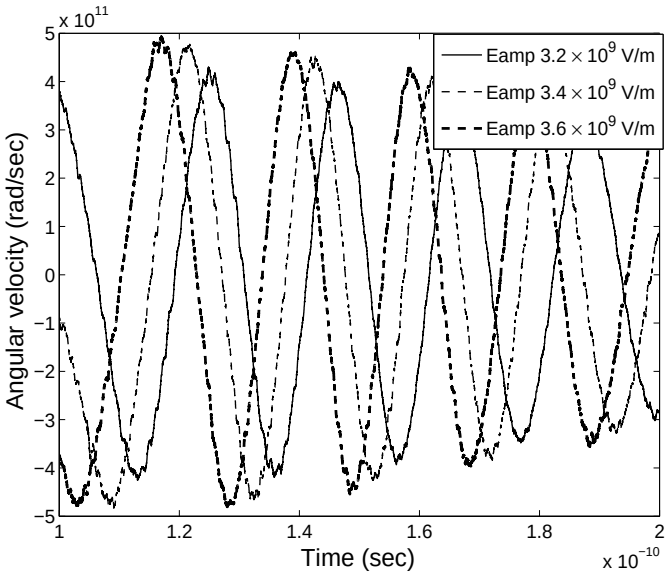

Figure 3.5: Temporal variation of the shaft angular velocity (rad/sec) for three different amplitudes of applied electric field 3.2×10^9, 3.4×10^9 and 3.6×10^9 V/m (Note that the angular velocity is plotted for the period 100-200 ps).

of θ_E, I_1, I_2 and R_a are obtained from MD. θ_E is 20 degree for this case. The instantaneous values of I_1 and I_2 are obtained from MD. Solving these equations numerically using a fourth order Runga-Kutta method we get the instantaneous values of ω_1 and ω_2.

3.3.4 Drag coefficient calculation

After setting up the ODE model, we try to get an approximate solution to these equations by varying the value of drag coefficient k over the range 0.95×10^{-29} - 1.09×10^{-29} Nms. A value of k = 0.95×10^{-29} Nms gives ω lesser in amplitude then the MD value, and k = 1.09×10^{-29} Nms overestimates this value. This implies that the angular velocities of the shaft and the sleeve are highly sensitive to k. We observe that an approximate value of k equal to 1.03×10^{-29} Nms gives a qualitatively good match with our MD results. This value of drag coefficient is in good agreement with that reported in [26].

3.3.5 Comparison with MD results

A comparison of the angular velocities obtained with the ODE model (with k = 1.03×10^{-29} Nms) with that of the MD results are shown in the Fig. 3.6. Qualitatively there is a fair match with the MD results. But at some points there

(i) Shaft angular velocity (rad/sec) (ii) Sleeve angular velocity (rad/sec)

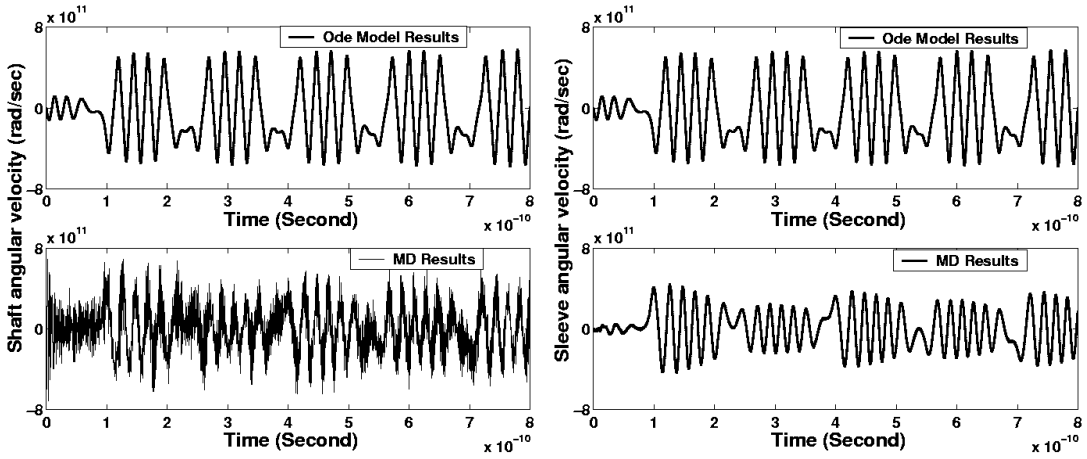

Figure 3.6: Comparison of the angular velocity (rad/sec) of the shaft and the sleeve obtained from the "ODE model" with that of "MD" with both the shaft and the sleeve moving.

are some mismatches also like:

- The start up behavior of the shaft and the sleeve angular velocities obtained with this model does not follow the trends as we see in our MD results.
- At the time points where rotary behavior is observed the angular velocity shows opposite sign as that to the MD results.

These mismatches could be because of the temperature effects and the kind of potential used in the MD which are not taken into account in this model. Using the results from this study we fitted an expression for the drag between the shaft and the sleeve.

3.4 Case 2 : Fixed sleeve case

3.4.1 Molecular Dynamics results

In this subsection we give the MD results of the case where the sleeve is kept immobilized. Such a configuration can be useful for the future applications of nano-devices where one would like to keep the sleeve fixed and attach it to some other nano-meter sized assembly. At first sight, it seems reasonable to assume that the drag torque should follow a similar form with and without the sleeve movement. This is then examined in this subsection. Only the usual radial breathing of the shaft [53] is observed in this case. This is due to the high drag force between the shaft and the sleeve due to the fact that atoms have to overcome potential barriers as atomic surfaces move with respect to each other [26, 48]. A higher amplitude electric field therefore would be required for the rotation of the shaft inside the fixed sleeve.

3.4.2 Potential energy surface (PES) calculation

In order to quantify the electric field required to overcome the drag force, we map the whole Potential energy surface (PES) of the system by giving small rotations of 0.1 degree each to the shaft and finding out the total potential energy ϕ of the system at each step. A plot of the PES with the starting configuration of the DWNT system before the temperature and pressure thermalization is shown in Fig. 3.7 (i). This PES gives 15 peaks, which is in agreement with Merkle's [54] formula for the periodicity of the potential energy of such a DWNT configuration. The number of peaks depend on the number of atoms in the outer and inner nanotube. However after relaxing this structure at 1 atmosphere pressure and 300 K temperature using MD, one global maximum and two nearly equal global minimas in the PES are observed as seen in the Fig. 3.7 (ii).

3.4.3 Threshold electric field calculation

The gradient of the PES plot along θ is calculated as shown in the Fig. 3.7 (iii). The threshold electric field $E_{threshold}$ required for the rotation of the shaft inside the fixed sleeve is given in terms of this gradient in θ as follows:

$$qR_aE_{threshold} = d\phi/d\theta, \tag{3.9}$$

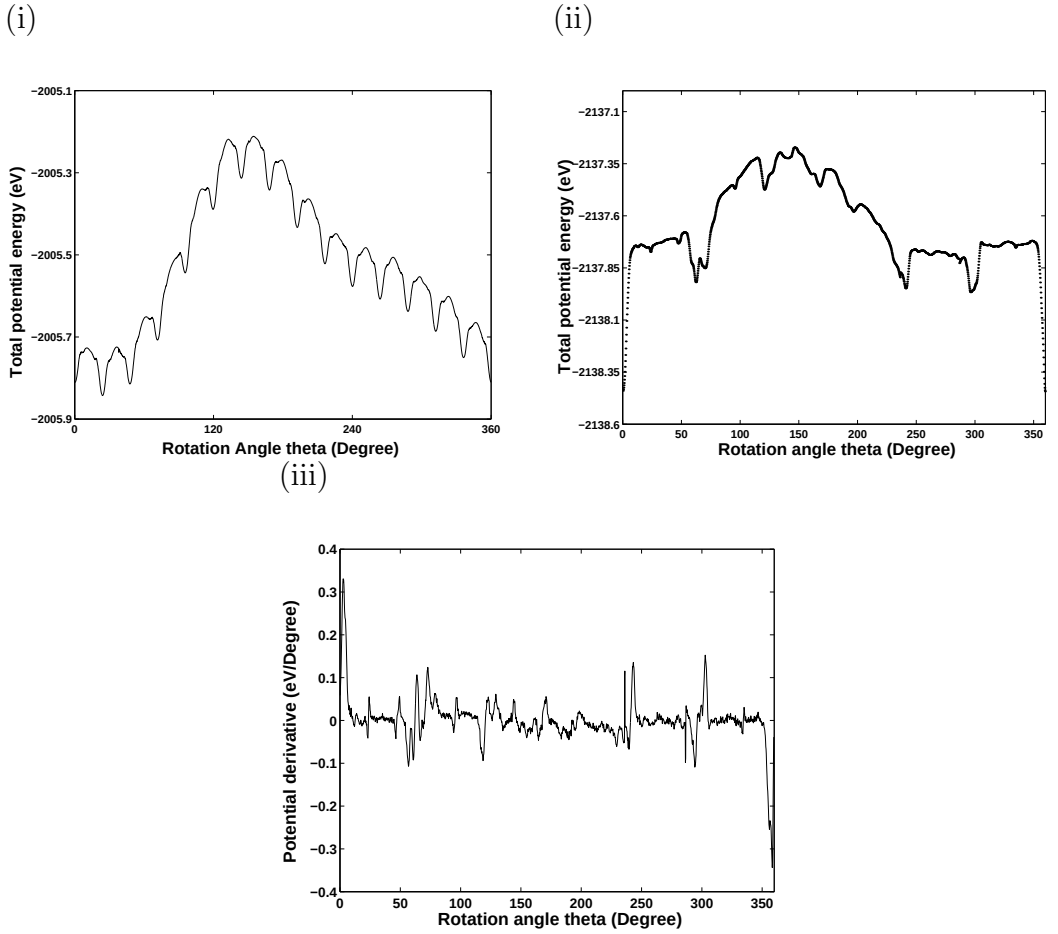

Figure 3.7: (i) Total potential energy (eV) of the system as a function of angular orientation of shaft (θ) inside the immobilized sleeve before thermalization. (ii) Total potential energy (eV) of the system as a function of the angular rotation of the shaft inside the fixed sleeve after thermalization. (iii) Derivative of the total potential energy (eV) with θ (deg).

Where $E_{threshold}$ is the threshold electric field, ϕ is the total potential energy of the system, θ are the small angular rotations of 0.1 degree each given to the shaft, q is the electronic charge and R_a is the radius of the shaft. In the ideal case, relaxed DWNT case, we find that $E_{threshold} = 3.69\text{x}10^{10}$ V/m.

However we find that this simplistic argument for overcoming the potential barrier for rotation is not sufficient to produce rotation. It is only after applying an electric field of amplitude 4.43×10^{10} V/m we observe rotation in spurts, with the inner nanotube spending most of its time in two different locked states in the angular orientation of the shaft inside the fixed sleeve as seen by the flat regions in Fig. 3.8.

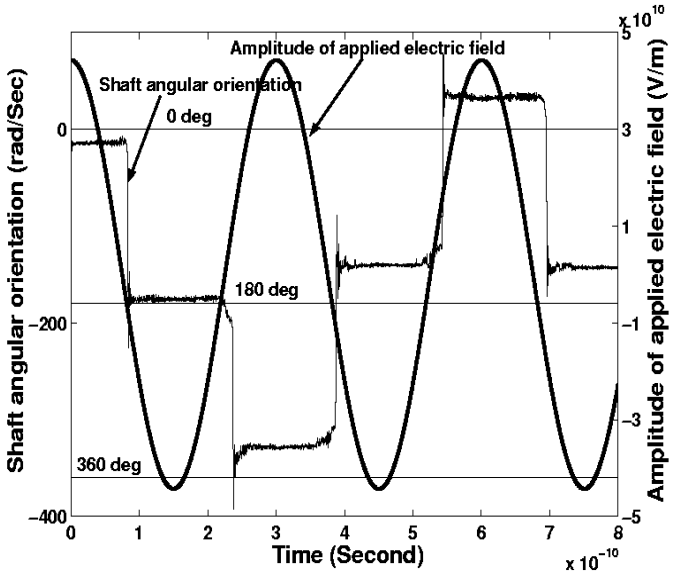

Figure 3.8: Temporal variation of shaft angular orientation θ (deg) inside the fixed sleeve and the scaled applied electric field (Applied electric field amplitude is $4.43 \times 10^{10} V/m$ here).

The straight lines at 0, 180 and 360 deg in the plot correspond to the direction of the applied electric field. Note that the observed locked states are not in the direction of the applied field unlike the first case where both the shaft and sleeve are free to move.

3.4.4 Theoretical model results

For the second case where the sleeve is held fixed, $\omega_2 = 0$, so the system of Eqns. 5.3-5.5 reduces to

$$\frac{d}{dt}(I_1\omega_1) = -\tau_{12} + E_a cos(w_E t) \times 2qR_a sin(\theta_E) \tag{3.10}$$

$$\frac{d}{dt}(\theta_E) = \omega_1 \tag{3.11}$$

$$\tau_{12} = k(\omega_1) \tag{3.12}$$

we expect the drag force to be high in this case as compared to the first case since ω_2 is zero here. It is easy to see that the this simple theoretical model does not reproduce the observed locked states, which are not aligned parallel to the electric field. For locked states $\omega_1 = 0$ and Eqns. 3.10-3.12 gives only the trivial locked states in the direction of the applied field.

For one more case with $\omega_E = 2.045 \times 10^{11}$ rad/sec and same value of applied electric field amplitude as earlier we compare the theoretical model results with MD. As seen in Fig. 3.9 (i) model gives constantly decaying oscillations of the shaft angular orientation, θ inside the sleeve. Different locked states can be seen in θ values obtained from MD as seen in Fig. 3.9 (ii). In the next section we show that the observed locked states are a result of radial shape changes and centroid shift of the shaft due to the external applied electric field. This implies that Eqn. 3.12 needs to be modified to include these effects.

(i) (ii)

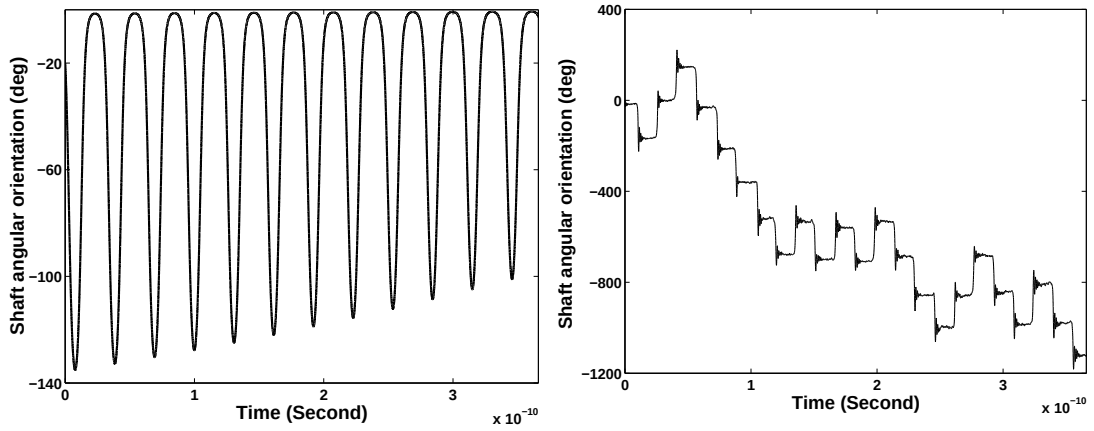

Figure 3.9: Temporal variation of the shaft angular orientation θ inside the fixed sleeve (i) Model Result (ii) MD result.

3.5 Fixed sleeve case with $E_{applied} > E_{threshold}$

We observe that the shaft has certain locked states, as indicated by the flat regions for the angular orientation, θ, as a function of time in Fig. 3.8. Note that these locked states need not be in the direction of the electric field unlike the case where both the shaft and the sleeve are free to move. Note further that the transition between these locked states occurs only when the applied external electric field changes direction. These states are explained in terms of

- Radial shape changes of the shaft, and
- Shift in the centroid position of shaft inside the sleeve.

By centroid shift we mean the shift in the location of the shaft center (x_c,y_c). The above two causes for the locked states are addressed in more detail in the next two subsections.

3.5.1 Radial shape changes of the shaft

The electric field preferentially acts only on the atoms to which charges are assigned (atoms 1 and 6) and moves them. The other atoms of the shaft respond to the positional changes of these atoms through the interaction potential. This asymmetric external force leads to radial shape changes of the shaft. Fig. 3.10 shows the radial variation of these two atoms (normalized to R_{shaft}) and the variation of the applied electric field (scaled to fit in the graph) as a function of time. Note that the radial

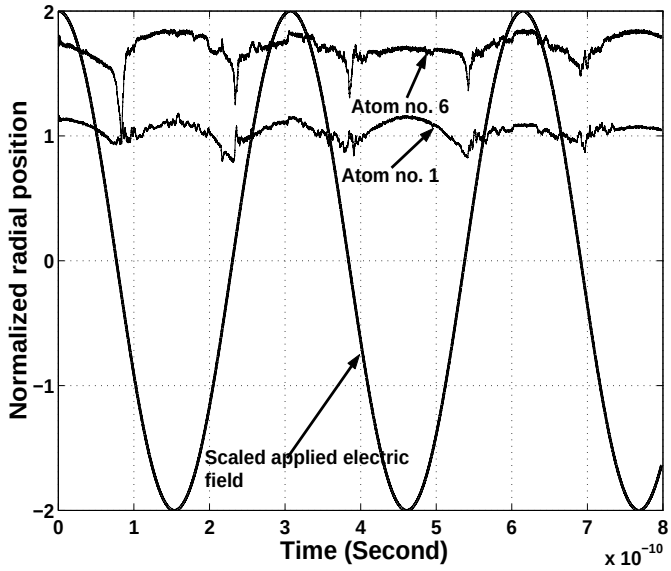

Figure 3.10: Variation of radial positions of atom nos. 1 and 6 (normalized to the R_{shaft}). Note that at the point of transitions in θ like at 8.25×10^{-11} sec and 2.37×10^{-10} sec, radial positions of these two atoms become close to 1.

position of both these atoms (specially atom no. 6) is much greater than unity most of the times, implying radial shape change of the shaft. It is only when the electric field flips direction, that the radial positions of these atoms comes close to R_{shaft}, thereby decreasing the shape change. This reduction in the radial positions of these two atoms when the applied electric field changes sign makes the interaction between the shaft and the sleeve weak, thereby facilitating the flip from one locked state to another. Note that the flip occurs at values of electric field lesser than the

threshold electric value ($E_{threshold}$ = 3.69x10^{10} V/m) obtained by our static analysis with no shape change. This indicates that dynamic shape change make pathways for rotation.

Fig.3.11 (i) and (ii) shows the shape of shaft inside the sleeve before and after the dynamic shape change, respectively. Fig. 3.11 (i) shows the shape of the shaft after

(i) Shaft before applying electric field to it.

(ii) Shaft after applying electric field to it.

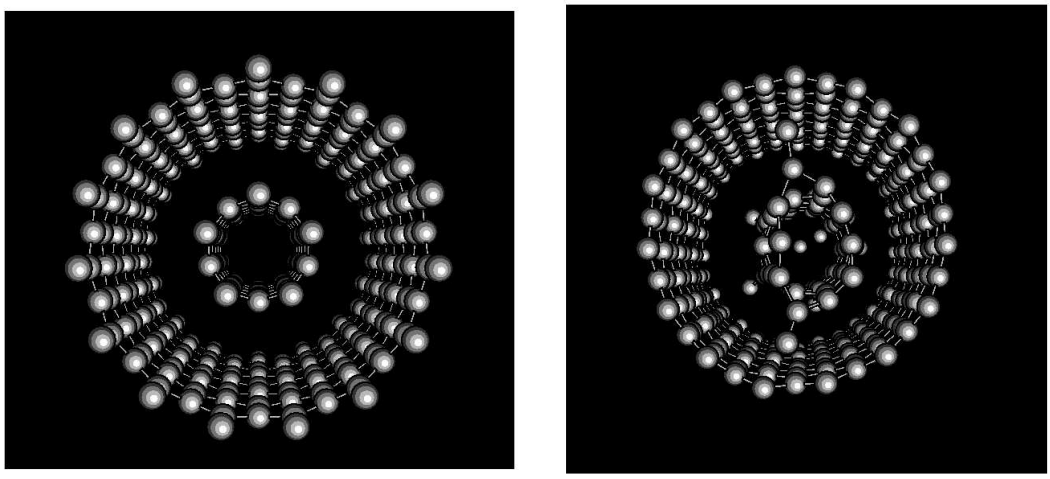

Figure 3.11: Shape of the shaft inside the sleeve before and after applying electric field to it. Note that the distortions are produced in the shaft due to the stretching of charged atoms, after applying an electric field to it.

the NPT relaxation and Fig. 3.11 (ii) shows distortion produced in it due to the stretching of the two charged atoms due to the application of an electric field. A cross-section of the PES, as shown in Fig. 3.12, is then obtained from this distorted configuration, following the method described in subsection 3.4.2. The initial atomic coordinates for this are taken from the MD output at 10 ps, where we see a significant distortion in the radial locations of atoms no. 1 and 6. Rotations are done in steps of 0.2 deg each to cover a full rotation of 360 deg. Fig. 3.12 shows that the

minimum energy state occurs at 170 deg, which is also the location of the locked state of the shaft inside the fixed sleeve.

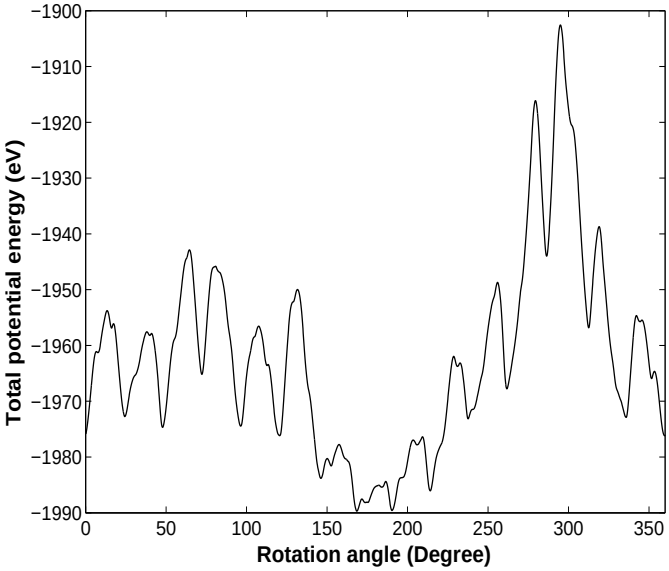

Figure 3.12: PES plot of the shaft inside the fixed sleeve after dynamic shape change produced in it due to the stretching of the charged atoms on application of electric field to it.

3.5.2 Shift in the centroid location

In the ideal case, the centroid position of the shaft in the sleeve, x_c and y_c should be (0,0). However, as seen in Fig. 3.13 (i) x_c is 0.77 Å and y_c is remains close to 0.0 near the first flip, i.e at 8.25×10^{-11} sec. Note that there is a significant shift in x_c and y_c near all the transition points in θ which occur with a change in the applied electric field direction. In order to interpret the transition between these locked states in terms of applied electric field, radial shape change and shift in centroid location, we plot the scaled applied electric field, change in the the scaled radial positions of atom no. 1 and 6, shift in centroid location (x_c,y_c) and the angular orientation θ of the shaft for the first four transitions in Fig. 3.14 (i-iv). We make the following general observations:

- First the applied electric field changes direction, followed by radial position change of atoms 1 and 6. This is then followed by a shift in centroid location, after which a transition between the locked states occurs.

- The radial position of atoms 1 and 6 are usually greater that the average shaft radius. In these simulations, we see that atom 6 has a higher deviation from the average value than atom 1. This is probably because the relaxation of the shaft in the sleeve does not yield a perfectly θ symmetric configuration.

- Large shifts in the centroid location are seen even at times where there are no transitions between the locked states. However in these cases, the radial deviations of atoms 1 and 6 from their average value are large and therefore this seems to be a necessary condition for the transitions.

(i) Shift in x coordinate of centroid (x_c). (ii) Shift in y coordinate of centroid (y_c).

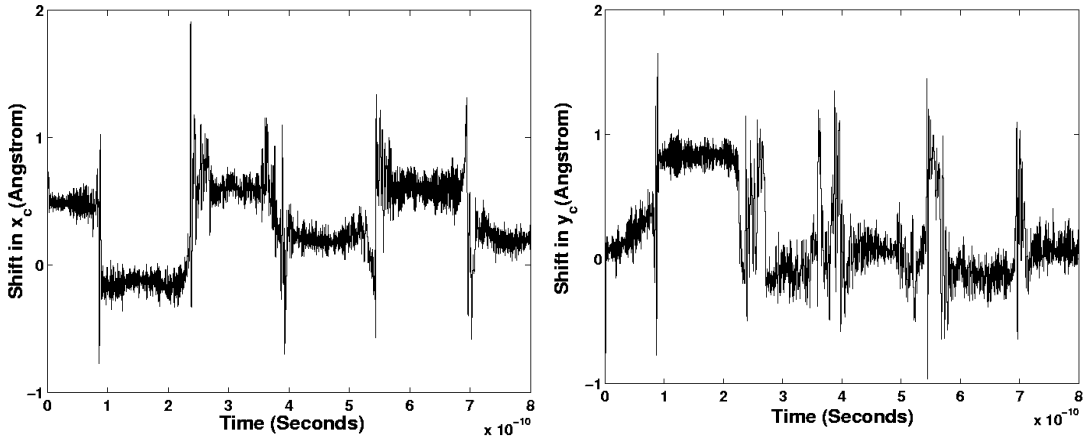

Figure 3.13: Temporal variation of the shaft centroid location.

3.6 Simulations with no temperature control

The foregoing simulations have been done with the temperature maintained constant at 300 K. This means that part of the energy poured into the system by the applied electric field is taken away by a constant temperature bath. Hence the DWNT is not allowed to heat up. In reality, however, the device would have a finite heat transfer rate to the surroundings, due to conduction and convection. This means that the temperature could rise. It is thus of interest to examine the performance of the device in the limit of no energy loss, i.e., without any temperature bath attached to it. A constant energy simulation, NVE, is performed to study this effect. All

other parameters are kept as before. The simulation is run for 800 ps. Pendulum-like oscillations are seen for the first 300 ps but after that the motor breaks apart. Since the Brenner potential does not accurately reproduce chemical reactions, the process of breakup yielded by these simulations is not likely to be accurate. Hence the detailed results are omitted here.

3.7 Conclusions

A DWNT configuration consisting of a shaft (inner nanotube) and a sleeve (outer nanotube), which has been used to simulate a nanomotor [23], has been revisited using MD with a better interatomic potential. This motor is stimulated by an externally applied sinusoidally varying electric field. New situations, like keeping the sleeve mobile and the effect of temperature on the nanomotor configuration have been studied. Two different locked states are observed in the angular orientation of the shaft inside the fixed sleeve, which precludes the motor- or even the pendulum-like behavior for the parameters used in this study. This is due to radial shape changes and shift in the centroid location of the shaft. The frequency of shift between these two locked states correspond to the frequency of the applied electric field. In the case where the sleeve is not fixed, angular oscillations of the whole assembly around the direction of the electric field are observed with motor-like behavior occurring only with a change in the direction of the applied electric field. Since it is interesting to examine the performance of such a device in the limit of no energy losses, we simulate the behavior of the motor in the absence of any heat bath attached to it and observe that the motor breaks apart in this case.

In Chapter 5, we study the effect of applying different electric field frequencies and amplitudes, with the objective of determining the useful parameter space for pure motor-like behaviour.

(i) At 1st transition in θ.

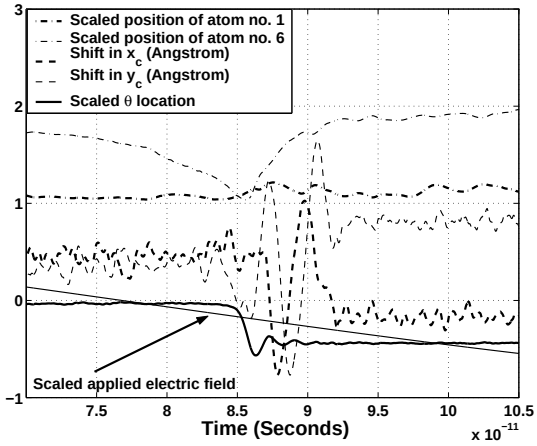

(ii) At 2nd transition in θ.

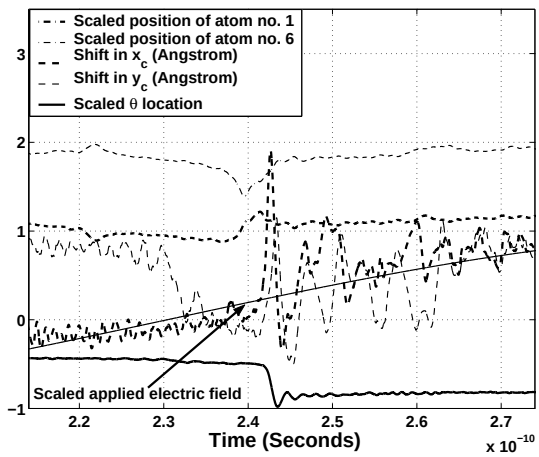

(iii) At 3rd transition in θ.

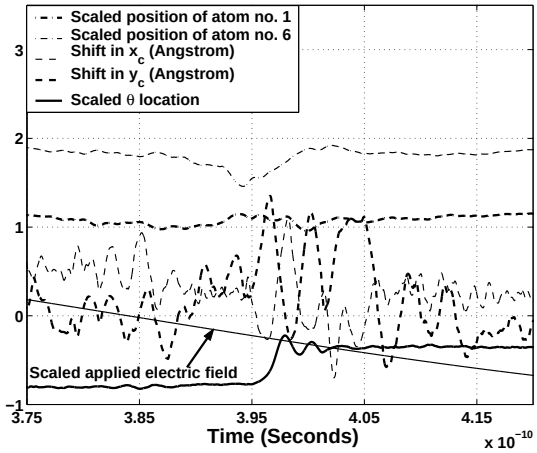

(iv) At 4th transition in θ.

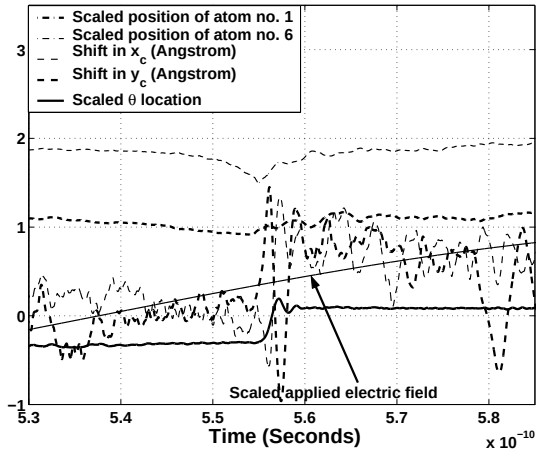

Figure 3.14: Plots showing the variation of scaled applied electric field, scaled radial positions of atom no. 1 and 6, shift in centroid location (x_c,y_c in Å) and scaled shaft angular orientation θ.

Chapter 4

Mode analysis of Carbon nanotubes based on Molecular Dynamics : A Singular Value Decomposition study

4.1 Introduction

The nanomotor discussed in this thesis involves a DWNT, with the outer CNT behaving as a sleeve and the inner one as a shaft. Charges are assumed to be placed on two diametrically-opposite atoms on one ring of the shaft, and is made to rotate by the application of an external electric field [23, 55]. The ideal situation would be for the sleeve and shaft to exhibit rigid body rotation about their common axis, like an ideal motor. However, at these scales, apart from pure rotation, the CNTs exhibit rather complex motion involving distortions of various types as discussed in the last chapter. Hence it behaves as a 'non-ideal motor'. These distortions are particularly prominent in the case of externally-driven systems, as seen in [55]. In a DWNT-based nanomotor driving a propeller, complex motion of the shaft would translate into complex motion of the propeller. Hence it is necessary to understand this non-ideal behavior of CNT-based nanomotors. Such complex motions can often be resolved into the normal/characteristic modes of the structure. Hence it is important to develop a good understanding of the modes of a SWNT and DWNT, which forms the subject of this chapter. The knowledge of the characteristic modes is also

necessary from the point of view of application of these SWNTs for nano-devices, where excitation at a particular mode frequency can give rise to resonance excitation, which can then be used for extracting useful work from the device.

The simplest mode, involving in-phase radial movement of the carbon atoms of an SWNT, is called the radial breathing mode (RBM). The RBM frequency is given by

$$\omega_{RBM} = A/d \tag{4.1}$$

where A is a constant derived experimentally [56] and d is the diameter of the nanotube. Normal modes of CNTs have been studied experimentally using Raman Spectroscopy [31, 57–60]. Raman spectra are obtained using a high intensity laser field, such as that of an argon-ion laser [60]. The number of Raman-active vibrational modes is just 15 or 16 [61], and includes modes like A_{1g}, A_{2g}, E_{1g} and E_{2g} [3]. Even out of the Raman-active modes, only four bands are strongly resonance-enhanced and hence can be identified easily in experiments [53,57,62,63]. Out of these modes, RBM gives the most intense Raman signal and can be used for nanotube characterization. Thus RBM remained the most widely explored mode for the purpose of nanotube characterization.

Theoretically, the modes of an SWNT have been studied using Density Functional Theory (DFT) [61] and also using classical Molecular Dynamics [60] simulations. Kurti [53] used DFT, applying a plane wave basis set and extracted out RBM frequencies of 40 different SWNT with small diameters. Nachiket [62] studied the temperature dependence of RBMs with classical molecular dynamics (MD) simulations using the Tersoff-Brenner potential and also verified it using Raman spectroscopy. Popov [64] calculated radial breathing and G-band vibrational modes of SWNT calculated within a symmetry-adapted non-orthogonal tight-binding (TB) model. The dynamical matrix was calculated using the linear-response approximation within the TB approach. Dobardzic [65] used a simple analytical model for studying the breathing-like phonon modes in case of a DWNT where the tube walls were treated as coupled oscillators. In all these theoretical studies, the main focus remained on the RBM, since it is unique to nanotubes without any counterpart in graphene sheets and it gives important information for the nanotube characterization.

In this chapter, we first present the characteristic modes of an SWNT in detail,

obtained using Singular Value Decomposition (SVD) analysis on the MD results. Later we repeat the same analysis for a DWNT, which is discussed in the later part of the chapter.

4.2 Phonon Modes

The most commonly determined characteristic modes of a system are discussed in terms of the phonon modes/branches of the system.

The phonon frequencies ω as a function of the wave vector k can then be obtained by solving the secular equation [66] :

$$\det \left| \frac{1}{\sqrt{M_s M_t}} C_{st}^{\alpha\beta} - \omega^2(k) \right| = 0 \tag{4.2}$$

Where M_s and M_t are the masses of the atoms t and s and the dynamical matrix is defined as:

$$C_{st}^{\alpha\beta}(k) = \frac{\partial^2 E}{\partial u_s^{\alpha}(k) \partial u_t^{\beta}(k)} \tag{4.3}$$

where u_s^{α} denotes the displacement of atom s in the direction α, and E is the total energy of the system which is determined by the interatomic potential. The normal modes of a 2D system with N particles are the eigenvalues and eigenvectors of the dynamical matrix [67] $C_{st}^{\alpha\beta}(k)$ given in Eqn. 4.3.

$$C_{st}^{\alpha\beta}(k) = \frac{\partial}{\partial u_s^{\alpha}(k)} F_t^{\beta}(k) \tag{4.4}$$

In an explicit calculation of the dynamical matrix by displacing each of the atoms of the unit cell into all three directions, a periodic supercell has to be used which is commensurate with the phonon wave length 2π/k. Fourier transform of the k-dependent dynamical matrix leads to the real space force constant matrix $C_{st}^{\alpha\beta}(R)$ where R denotes a vector connecting different unit cells.

A phonon calculation starts with the determination of the dynamical matrix in real space or reciprocal space. In the force constant approaches, a reduced set of force constants $C_{st}^{\alpha\beta}(R)$ are fitted in order to reproduce experimental data. The force constants can be calculated by displacing atoms from their equilibrium position, calculating the total energy of the new configuration and obtaining the second derivative of the energy through a finite difference method. This approach is chosen

in the ab initio calculations of graphite phonons in [31, 56, 61, 63, 68]. In order to calculate the dynamical matrix for different k, a super-cell has to be chosen that is commensurate with the resulting displacement pattern of the atoms. An alternative is the use of density-functional perturbation theory (DFPT) [18,19] where the atomic displacement is taken as a perturbation potential and the resulting change in electron density and energy is calculated self-consistently through a system of Kohn Sham like equations. In both the approaches, if the dynamical matrix is calculated on a sufficiently large set of k-points, phonon's for any k can be calculated by interpolating the dynamical matrix.

4.3 Singular Value Decomposition analysis

4.3.1 Overview of SVD

Singular Value Decomposition (SVD) is a novel technique to determine all the characteristic modes of a system. In our case we generate the atomic positions using MD simulations. SVD is then done on the MD data. The details of the SVD technique are already been described in Chapter 2. In this Chapter we would give a comparison between the SVD technique and the other methods of the calculation of the modes of a system.

As stated in Section 4.2 the phonon dispersion relation calculation needs a sufficiently large set of k-points for which a large supercell has to be assumed. Phonons for any k is obtained by interpolating the dynamical matrix. In the present work we are interested in the nanomachinaery/nanodevices made up of carbon nanotube which are of finite sizes. For such systems the calculation of the mode frequencies would be different than the continuous phonon branches. Rather we are more interested in the response of such systems on the application of some external excitation, for example radial stretching given to all its atoms or an excursion given in the axial direction etc. For studying such excitations SVD seems to be a more useful technique because of the following three advantages:

- Firstly, it can, resolve the modes of a system in order of the hierarchy, including the associated frequencies as well as spatial distortions.
- Secondly, it can handle small as well as large-amplitude perturbations given to the system to excite these modes, i.e., it can identify anharmonic behavior

as well.

- Thirdly, while the present study covers only SWNTs and DWNTs, it can readily be extended to more complex structures.

4.3.2 Comparison between SVD and other methods

This subsection gives a brief comparison between the SVD technique and other methods of calculating modes of an SWNT. As discussed in Section 4.2, phonon modes are the most commonly used representation of the characteristic modes of a system. These modes correspond to the vibrational behavior of the system.

Normal mode analysis yields the complete list of vibrational modes of a CNT, giving their frequencies and the corresponding distortions (eigenvectors). The technique of normal mode analysis has also been applied successfully for the investigation of the dynamical properties of finite dust clusters in [69–71].

Normal mode analysis, in its standard form, has a major limitation i.e it yields the normal modes only in the limit of very small perturbations about the equilibrium state of the CNT based systems. In nanomotors, which is our area of interest, there can be fairly large distortions in the shape of the CNT-based system, as described in Chapter 3. This could produce two kinds of changes in the characteristic modes of the system. Firstly, the frequency of a given mode may change. Secondly, new frequencies and eigenvectors (distortions) could be generated by the interactions of modes, or by the generation of harmonics.

Therefore the characteristic modes under these conditions can be determined by a two-step process. Firstly, MD simulations are performed for the system, using an accurate interatomic potential. Secondly, the time-series data of atomic coordinates so generated is analyzed using the Singular Value Decomposition technique. This method also resolves the characteristic modes of a system in order of their relative amplitudes in that particular problem, including the effects of finite-amplitude excitation, boundary conditions, etc. This is particularly important for understanding nanodevice behavior.

Thus SVD gives the characteristic modes of the system for either small (linear) or large (nonlinear) perturbations. Strictly speaking, we cannot always call the SVD modes as 'normal modes'. However, in the limit of very small perturbations, it is expected that the two methods would yield similar results. This kind of data analysis

has been used, in the past, for studying instability-driven non-equilibrium melting dynamics of finite two-dimensional dust clusters [72]. The dynamic properties of the system have been described by both normal mode and SVD mode analysis. Using SVD, it was found that the driving modes were unambiguously related to the unstable oscillations, which were not accessible by normal mode analysis.

4.4 Computational technique

In this section we describe our MD simulations and the various parameters used. SWNT's in zig-zag and arm-chair configurations (5,0), (10,0), (15,0), (5,5), (10,10) and (15,15) are used. The structures are first relaxed with NPT simulations at a constant temperature of 300 K and pressure 0 atm. Berendsen's temperature and pressure controls [44] are used to give a desired velocity distribution and positions to the atoms. The parameters are so chosen that the velocity distribution is close to desired Maxwellian as explained in Chapter 2.

4.4.1 Choice of time step

MD time step of 0.2 fs is used in these simulations which is chosen on the basis of the largest frequency present in the system. For that we obtain the power spectral density (PSD) from the **X** coordinate of one of the atoms of the CNT as seen in Fig. 4.1.

The PSD shows that the power reduces by 10^{10} times at a frequency of 5×10^3 cm^{-1} and stabilizes after that. We take 10 times of this frequency as the Nyquist frequency so that we don't miss any other higher frequencies present in the system which gives us a time step of 0.3 fs. It means a time step of less than 0.3 fs should give us a good energy conservation in the simulations. So we do energy conservation checks with NVE runs for 2 time steps of 1 fs and 0.2 fs. We monitor the temporal variation of total energy for these two time steps. A monotonic variation in total energy is observed for the case with a time step of 1 fs while the total energy is fairly conserved in the case of 0.2 fs time step. These energy conservation checks are explained in appendix B.

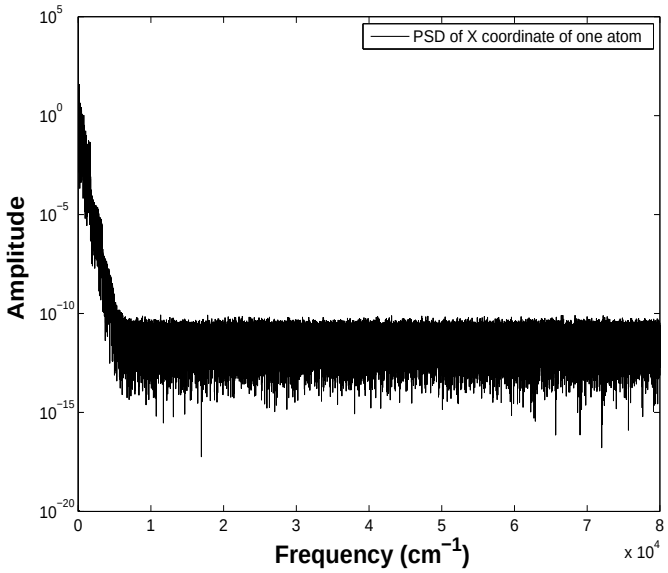

Figure 4.1: Power spectral density of **X** coordinate of one atom. The highest significant frequency is used to fix the time step for MD simulations. For frequencies higher than 5×10^3 cm^{-1}, the power spectrum resembles numerical noise.

4.4.2 Periodic boundary conditions used

Periodic boundary conditions (PBC) are used along the axial direction of the SWNT i.e **Z** axis using the minimum image convention method. Radius of each CNT is calculated as the mean radius measured from the instantaneous centroid of that CNT obtained from the relaxed coordinates. (5,5) and (10,10) configurations are observed to have a diameter of 6.97 and 13.85 Å respectively. These diameters are calculated as $2R_c$, where R_c is the instantaneous average radius obtained from the NPT relaxation data. These diameters are fairly close to those reported in [60].

4.4.3 Types of physical conditions examined

An isolated CNT in a vacuum behaves like a micro-canonical system. This means that it requires NVE simulations, since no energy can flow in or out of the system. A realistic single CNT, on the other hand, would be exposed to a constant pressure and temperature due to interactions with its surroundings. This requires NPT simulations. It is possible that these two conditions could yield a different hierarchy of SVD modes. In the present study, therefore, we have performed NVE simulations for all the six configurations of SWNT described in Section 4.4. For illustration we

repeat these simulations for one of the SWNT configurations under NPT conditions. The significant modes are extracted using SVD. In all the cases, simulations have been performed starting with the structures obtained through NPT relaxation, as described in Section 4.4.

4.5 Modes of an SWNT under NVE conditions

In this section we describe the method used to excite these modes in a SWNT for two different perturbations given to the system and report the various mode frequencies and mode structures observed for a set of zig-zag and arm-chair nanotubes. We broadly observe two classes of modes. Let m_θ and m_z refer to mode numbers in the θ and z-directions. The first class of modes observed here is characterized by $m_z = 0$, i.e., axial uniformity and the other with $m_\theta = 0$, are with radial uniformity. In the next section we discuss the method used to excite RBM and the RBM frequencies obtained in case of different SWNTs as this is the most commonly observed mode in the literature. Modes other than RBM will be discussed in a different section.

4.5.1 Radial breathing Mode (RBM), m_θ=0, m_z=0

RBM (m_θ=0, m_z=0), the most commonly observed mode in a SWNT involves a uniform (in-phase) expansion and contraction of the entire CNT. In the literature, it is commonly reported as A_{1g} mode. The frequency of this mode is known to vary as in Eqn.4.1.

To excite RBM in an SWNT, we stretch the atomic positions of all the carbon atoms, obtained from NPT relaxation runs, by 5% and 1% in two different cases and then run an NVE simulation for 1 ns. We ensure that the atom velocities are set to zero before starting the simulations. Here we discuss the results obtained for 5% initial radial stretching. Results of the 1% stretching case will be discussed in a separate section. A typical set of **S** values, as yielded by SVD, is shown in Fig. 4.2 for a (5,0) SWNT.

The use of periodic boundary conditions permits MD simulations with 200 atoms, which yields a maximum of 600 modes from SVD. For this case, and for other configurations studied, only the first few modes have significant amplitudes. Hence, in the rest of this work, we limit our analysis to the ten most significant modes.

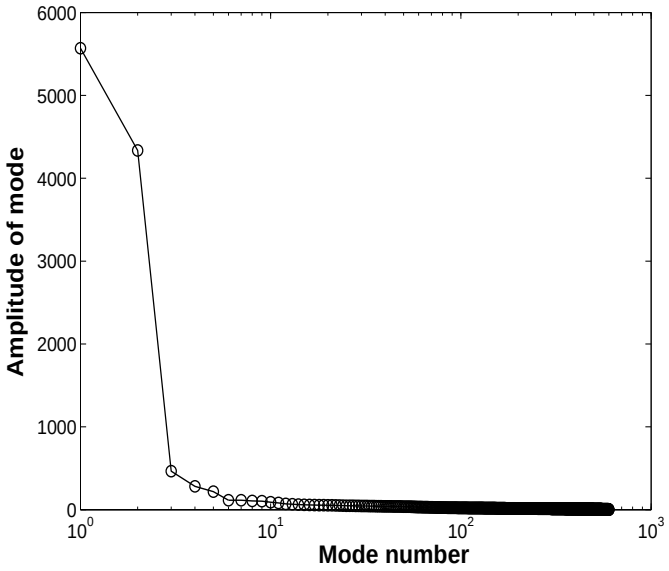

Figure 4.2: Values of amplitude S for all 600 SVD modes obtained using SVD analysis of MD data for a (5,0) SWNT. The SWNT is perturbed by an initial radial stretch of 5%. Only the first few modes have significant amplitudes.

The RBM peak is observed in two modes, numbers 1 and 2. The power spectral density for mode 1 is shown in Fig. 4.3 for a (5,0) CNT. A clear peak can be seen at 492 cm^{-1}, corresponding to RBM. Along with the RBM peak, a very low frequency peak below 1 cm^{-1} is also observed in both the cases – this is examined in detail later in this work. The spatial structure corresponding to the displacement due to the usual in-phase movement of all the carbon atoms of the nanotube in the **X-Y** and **X-Z** planes, for mode number 1, can be seen in Fig. 4.4 and Fig. 4.5 respectively. The distortions are shown for two different configurations.

From the **V** vector yielded by SVD, we obtain the distorted positions of all the carbon atoms in each case as explained in subsection 2.2.2 of Chapter 2. The percentage change in the average radii of all 20 rings of a (5,0) SWNT, due to the motion produced by mode number 1, are plotted in Fig. 4.6. A variation of nearly 12% is observed in the radii, with negligible variation along the length, clearly indicating RBM. For mode number 2, a variation of $\sim$3.5% is observed for all rings, as shown in Fig. 4.7. The analysis is then repeated for (10,0), (10,10), (15,0) and (15,15) set of carbon nanotubes. The observed frequencies are listed in Table 4.1 and are compared with the available experimental/theoretical values for the available

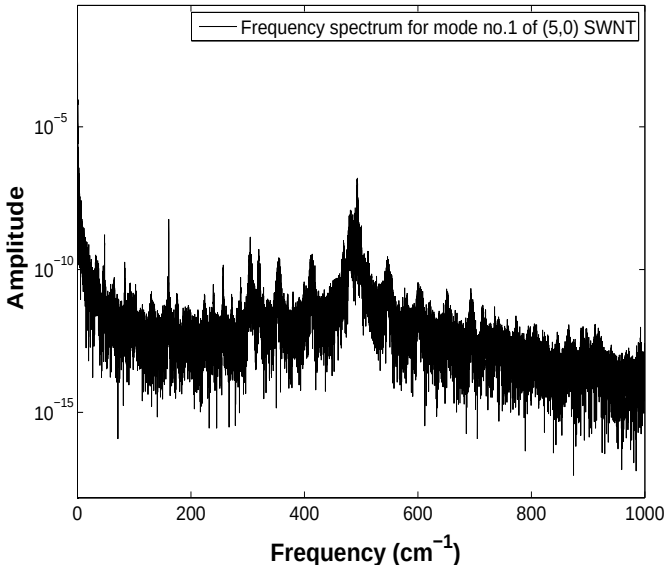

Figure 4.3: Frequency spectrum corresponding to mode number 1 for a (5,0) SWNT, showing a clear peak at 492 cm^{-1}, corresponding to RBM. A very slow frequency component is also seen in addition to RBM.

cases.

As discussed in subsection 4.4.2, the relaxed CNT diameters changes by a factor of two between (5,5) and (10,10), and the general frequency relation says that the RBM frequency should also change by a factor of two. This is indeed observed in our simulations, for the RBM frequencies. Hence the RBM mode frequency observed here satisfies the empirical formula:

$$\omega_{RBM} = A/d, \tag{4.5}$$

where d is the diameter of the nanotube and A is an empirical constant : determined experimentally [56].

4.5.2 Modes other than RBM with finite m_θ, m_z

After explaining the first 2 modes we now explain the next eight modes in descending order of their amplitude. These modes are identified in terms of the spatial distortions that they produce, such as distortions in average ring radius, average centroid shift and rotation angle θ of a ring of carbon atoms etc. As explained in the introduction of this chapter, these modes are significant from the point of view of application of SWNTs for resonantly-driven nanodevices for which the frequency

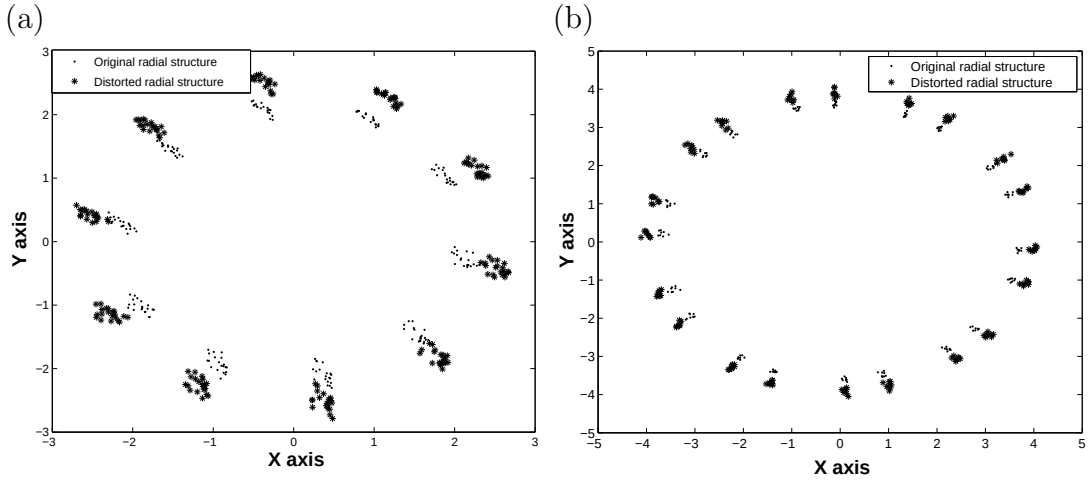

Figure 4.4: The spatial structure corresponding to the usual inphase movement of all carbon atoms of the SWNT in the **X-Y** plane, due to RBM. (a) (5,0) SWNT (b) (5,5) SWNT. The Z plane lies along the axis of the SWNT.

of the particular mode of interest should be known.

As stated earlier we broadly observe two classes of modes. The first class is characterized by $m_z = 0$, i.e., axial uniformity. Within this class, $m_\theta = 0$ is the RBM, also called A_{1g}, while $m_\theta = 2$, also called E_{1g}, are both well explained in the literature[9]. We also observe a mode with $m_\theta = 3$. The spatial distortions corresponding to RBM have already been discussed in subsection 4.5.1. The distortions associated with the other $m_z = 0$ modes, for a (10,0) SWNT, are shown in Fig. 4.8. The distorted positions of all atoms have been generated using Eqn. 2.22. However, instead of computing the time-varying 'Scale' using Eqn. 2.23, a single value of 'Scale' has been suitably chosen for clarity. It should be noted that the z-direction is the one along the original axis of the SWNT and the x-y plane shown in the figure contains the plane of each ring. From Fig. 4.8, we see an azimuthal variation in the radial positions of atoms, with some azimuthal mode number.

The second class of modes has $m_\theta = 0$ (azimuthally uniform), with $m_z = 1$ and 2. The typical spatial structures corresponding to these modes for a (5,0) SWNT are shown in Fig. 4.9. These modes involve shifts in the X- and Y-centroid locations of different rings. We now consider these modes in more detail for a (5,0) SWNT. Table 4.2 shows that modes number 3, 4, 5 and 7 have $m_\theta = 0$ and $m_z = 1$, and produce changes in the X and Y centroid locations of each ring in the SWNT, as

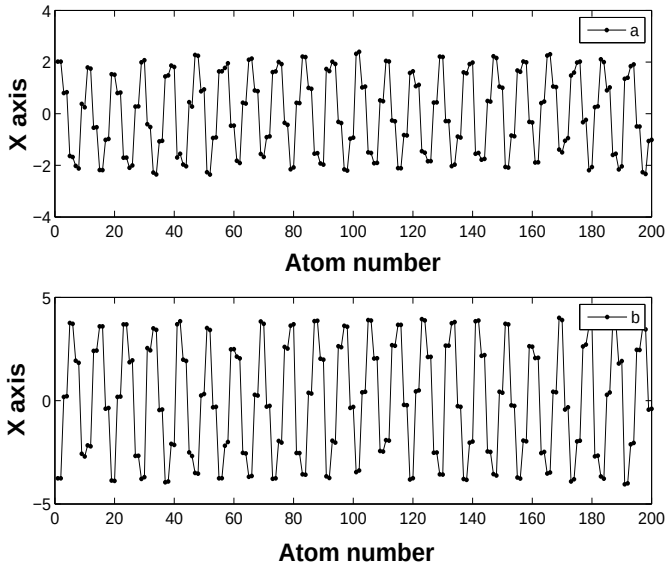

Figure 4.5: The spatial displacement of atoms corresponding to the in-phase movement of all the carbon atoms of a (5,0) SWNT due to RBM in the **X-Z** plane is shown. Curves a and b correspond to the unperturbed and the perturbed locations of the atoms respectively. The atom numbers show the Z plane along the axis of the SWNT. Note that an arbitrary scale factor is used here to get these distortions.

shown in Fig. 4.10.

We note that the amplitude of displacement in the X-centroid location is highest for mode number 3 and lowest for mode 4, and there is an axial phase shift in the amplitude. Mode 7 has higher X centroid displacements than modes 3,4 and 5, and there is negligible displacement in the Y-centroid location. The changes in quantities like average radii of different rings, and azimuthal rotation θ, are negligible for these modes. Modes number 6, 8, 9 and 10, all having $m_\theta = 0$ and $m_z = 2$, also involve changes in the X and Y centroid locations, as shown in Fig. 4.11.

The distortions in centroid locations due to the above modes mean that, at any given time, different rings in the SWNT have different centroids.

4.6 Very low frequency rotational mode

As stated in subsection 4.5.1, the RBM modes extracted through SVD, viz., modes number 1 and 2 in the amplitude hierarchy, also exhibit a very low frequency com-

$SWNT$	D	$RBM(SVD)$	$RBM(Scaling)$	$Experimental/Theoretical$
$(5,0)$	4.152	492	492	
$(10,0)$	8.056	250	246	
$(15,0)$	12.048	166	123	
$(5,5)$	6.978	295	295	$264^{[60]}$
$(10,10)$	13.850	146	147	$182^{[60]}$, $165^{[61]}$
$(15,15)$	20.768	80	73	

Table 4.1: Columns in the table show SWNT configuration, 'D' diameter obtained from NPT relaxation in Å, RBM frequency obtained from SVD in NVE simulations, RBM frequency expected from scaling law and RBM frequencies obtained by other workers. All the frequencies are in cm^{-1}. Note that the reference numbers of the other workers in the available cases, are mentioned in square brackets along with the frequencies.

	$(5,0)$	S	$(10,0)$	S	$(15,0)$	S
N	$Freq.$	(m_θ, m_Z)	$Freq.$	(m_θ, m_Z)	$Freq.$	(m_θ, m_Z)
1	492, 0.04	(0,0)	250, 0.04	(0,0)	166, 0.04	(0,0)
2	492, 0.04	(0, 0)	250, 0.04	(0,0)	166, 0.04	(0,0)
3	24	(0,1)	38	(2,0)	17	(2,0)
4	24	(0,1)	38	(2,0)	17	(2,0)
5	24	(0,1)	103	(3,0)	46	(3,0)
6	80	(0,2)	103	(3,0)	46	(3,0)
7	24	(0,1)	99	(1,0)	88	(4,0)
8	80	(0,2)	99	(1.0)	88	(4,0)
9	80	(0,2)	99	(1,0)	95	(0,1)
10	80	(0,2)	99	(1,0)	95	(0,1)

Table 4.2: Columns in the table show mode sequence number 'N' in order of decreasing amplitude, mode frequency and the mode structure **S** for different configuration of zig-zag SWNTs in NVE simulations. All the frequencies are in cm^{-1}. Mode structure is obtained as explained in subsection 2.2.2 of Chapter 2.

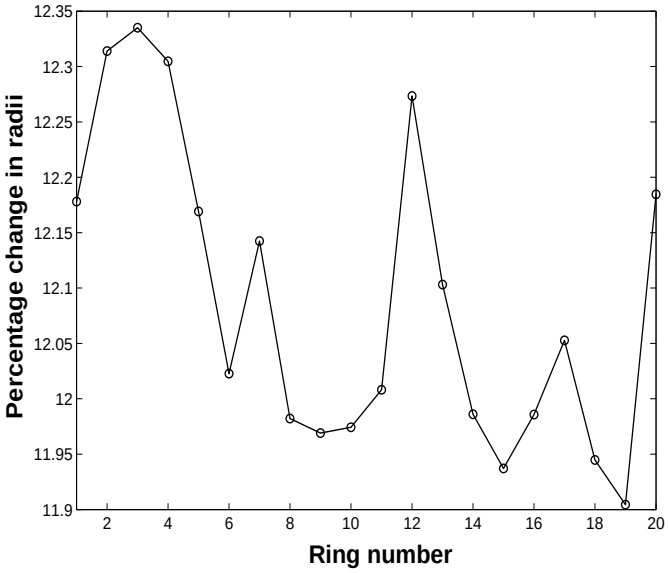

Figure 4.6: Percentage change in average radii of rings due to distortion produced by mode number 1, in a (5,0) SWNT. The radii are measured with respect to the respective centroid of the individual rings.

ponent. Analysis of the accompanying distortion shows that this corresponds to a very slow rotation of the SWNT rings about their respective centroids. This rotation is different from simple rigid body rotation of the entire SWNT which would raise a question about angular momentum conservation. The rings rotate about their own centroids which is different for different rings because of the various m_z modes involving movement of the centroids as discussed in Section 4.5.2. The total angular momentum of the system is conserved as discussed below.

4.6.1 Angular Momentum conservation

Since the MD simulation is started with zero atom velocities, it implies zero initial angular momentum of the SWNT about any specified axis. Conservation then demands that the angular momentum about that axis should always stay equal to zero. This can indeed be seen from Fig. 4.12, which shows the total angular momentum of the SWNT about the axis x=y=0 as a function of time. This angular momentum is negligible in comparison to the angular momentum of the individual rings as shown in Fig. 4.13. A significant angular momentum of the individual rings implies a net θ motion of the rings about their own centroid. As seen in Fig. 4.13 an individual ring acquires an angular momentum of nearly 2x10^{-32} Kgm^2/sec about the Z axis,

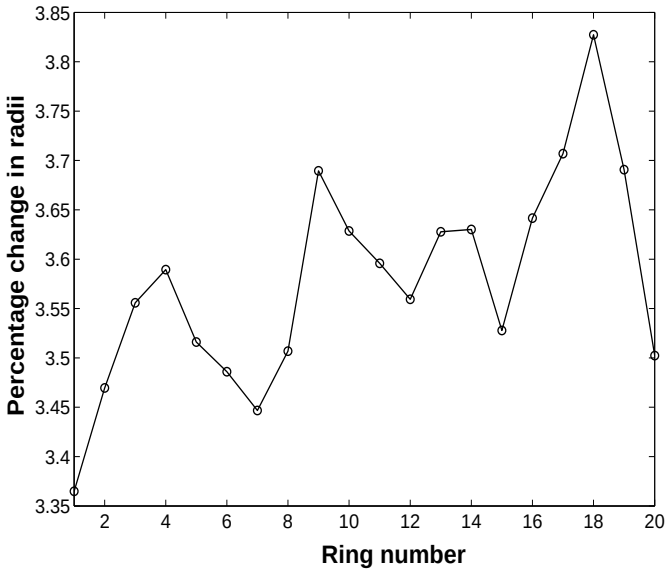

Figure 4.7: Percentage change in average radii of rings due to distortion produced by mode number 2 in a (5,0) SWNT. The radii are measured with respect to the respective centroid of the individual rings.

which is along the length of the SWNT. As seen in Fig. 4.14 the angular momentum of ring number 1 and 2 cancels out each other at times. Note that these two rings are chosen for illustration here though its the sum of the angular momentum of all the rings which makes the total angular momentum of the SWNT negligible. Thus total rotation that appears in modes 1 and 2 is actually the individual rotation of each ring about its instantaneous axis, this axis being different for different rings.

4.6.2 θ rotation of individual rings

Fig. 4.15 shows the temporal evolution of the azimuthal location θ of atom number 1 of ring 1, due to motion connected with modes 1 and 2. Here, $\theta(t)$ has been computed using Eqn. 2.22 and 2.23.

Similar rotational motion is observed for other atoms on the same ring, and on other rings. We also calculate the azimuthal rotation angle θ produced in atom number 1 of ring 1 due to all the 600 modes and find that the main contribution to this rotation comes from modes number 1 and 2.

Fig. 4.15 shows that the period of rotational motion is of the order of the complete MD simulation time $\sim$0.8 nanosecond, corresponding to $\sim$0.04 cm^{-1}. Since the frequency resolution of the SVD analysis is determined by the total simulation time,

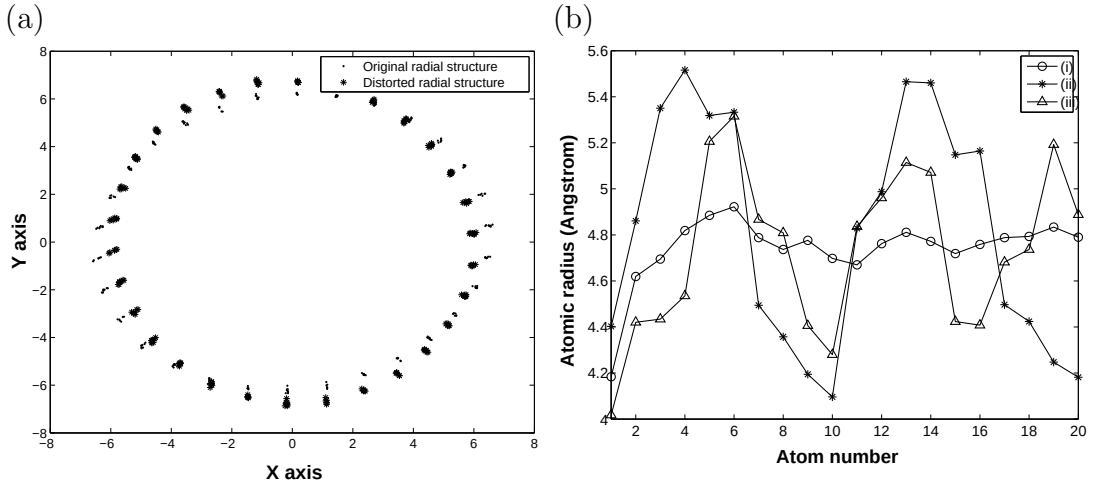

Figure 4.8: Modes with $m_z = 0$ and finite m_θ in a (10,0) SWNT. (a) Atomic displacements in the X-Y plane corresponding to (m_θ = 2,m_z = 0) (E_{1g}) mode. Variation of radial position of atoms with the azimuthal angle is clearly visible with a mode number 2. (b) Variation in atomic radii, measured with respect to the centroid of the respective ring. Curve (i) shows the radii in the unperturbed configuration. Curves (ii) and (iii) show the radii due to variations produced by modes (m_θ = 2, m_z = 0) and (m_θ = 3, m_z = 0) respectively. Increasing 'atom number' from 1 to 20 corresponds to azimuthal angle varying from 0 to 2π.

the low-frequency peak appears at the second frequency point, corresponding to 1.2 GHz or 0.04 cm^{-1}. The exact frequency could be slightly lower or higher than this value, but cannot be resolved.

One important point to be considered here is as to why this low frequency rotational mode appears with RBM. One possible reason could be that these are the only two observed modes for which the displacement produced in the atomic coordinates of all the atoms are same. On the other hand in all other modes the atomic coordinates of different atoms get perturbed by different amount as seen in Fig. 4.8 and Fig. 4.9.

4.7 Finite m_θ, m_z modes that are significant in other configurations

Frequencies of some other modes with significant amplitudes, for all six configurations of the SWNT mentioned in Section 4.4, are listed in Tables 4.2 and 4.3. Here we discuss some of these modes that are not observed in the case of a (5,0) SWNT.

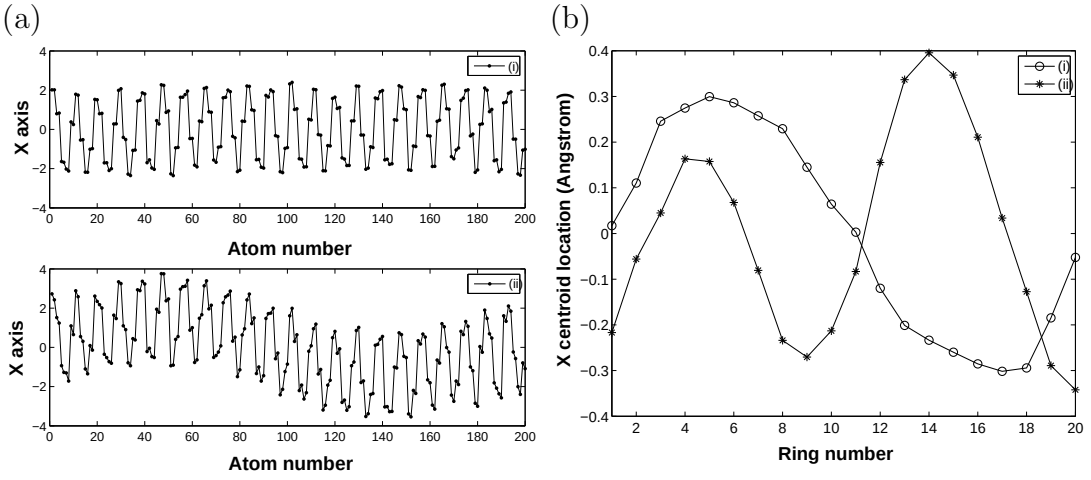

Figure 4.9: Modes with $m_\theta = 0$ in a (5,0) SWNT (a) Atomic displacements in the X-Z plane produced by $m_\theta = 0$, $m_z = 1$. Curves (i) and (ii) show the atomic locations of the atoms in the unperturbed and the perturbed configurations respectively. An arbitrary scale factor is used here to get these distortions. (b) Curves (i) and (ii) show the shifts produced in the X centroid locations of different rings, due to ($m_\theta = 0$, $m_z = 1$) and ($m_\theta = 0$, $m_z = 2$) modes respectively. Although only the X-centroid displacements are shown, these modes involve both X- and Y-shifts.

- (m_θ = 2,m_z = 0) (E_{1g}) is seen as mode number 3 for (10,0) and (10,10) SWNT's with a frequency at 38 and 12 cm^{-1} respectively. This mode is well understood in the literature of SWNT modes [57] with the spatial structure as shown in Fig. 4.8(a).

- (m_θ = 3,m_z = 0) mode is also observed in many cases. It has a frequency higher than that of the (m_θ = 2,m_z = 0) mode.

- In the case of (15,0) and (15,15) SWNTs, (m_θ = 4,m_z = 0) mode is also observed with frequency higher than that of (m_θ = 3,m_z = 0) mode.

- The frequency of quasi-rigid body rotation is slightly higher in case of a (15,15) SWNT, $\sim$ 0.08 cm^{-1}, while in all other cases it is 0.04 cm^{-1}.

These modes are significant from the point of view of application of these nanotubes for practical applications where knowledge of the frequencies of various modes can be used for resonantly exciting them.

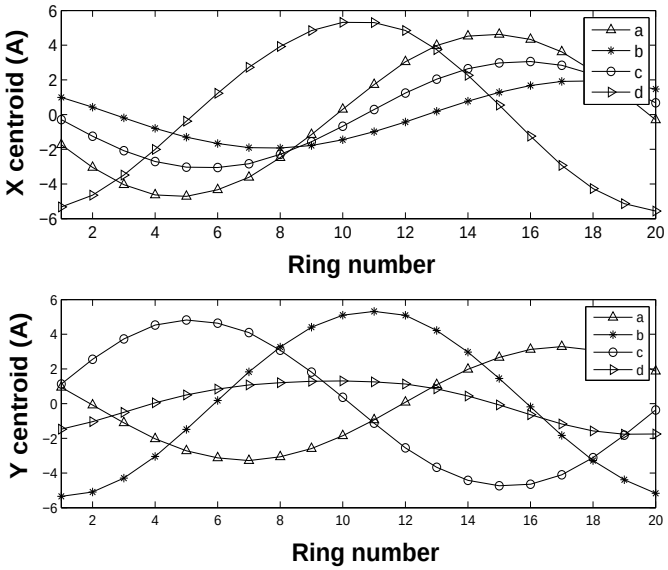

Figure 4.10: Shift in X and Y centroid locations (Å) of different rings in ($m_\theta = 0$,$m_Z = 1$) mode for (5,0) SWNT calculated from the unperturbed and the perturbed coordinates of the carbon atoms. Here curves a, b, c and d correspond to the distortions produced due to mode numbers 3, 4, 5 and 7 respectively.

4.8 Modes of (5,0) SWNT obtained for 1% radial stretching

The results of Section 4.5 were obtained after applying a 5% radial stretch in all atomic locations, as compared to the NPT-equilibrated locations. We repeat the simulations with only a 1% initial radial stretching given to the atoms as to see the effect of anharmonicity on the amplitude of the modes. The mode amplitudes for this case are shown in Fig. 4.16 for a (5,0) SWNT. Recall that in the 5% case, modes 1 and 2 had almost similar amplitudes, followed by significantly smaller amplitudes for the other modes. In the 1% case, mode 1 is observed to be clearly dominant and stands alone. As seen in Fig. 4.17 the RBM peak is clearly visible in the frequency spectrum and the relative strength of the RBM peak, in the relation to the low-frequency peak, has increased significantly. The RBM frequency has also come up to 495 cm^{-1} in comparison to 492 cm^{-1} in the NVE case. The hierarchy of other modes remains the same as in the 5% case. The second RBM mode has disappeared, as expected. The total range of rotational motion of atom 1 of ring 1 is 20 degrees, as compared to 90 degrees in the 5% perturbation case. Hence it appears that

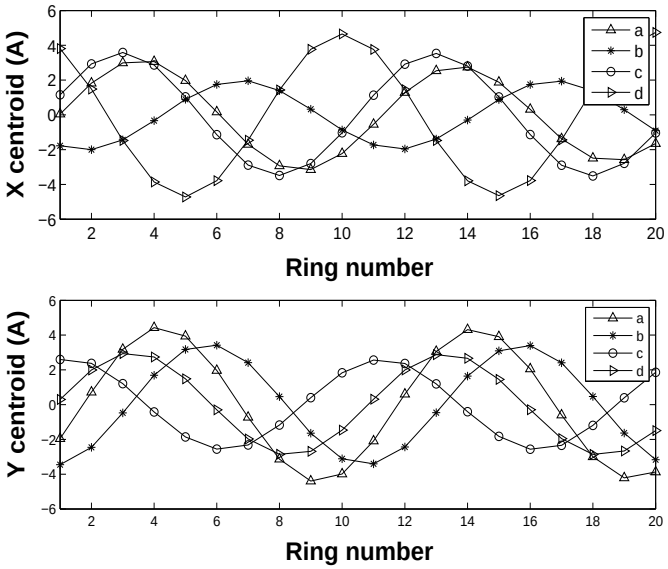

Figure 4.11: Shift in X and Y centroid locations (Å) of different rings in ($m_\theta = 0$,$m_Z = 2$) mode for (5,0) SWNT calculated from the unperturbed and the perturbed coordinates of the carbon atoms. Here curves a, b, c and d correspond to distortions produced due to the mode numbers 6, 8, 9 and 10 respectively.

low-amplitude perturbations leads to weaker coupling between modes.

4.9 Modes of an SWNT under NPT conditions

We have so far studied the SVD modes of an SWNT under NVE conditions. This is acceptable for an isolated SWNT. In real-life systems, however, the SWNT would be in contact with the surroundings, which would tend to maintain a constant temperature and pressure. Hence, for purposes of illustration, we repeat the same analysis for a (5,0) configuration of the SWNT under NPT conditions, with a temperature of 300 K and a pressure of 1 atm. A 5% initial radial stretch is used in this case. The results are presented in Table 4.4. The frequencies of various modes are broadly the same as those obtained in NVE simulations. However, the hierarchy of modes is shuffled in a few cases. The RBM frequency is observed to be higher in this case as compared to NVE simulations.

N	$(5,5)$ $Freq.$	S (m_θ, m_Z)	$(10,10)$ $Freq.$	S (m_θ, m_Z)	$(15,15)$ $Freq.$	S (m_θ, m_Z)
1	295, 0.04	(0,0)	146, 0.04	(0,0)	80, 0.08	(2,0)
2	295, 0.04	(0,0)	146, 0.04	(0,0)	80, 0.08	(0,0)
3	48	(2,0)	12	(2,0)	54	(2,0)
4	48	(2,0)	12	(2,0)	54	(2,0)
5	88	(0,1)	34	(3,0)	160	(4,0)
6	110	(0,1)	34	(3,0)	160	(4,0)
7	88	(0,1)	65	(4,0)	160	(4,0)
8	88	(0,1)	65	(4,0)	54	(2,0)
9	110	(0,1)	79	(0,1)	54	(2,0)
10	110	(0,1)	79	(0,1)	160	(4,0)

Table 4.3: Columns in the table show mode sequence number 'N' in order of decreasing amplitude, mode frequency and the mode structure **S** for different configuration of arm-chair SWNTs in NVE simulations. All the frequencies are in cm^{-1}. Mode structure in each case is obtained as explained in subsection 4.3 of Chapter 2.

N	$(5,0)$ $Frequency$	S (m_θ, m_Z)
1	495, 0.04	(0,0)
2	495, 0.04	(0,0)
3	24	(0,1)
4	24	(0,1)
5	80	(0,2)
6	24	(0,1)
7	24	(0,1)
8	80	(0,2)
9	24	(0,1)
10	80	(0,2)

Table 4.4: Columns in the table show mode sequence 'N' in order of decreasing amplitude, mode frequency and the mode structure **S** for (5,0) configuration of a zig-zag SWNT in an NPT simulation. All frequencies are in cm^{-1}.

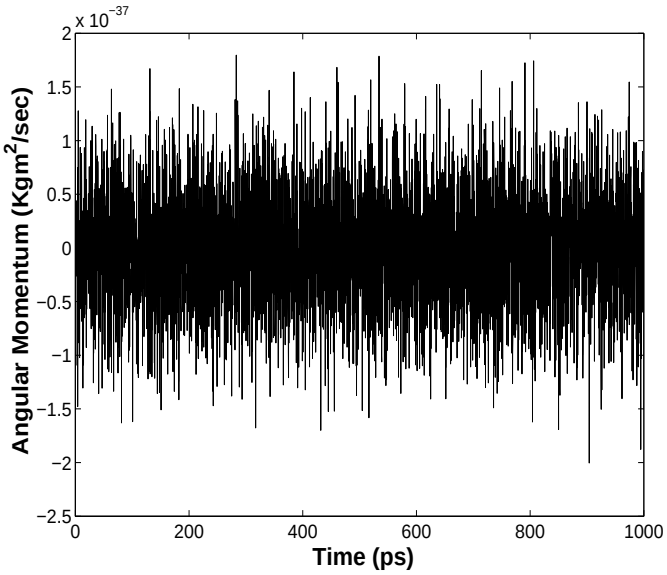

Figure 4.12: Variation of the total angular momentum, of the SWNT about the axis x=y=0 as a function of time. Shows that the SWNT exhibits a very small total angular momentum hence a negligible angular frequency.

4.10 Resonance excitation of an SWNT

Normal modes of any structure are often weakly damped, since they are distortions that are intrinsically supported by the structure. Hence it is reasonable to expect that external excitation of a characteristic mode would lead to large amplitude perturbations that are higher than those produced by non-resonant excitation. This is illustrated below.

Let us attempt to excite the mode ($m_\theta = 0$,$m_z = 1$), which involves x- and y-directed motion of the centroids of different rings. We start with a (5,0) SWNT that is relaxed at normal NPT conditions. We next assume that atom 1 of ring number 5 and atom 6 of ring 15 are given charges of +e and -e, respectively. The SWNT is then exposed to an external electric field of the form

$$\vec{E} = E_{x0} Cos(\omega t) \tag{4.6}$$

as detailed in [55]. This field produces an x-directed acceleration of these two atoms. The frequency of this externally applied electric field is chosen to be 24 cm^{-1}, which is the frequency of the ($m_\theta = 0$,$m_z = 1$) mode. These two atoms are chosen due to the spatial structure of this mode, shown in Fig. 4.10.

NPT simulations are run for 100 ps. The X and Y centroid locations of all the

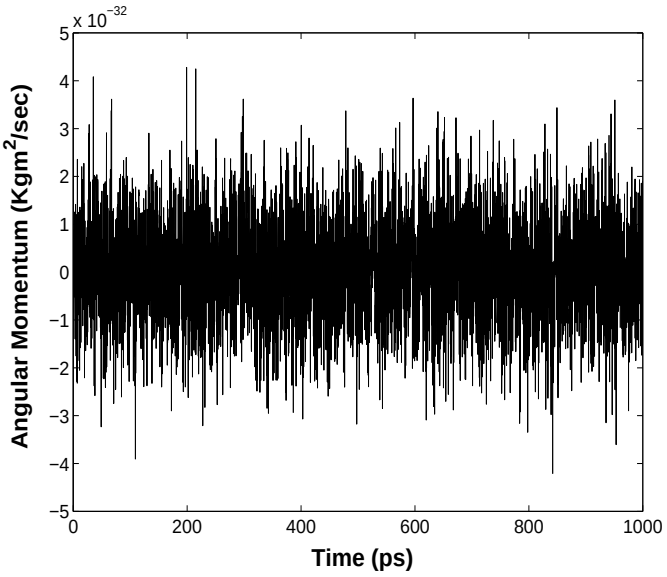

Figure 4.13: Variation of the angular momentum, of the ring number 1 of SWNT about the axis x=y=0 as a function of time. This angular momentum is significant in comparison to the total angular momentum of the SWNT implying that the individual rings are rotating about their own centroids.

atoms are monitored during the simulation. Fig. 4.18 shows the X and Y centroid locations of atom number 1 of ring number 5 to which the positive peak of the field is applied.

A continuously rising amplitude of the X centroid location can be observed. This is because of the sinusoidally applied electric field in this direction. The Y centroid location shows a different behavior which could be because of the indirect coupling of energy from the field. Fig. 4.19 shows the envelopes of the X centroid location amplitudes for different rings.

The amplitude of the envelopes is seen to be decreasing as we move away from the ring to which electric field is applied. For rings number 5 and 15, we see the amplitude rising continuously, reaching 6 Å at t = 100 ps.

Let us now consider non-resonant excitation using two different frequencies. Fig. 4.20 shows the envelopes of the X centroid location amplitudes for two different frequencies of the applied field. Also shown for reference is the case of no applied field. For an applied frequency equal to 48 cm^{-1}, twice the mode frequency, oscillations in the range of +1 and -1 Å are observed – also, the amplitude is observed to saturate, unlike the resonant case. For an arbitrary applied frequency = 56.88 cm^{-1}, smaller oscillations with 0.5 Å are observed. These oscillations are even

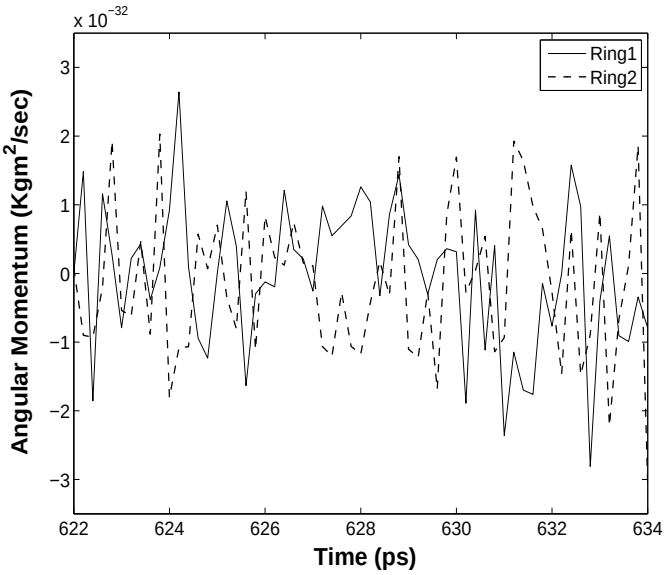

Figure 4.14: Variation of the angular momentum, of ring number 1 and 2 of SWNT about the axis x=y=0 as a function of time. This angular momentum is significant in comparison to the total angular momentum of the SWNT. Also note that at times like 624, 628 and 632 ps the angular momentum of the two rings seems to be canceling out each other. Note that its the sum of the angular momentum of all the rings which makes the net angular momentum of the system zero.

smaller in the case of no external field applied to the system.

This means that the excitations produced at a frequency other than the characteristic mode frequency does not produce any significant resonance in the SWNT. These studies involving the resonance excitations of the SWNT are important from the point of view of application of these SWNTs as nano-devices.

4.11 Mode analysis of a (5,0)@(15,0) DWNT under NPT conditions

Similar to the characteristic mode analysis done for an SWNT, we repeat this analysis for a DWNT. We choose a (5,0)@(15,0) DWNT. The structure is first relaxed at room temperature and pressure. An NVE MD simulation is then performed. SVD done on the MD data gives all the characteristic modes of the structure. We study first ten modes in detail. The various characteristic modes obtained and the corresponding frequencies are as in Table 4.5. As compared to the SWNT case, we

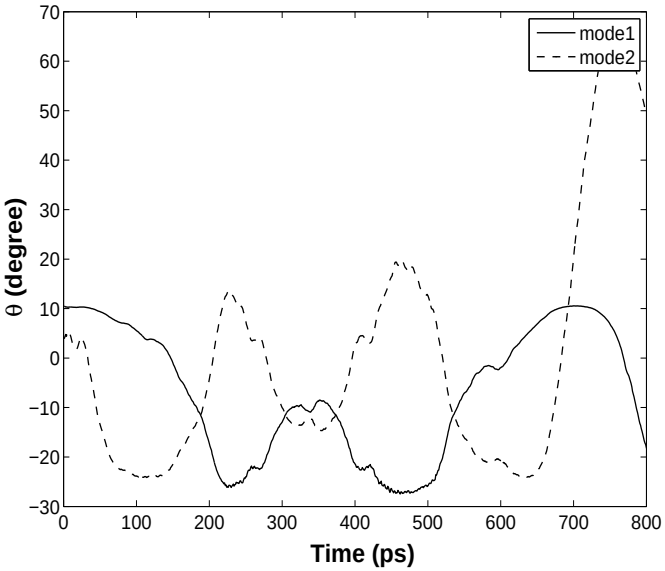

Figure 4.15: Variation of azimuthal rotation angle θ produced in atom number 1 of ring number 1, due to mode numbers 1 and 2. These slow rotations are produced due to a quasi-rigid body rotation of the rings about their respective centroids.

N	$(5,0)$ $Frequency$	S (m_θ, m_Z)
1	497, 0.04	(0,0)
2	497, 0.04	(0,0)
3	26	(0,1)
4	26	(0,1)
5	26	(0,1)
6	125	(0,2)
7	26,125	(0,2)
8	125,242	(0,2)
9	125,242	(0,2)
10	82	(0,2)

Table 4.5: Columns in the table show mode sequence 'N' in order of decreasing amplitude, mode frequency and the mode structure **S** for a (5,0)@(15,0) DWNT configuration in an NPT simulation. All frequencies are in cm^{-1}. Note that the outer carbon nanotube is held fixed in this case.

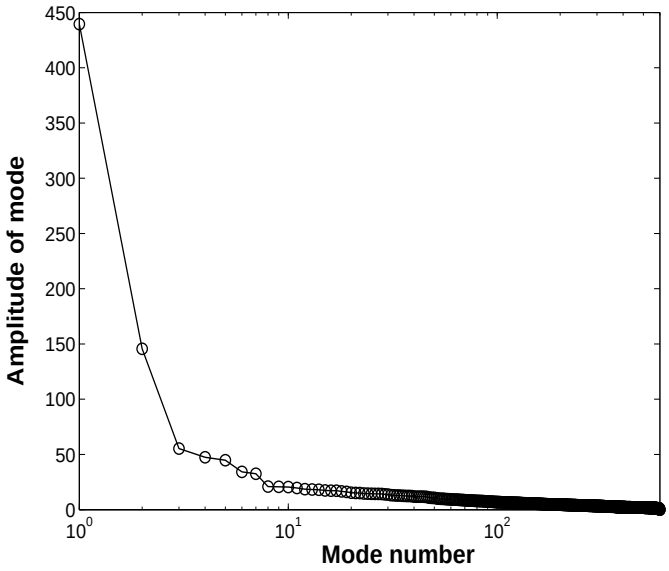

Figure 4.16: S values for all the SVD modes in a (5,0) SWNT configuration for a radial stretch of 1% given to all its atoms. Amplitude of first few modes look significant.

see the following differences in the mode frequencies obtained in this case:

- In this case we see that the RBM frequency has got shifted up to 497 $cm^{-}1$. This is because as expected, this geometry produces a higher restoring force, hence it leads to an upshift in the RBM frequency.
- Also the frequency of some axial modes like (m_θ, m_z) = (0,1) and (0,2), are slightly different from the SWNT case.
- For some other mode numbers (same m_θ & m_z), where an SWNT exhibited a single frequency, a DWNT exhibits more than one peak in the power spectral density. This is possibly due to coupling between different modes due to interaction with the outer CNT.

4.12 Conclusions

We have shown, for the first time, that the complete set of characteristic modes of a single-walled nanotube can be extracted using SVD analysis on molecular dynamics results. For the well-known case of radial breathing modes, this analysis gives good agreement between the calculated mode frequency and published experimental measurements, as also the 1/D scaling of RBM frequency.

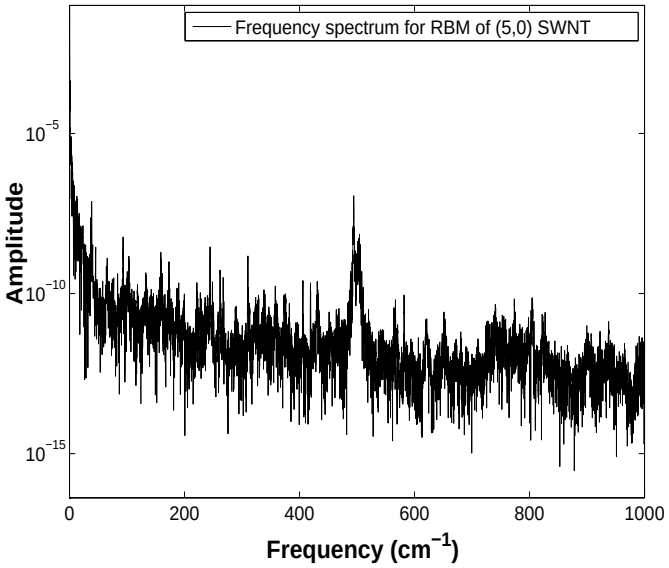

Figure 4.17: Frequency spectrum corresponding to mode number 1 of a (5,0) SWNT showing a clear peak at 495 cm^{-1} for RBM. Note that the amplitude of the RBM peak is more sharp in this case as compared to the 5% radial stretching case.

The first part of the study focuses on an SWNT under NVE conditions, i.e., an isolated SWNT. For the case with 5% initial radial stretching in the SWNT, radial breathing motion is seen in the two strongest modes. The distortion associated with each of these modes is a combination of radial breathing with a very slow rotational motion of individual rings of the SWNT, although the SWNT as a whole has a zero rigid-body rotational motion. This coupling between these two modes weakens when the radial stretching is reduced to 1%. These conclusions apply to all six configurations examined in this work. Apart from these mixed RBM-rotational modes, the next eight most significant modes can be broadly divided into two classes. The first class is characterized by $m_z = 0$, i.e., axial uniformity. These modes produce an azimuthal variation in the radial positions of atoms, with some azimuthal mode number. The second class of modes has $m_\theta = 0$ (azimuthally uniform), with $m_z = 1$ and 2. These modes involve shifts in the X- and Y-centroid locations of different rings, i.e., transverse to the nominal axis of the SWNT. Some modes arise only in the case of configurations other than (5,0), such as $m_z = 0$ with $m_\theta = 2,3,4$ and $m_z = 3$ with $m_\theta = 0$.

The analysis has been repeated for a (5,0) configuration of SWNT under NPT conditions, maintaining a temperature and pressure of 300 K and 1 atm, which mimic

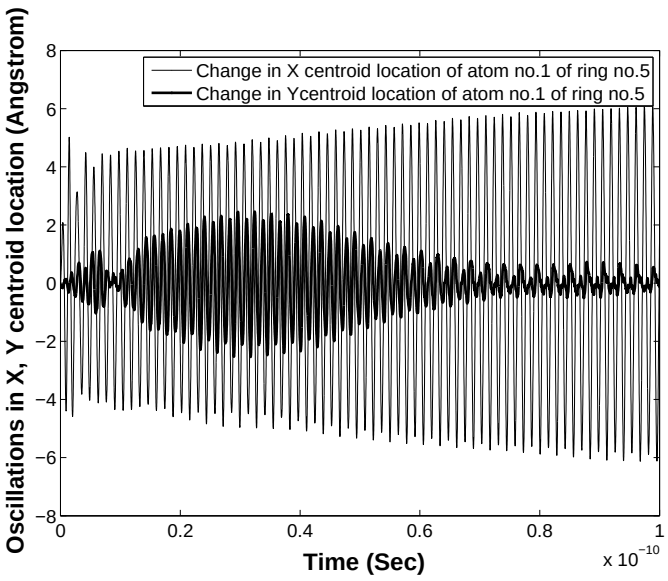

Figure 4.18: Temporal variation of the amplitudes of the X and Y centroid locations produced in atom number 1 of ring number 5 of a (5,0) SWNT, produced from the resonance excitation at one of its characteristic mode frequency, 24 cm^{-1}.

laboratory conditions. The frequencies of the modes are almost similar to those obtained under NVE conditions, but the hierarchy of modes is slightly different. The RBM frequency observed in this case is slightly higher as compared to that observed in NVE simulations.

The knowledge of the characteristic modes thus obtained is then used to study the difference between resonant and non-resonant excitation of an SWNT. Excitation produced at one of the characteristic mode frequencies, corresponding to centroid motion ($m_\theta = 0$, $m_z = 1$), shows a significant and steady increase in the amplitude of centroid displacement. Excitation at the second harmonic of the mode frequency leads to an initial increase in displacement amplitude, but eventual saturation. Non-resonant excitation leads to saturation at a lower level than that from second harmonic excitation. These conclusions are important from the point of view of application of SWNTs as nano-devices, e.g. as nanomotors.

The characteristic mode analysis has been repeated for a DWNT. We see that majority of the modes are the same but the mode frequencies are slightly different. The frequency of the RBM mode is observed to be higher in this case. Also the frequency of few other modes is different than the SWNT case. Multiple peaks are also seen for some of the modes at more than one frequency point. This variation is

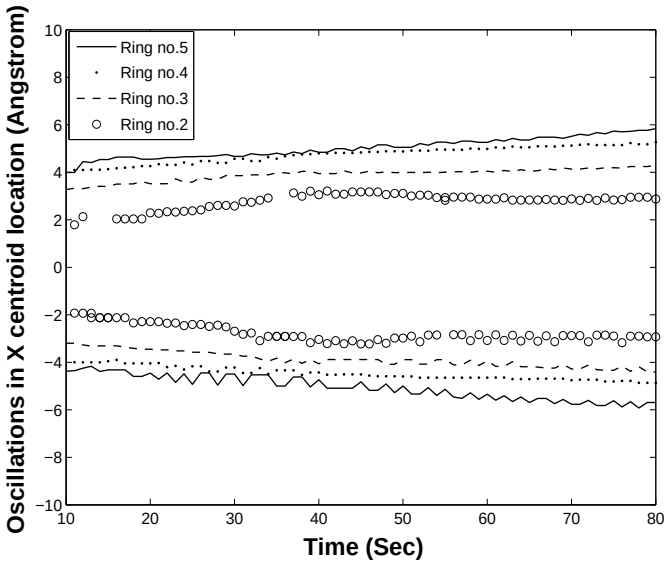

Figure 4.19: Envelopes of the amplitudes of the X centroid location of atom number 1 of different rings for resonance excitation produced in a (5,0) SWNT at one of its characteristic mode frequency, 24 cm^{-1}. Note that the amplitude of the perturbation produced in the centroid locations decreases as we move away from ring number 5 to which external field is applied.

expected because of the interaction between the inner and the outer carbon nanotube in case of a DWNT.

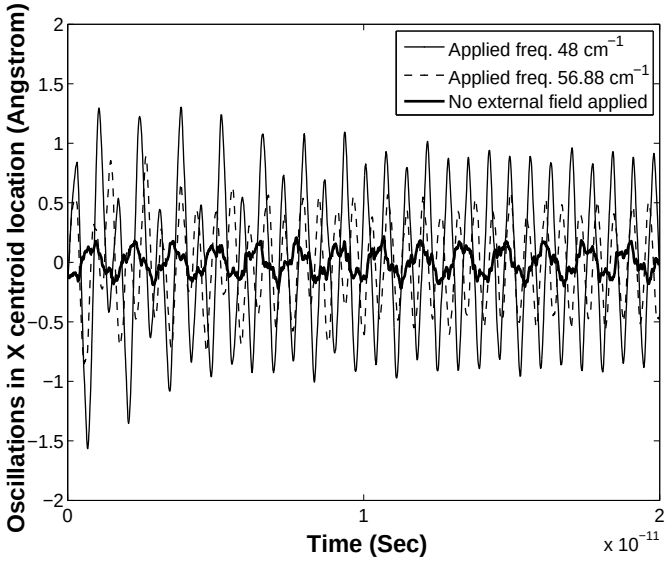

Figure 4.20: Temporal variation of the amplitudes of the X centroid location of atom number 1 of ring number 5 of a (5,0) SWNT for excitations produced at different frequencies. These frequencies are different from the mode frequencies of the SWNT.

Chapter 5

Determination of useful parameter space for a double-walled carbon nanotube motor subjected to a sinusoidally varying electric field

5.1 Introduction

In Chapter 3 we saw that for a given frequency ($\sim 2 \times 10^{10}$ Hz), it was impossible to produce full rotation of the shaft, regardless of the applied E-field amplitude [55]. This is because at low amplitudes, the torque produced by the electric force was less than the torque required to overcome the restoring torque. This restoring torque was due to the potential energy barriers in the system. A simple estimate of the minimum E-field, E_{th}, required to produce rotation in the shaft was made using the gradient of the potential energy surface in the direction of rotation. Locked states were observed in the shaft on applying a field of frequency of 2.045×10^{10} Hz and amplitude higher than E_{th} [55]. Application of higher amplitude fields led to distortion of the shaft, in turn changing the potential energy surface (PES). This led to even stronger potential energy barriers against rotation of the shaft, in turn increasing the threshold electric field beyond the actual applied value. These locked states limit the utility of these motors for the practical applications of these as nanomotors.

As discussed in Chapter 3, earlier the frequency was held constant, while a few

different electric field amplitudes were tried in an attempt to produce unidirectional motion of the shaft. In general, the electric field amplitude and frequency form a two-dimensional parameter space. Now we attempt to determine a 'useful' region in this parameter space where the shaft exhibits unidirectional (motor-like) motion.

Consider the use of a higher frequency at a given amplitude. We would expect the shaft to deform less before the E-field reverses sign. This should lead to a reduction in the potential energy barrier against rotation, making rotation possible. In the limit of very high applied frequency, however, the shaft would simply not respond to the electric-field due to its own inertia. This imposes an upper bound on the useful frequency. Therefore it seems, that there should be a useful range of E-field frequencies, where the distortion of the shaft is small, but there is still enough time to drive rotation. For a given frequency in this range, there could then be a range of E-field amplitudes which is enough to overcome the rotational barrier and yet does not cause too much distortion. Therefore now our objective is to determine if such a useful region in parameter space exists at all and to define its limits.

This chapter is organized as follows. In Section 2, we present details of the computational model. In Section 3, we present a simple rigid-body model of the nanomotor to determine a useful operating point where unidirectional motor-like motion is likely. Section 4 gives the results and discussion. A detailed explanation for an unexpected result is presented in Section 5, and Section 6 lists the conclusions.

5.2 Computational Technique

5.2.1 Setting up the MD simulations

In this section we describe our MD simulations and the various parameters used. Brenner potential [34] is used as earlier for carbon-carbon interactions within a nanotube, with Nordlund's long range interaction potential [35] for the interactions between the nanotubes. SWNTs in zig-zag configurations (5,0) and (15,0), of lengths 41.81 and 12.52 Å respectively, are used in our simulations as shaft and sleeve. The co-ordinates used and the end-on configuration of the motor are as shown in Fig. 3.1. Both the shaft and sleeve are centered about a common rotational axis

(**Z** axis). After placing the shaft inside the sleeve, the structure is equilibrated at a temperature of 300 K and 0 atmosphere pressure, using Berendsen's temperature and pressure control [44] with a time constant of 500 fs for a simulation of 100 ps.

5.2.2 Application of external electric field

After relaxation of the DWNT structure, unit positive and negative charges are assumed on the diametrically opposite first and sixth atoms of the shaft as already discussed in Chapter 3. The line joining these two atoms makes an initial angle of 20 degree with the X axis. An external electric force of the form

$$qE_a\ cos(w_E t), \tag{5.1}$$

is applied to the already existing interatomic potential force term for the two charged atoms, where ± q is unit charge assigned to atoms 1 and 6, and E_a denotes the applied electric field strength. To start with, we use a field amplitude E_a as 1.1×10^{10} V/m and frequency ω_E equal to 2.0×10^{12} rad/sec as obtained from a simple model described in the next section. A parametric study can then be performed by varying the field amplitude and the frequency over a range of values close to this point in amplitude-frequency space. The MD time step is 0.1 femto-second in our simulations and the simulations are run for 800 ps. The angular velocity for the shaft and the sleeve are calculated in the same way as explained in the subsection 3.2.4.

5.3 Nominal operating point calculation

Before exploring a full parameter space for the nanomotor using MD it is essential to obtain a nominal operating point since exploring a full parameter space with MD would be computationally very costly. This nominal operating point would require a point in the field amplitude and frequency space where unidirectional motion of the shaft could be observed. Therefore we first calculate a threshold electric field amplitude as explained below and then obtain a corresponding frequency for this field amplitude which could produce possible motor like motion in the shaft.

5.3.1 Threshold electric field E_{th}

Consider the section of the potential energy surface (PES) for the DWNT system, corresponding to rigid-body rotation of the shaft inside a static sleeve. The potential

energy barriers produced by this PES imply a large drag force that opposes rotation of the shaft inside the sleeve. As explained in Chapter 3 a high amplitude electric field is needed to rotate the shaft inside the fixed sleeve, in order to overcome this drag.

The above-mentioned section of the PES is generated as explained in Subsection 3.4.2. A plot of the PES with the starting configuration of the DWNT system before NPT thermalization is as shown in Fig. 5.1 (i). This PES gives 15 peaks, which is in agreement with Merkle's [54] formula for the periodicity of the potential energy of such a DWNT configuration. The number of peaks depend on the number of atoms in the outer and inner nanotube. However after relaxing this structure at 0 atmosphere pressure and 300 K temperature using MD, the PES becomes smooth as seen in Fig. 5.1 (ii). The reason for the smooth behavior of this PES will be explained in the next subsection.

The gradient of this PES plot along the direction of rotation θ is as shown in the Fig. 5.1 (iii). The threshold electric field E_{th} required for the rotation of the shaft inside the fixed sleeve is given in terms of this gradient as follows:

$$2qR_aE_{th} = d\phi/d\theta \tag{5.2}$$

where q is the electronic charge and R_a is the radius of the shaft. In the above expression, the direction of the electric field is assumed to be perpendicular to the line joining the two charged atoms, i.e., the orientation of maximum effectiveness in generating a torque. A threshold electric field, E_{th} of 0.28×10^{10} V/m is obtained in this case. Note that the model used above does not take into account the distortions produced in the shaft due to the application of the electric field, Secondly, since the shaft keeps rotating, the angle between the electric field and the line connecting the two charges would vary, reducing the time-averaged torque. For both these reasons, the actual field amplitude required might be significantly higher than this value.

5.3.2 Comparison with the Merkle's hypothesis

In our simulations we have a 3.74 Å spacing between the shaft and the sleeve which is close to the spacing observed in a DWNT obtained experimentally [36, 37]. During the NPT relaxation, the sleeve is held fixed and the shaft center shifts widely within the sleeve. We observe a centroid displacement of the shaft at the end of the simulation as seen in Fig.5.2. The shaft sits off-axially inside the fixed sleeve

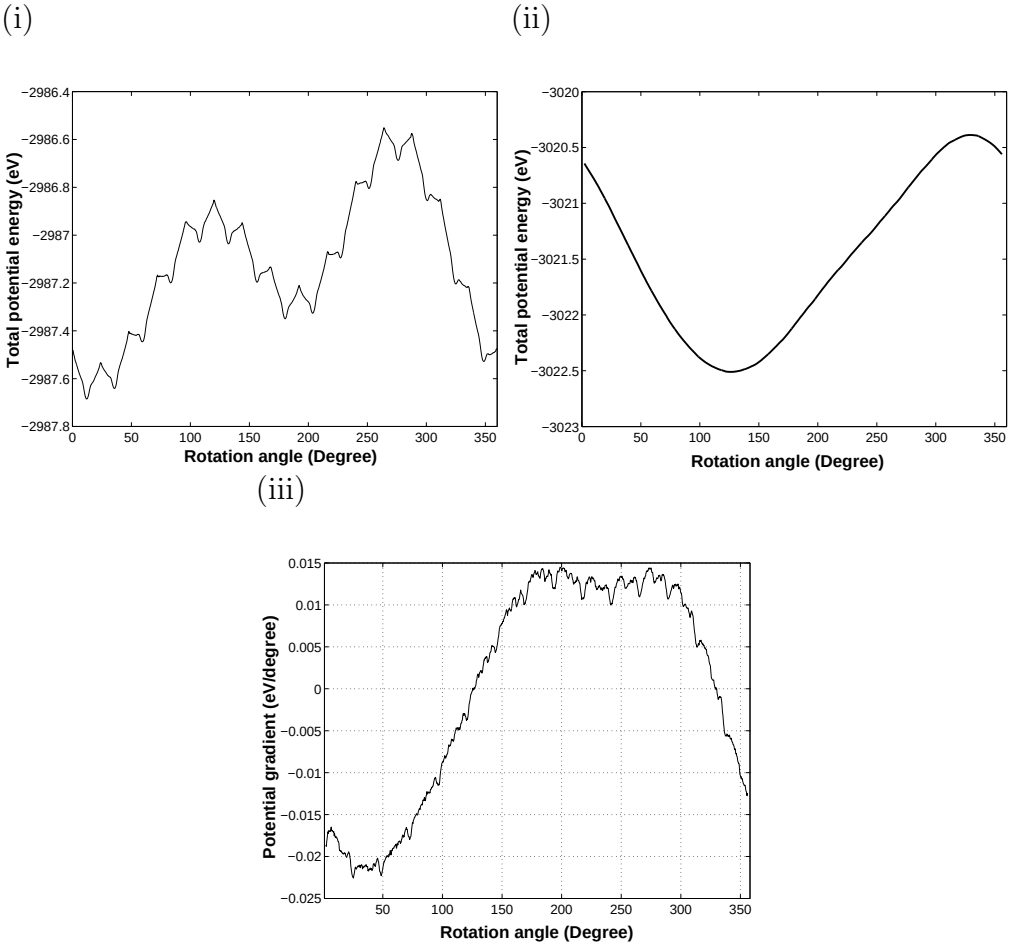

Figure 5.1: (i) Total potential energy (eV) of the system as a function of angular orientation of shaft (θ) inside the immobilized sleeve before NPT thermalization. (ii) Total potential energy (eV) of the system as a function of the angular rotation of the shaft inside the fixed sleeve after NPT thermalization. (iii) Derivative of the total potential energy (eV) with rotation angle θ (deg).

as seen in the figure. The potential energy surface of the system is calculated by summing over the potential energy of all the atoms when the shaft is rotated about the centroid (0,0). Therefore in this case the shaft atoms which are away from the sleeve will not contribute much to the total potential energy of the system. That is why we see a smooth PES after doing NPT relaxation.

Merkle's paper [54], does not take into consideration this kind of centroid shift in the shaft. But he assumes symmetry around the Z axis which does not apply to this case. So this case of the PES calculation after NPT relaxation is an exception to the Merkle's formula.

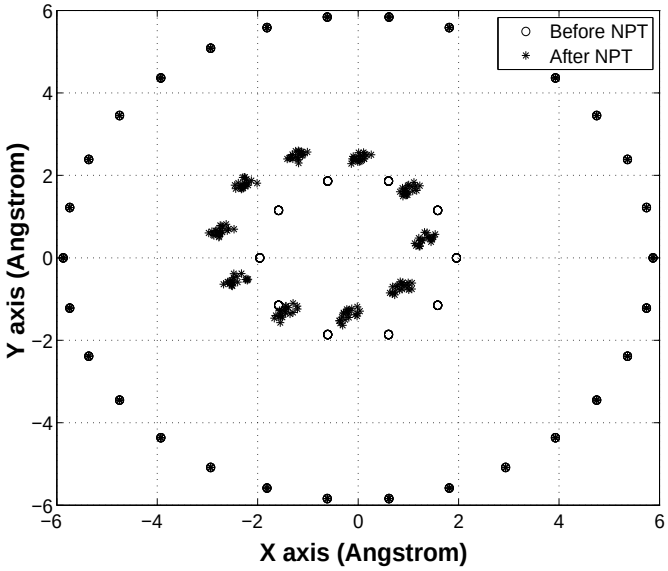

Figure 5.2: X and Y coordinates of the atoms showing displacement of the shaft centroid after NPT relaxation.

5.3.3 Operating frequency

A simple theoretical model, based on rigid-body rotation of the shaft [55], is used to calculate an operating frequency point for the motor as follows:

$$\frac{d}{dt}(I_1\omega_1) = -\tau_{12} + E_a cos(w_E t) \times 2qR_a sin(\theta_E) \tag{5.3}$$

$$\frac{d}{dt}(\theta_E) = \omega_1 \tag{5.4}$$

$$\tau_{12} = R_a \times \frac{d\phi}{d\theta} \tag{5.5}$$

where τ_{12} is the drag force acting between the shaft and the sleeve which is given as the product of shaft radius R_a and the gradient of the total potential of the system in the direction of rotation i.e $d\phi/d\theta$, q is the unit electronic charge, E_a and ω_E are the amplitude and frequency of the applied electric field and θ_E is the angle which the line joining the two charged atoms make with the electric field. The values of I_1, I_2 and R_a are kept constant here. The initial value of θ_E is 20 degree for this case.

These equations are solved numerically using a fourth order Runga-Kutta method to get the instantaneous values of the shaft angular velocity ω_1. With trial and error, we get a unidirectional motion of the shaft at an applied field frequency of 2.0×10^{12} rad/sec and amplitude 1.1×10^{10} V/m as seen in Fig. 5.3. The corresponding vari-

ation of rotation angle θ is shown in Fig. 5.4. It is noteworthy that motor-like behavior occurs at an amplitude ~ 4 times higher than the simple estimate made in Subsection 5.3.1. Also, motor-like behavior is observed 200 ps after start, out of a total simulation time of 800 ps.

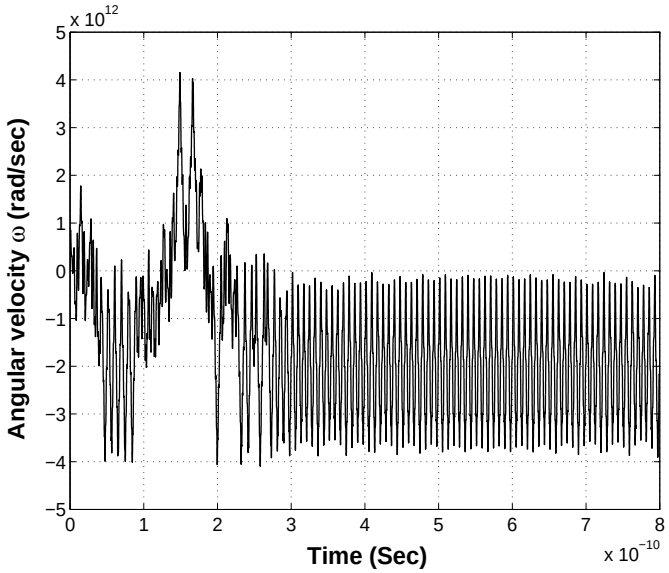

Figure 5.3: Temporal variation of the shaft angular velocity (rad/sec) inside static sleeve at an applied field of frequency 2.0×10^{12} rad/sec and amplitude 1.1×10^{10} V/m. This operating point is obtained from the theoretical model wherein full unidirectional motor-like behavior is observed.

Having obtained a simple estimate of a useful amplitude-frequency combination, the next step is to proceed to full MD simulations to study the parameter space around this nominal operating point.

5.4 Results and discussion

MD simulations have been performed for a DWNT-based electrically-driven nanomotor system. The applied electric field has a component only along the x-direction, i.e., E_x. The amplitude and frequency of this field are varied around the nominal operating point determined from the theoretical model in the last Section.

Unidirectional motor-like behavior of the shaft is observed on application of a field amplitude of 1.1×10^{10} V/m and a frequency of 2.0×10^{12} rad/sec which

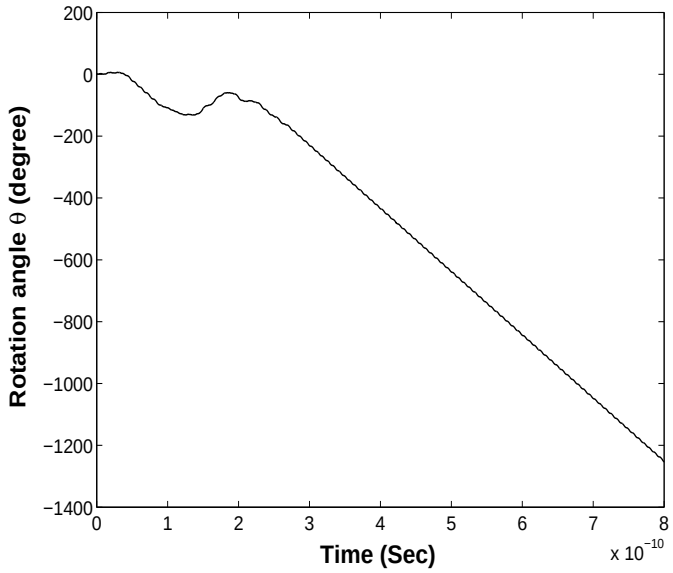

Figure 5.4: Temporal variation of the rotation angle $\theta(degree)$ of the shaft inside static sleeve at an applied field of frequency 2.0×10^{12} rad/sec and amplitude 1.1×10^{10} V/m. Note that for times >200 ps, θ changes monotonically, indicating unidirectional motion.

was obtained from the theoretical model. The instantaneous angular velocity $\omega(t)$ (rad/sec) of the shaft inside the fixed sleeve is shown in Fig. 5.5, and can be seen to vary between (1-3)$\times 10^{12}$rad/sec. Thus the instantaneous value of the shaft angular velocity lies close to the applied value of 2.0×10^{12} rad/sec. The angular velocity does not change sign, which implies full unidirectional motion of the shaft inside the sleeve. Fairly large fluctuations in ω are observed, which could be due to three physical reasons as well as a 'numerical' reason, as explained below. Firstly, even with rigid-body rotation of the shaft, the effective drag force due to potential energy barriers varies as a function of angular position of the shaft. Secondly, the applied electric field produces distortions in the shape of the shaft, which in turn modifies the potential energy barriers. Thirdly, the torque applied by the electric field varies with the relative angle between the electric field (x-direction) and the line joining the two charges. There could also be numerical 'noise', since the average angular velocity ω is computed by averaging over all atoms in the simulation.

The parameter space around this amplitude and frequency point is then explored to get a region where full unidirectional motion of the shaft can be observed. Two sets of simulations are performed. Either the field amplitude or the frequency is varied over a range of values, while keeping the other one fixed.

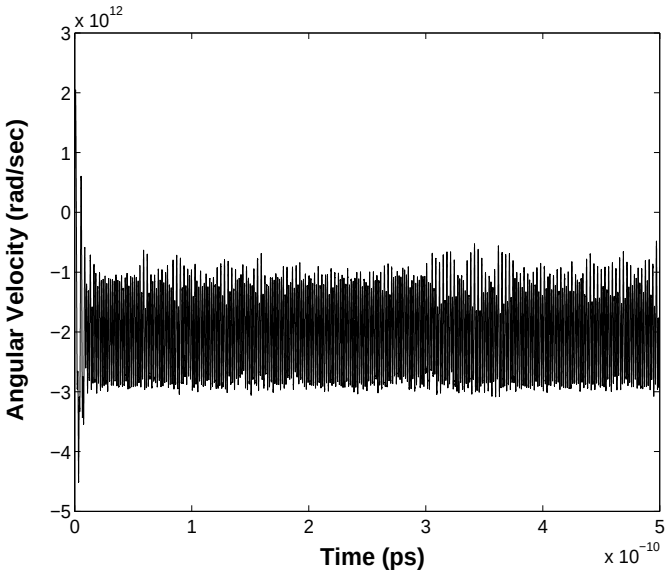

Figure 5.5: Temporal variation of the shaft angular velocity (rad/sec) inside the static sleeve at an applied field of frequency 2.0×10^{12} rad/sec and amplitude 1.1×10^{10} V/m obtained from MD. Fairly large fluctuations are seen in the angular velocity, expected cause of which is explained in the text.

5.4.1 Case 1 : Fixed $\omega_E = 2.0 \times 10^{12}$ rad/sec

The applied field frequency is kept fixed in this case at $\omega_E = 2.0 \times 10^{12}$ rad/sec, while the amplitude is varied from 0.19×10^{10} V/m to 2.89×10^{10} V/m. Let us define R_{max} as the maximum radial position of any atom in the shaft, as measured from the instantaneous centroid of the shaft. R_{max} is a measure of the distortion produced in the shaft due to application of the electric field. Before the electric field is applied (initial conditions), the average radius of the shaft $R_{av,init} = 2.27$ Å and $R_{max,init}$ is 2.74 Å.

For each applied combination of electric field amplitude and frequency, R_{max} is a function of time which can be determined from MD results. The highest value of R_{max}, throughout the simulation period, is recorded, and is shown in Fig. 5.6 as a function of field amplitude. As expected, R_{max} increases with the electric field amplitude, thereby making the potential energy barriers stronger, which enhances the hindrance to pure rotational motion of the shaft.

The complete range of the applied field amplitudes is divided into three regions, which are discussed below.

- Region 2 : Full unidirectional motion of the shaft is observed in this region,

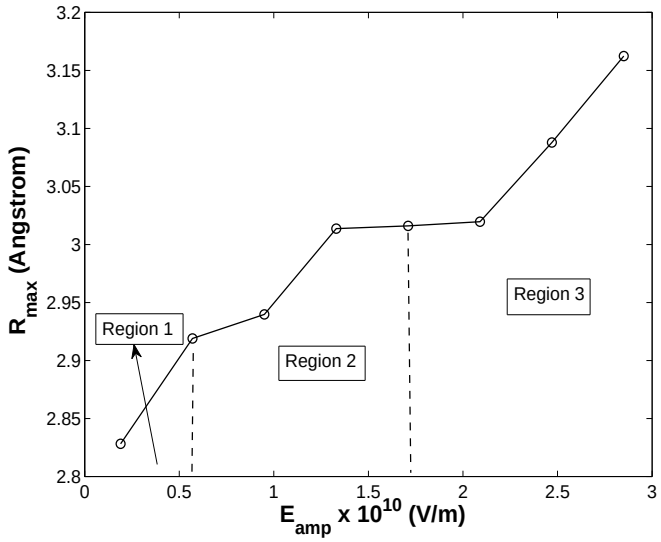

Figure 5.6: Variation of R_{max} (Å) over the whole range of the applied field amplitudes $(0.19 - 2.89) \times 10^{10}$ V/m. The frequency of the applied field is kept constant here as 2.0×10^{12} rad/sec. Region 2 observed to be the operational region in this range where unidirectional motor-like behavior is observed.

where the amplitude varies between $(0.57-1.70)\times 10^{10}$ V/m. Correspondingly, R_{max} varies between 2.92 and 3.01 Å. Over this range of small distortions, there is a relatively small increase in the potential energy barriers, which makes unidirectional motion possible. Hence Region-2 is found to be the useful region over the range of field amplitudes examined in this work.

- Region 3 : In this region R_{max} varies from 3.01 to 3.16 Å and unidirectional motion is not observed. This is due to a greater enhancement in potential energy barriers.

- Region 1 : At 0.19×10^{10} V/m, R_{max} observed is 2.83 Å. However, unidirectional motion is not observed in this case. This can be explained in term of the threshold electric field amplitude, E_{th}, required to overcome the potential energy barriers in the CNT configuration, as explained in Section 5.3.1. The potential energy surface (PES) and E_{th} calculated from the gradient of the PES w.r.t rotation angle θ is shown in Fig. 5.7 for two different values of the applied electric field amplitudes. For an applied field amplitude of 0.19×10^{10} V/m, the DWNT configuration is observed to have a E_{th} of 0.195×10^{10} V/m, slightly higher than the applied value. This explains why unidirectional

motion is not observed. By comparison, in Region-2, for an applied field of 0.57×10^{10}V/m, E_{th} is found to be 0.4×10^{10} V/m, i.e., the applied field is well above the threshold field.

(i) $E_a = 0.19\times10^{10}$ (V/m) (ii) $E_a = 0.57\times10^{10}$ (V/m)

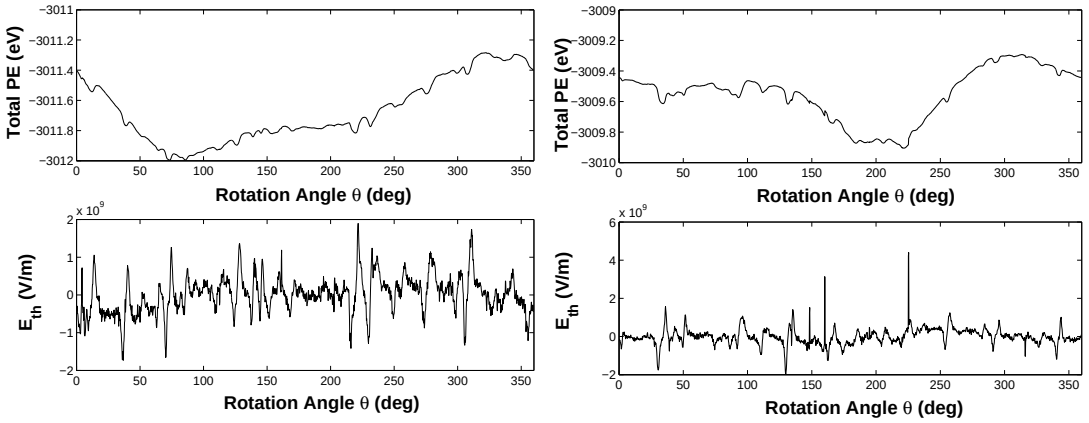

Figure 5.7: PES and the corresponding threshold electric field E_{th} calculated from the gradient of PES for an applied field amplitude of (i) 0.19×10^{10} and (ii) 0.57×10^{10} V/m. E_{th} is observed to be (i) 0.195×10^{10} V/m (ii) 4×10^{10} V/m. Note that E_{th} is greater than the applied field in the first case, which hinders unidirectional rotation. In the second case, the applied field is higher than E_{th}, which makes unidirectional rotation possible.

5.4.2 Case 2 : Fixed $E_a = 1.1\times10^{10}$ V/m

The amplitude of the applied field is kept fixed at $E_a = 1.1\times10^{10}$ V/m and the frequency ω_E is varied from $(1.5-7.5)\times10^{12}$ rad/sec. The corresponding variation of R_{max} is as shown in Fig. 5.8. This frequency range can be divided into 4 different regions as follows:

- Region 1 : In this region, R_{max} is observed to be ∼3.1-3.2 Å . Unidirectional motion is not observed in this region because of the high distortion produced in the shaft which, in turn, makes the potential energy barriers higher.

- Region 2 : This region includes the points of applied frequency from 2.0×10^{12} to 3.5×10^{12} rad/sec. The R_{max} varies from 2.79 to 3.05 Å in this region and full unidirectional motion of the shaft is observed. This region also includes our nominal operational point in the amplitude-frequency space, i.e., applied

frequency of 2.0×10^{12} rad/sec. The distortions of the shaft are lower as compared to Region-1, since the shaft atoms have less time to respond to the applied electric field.

- Region 3 : This region includes applied frequency ranging from 4.0×10^{12} to 6.0×10^{12} rad/sec. We do not observe unidirectional behavior in this region. A maximum R_{max} value of 3.92 Å is observed in this region for an applied frequency of $\omega_E = 5 \times 10^{12}$ rad/sec. PES are calculated for different applied frequencies in this region, and the maximum barrier height (in eV) is measured as listed in Table 5.1. The PES is shown for three different values of the applied frequencies in Fig. 5.9. Note that the PES is calculated by rigid-body rotation of the shaft configuration obtained at the point of maximum distortion. A maximum barrier height of 2.5 eV is observed for an applied frequency of 5×10^{12} rad/sec. This value of barrier height becomes progressively smaller as we move away from 5×10^{12} rad/sec to other frequencies. A physical explanation for this peak is given in the next Section.

- Region 4 : This region includes applied frequency from 6.5×10^{12} to 7.5×10^{12} rad/sec. R_{max} varies from 2.92 to 3.01 Å in this region which is close to the distortions seen in Region 2, still unidirectional motion is not observed in this region. This is because the frequency of the applied field is significantly higher in this region which does not give enough time to the shaft to complete a full rotation before the field reverses sign.

5.5 Explanation for sharp peak in R_{max}

In Region 3 of Fig. 5.8, we have seen a sharp peak in R_{max} over some range of variation of the applied frequency. Such a variation is observed only with variation in frequency, not with changes in the amplitude. Hence it is natural to hypothesize that there is some resonant effect involved – it may be that the applied frequency happens to match a natural frequency of the DWNT. Hence it is first necessary to determine the characteristic frequencies of this DWNT system.

Earlier we have used the novel technique of Singular Value Decomposition (SVD) to study the modes of a (5,0) SWNT [73] and a (5,0)@(15,0) DWNT. Similar to that

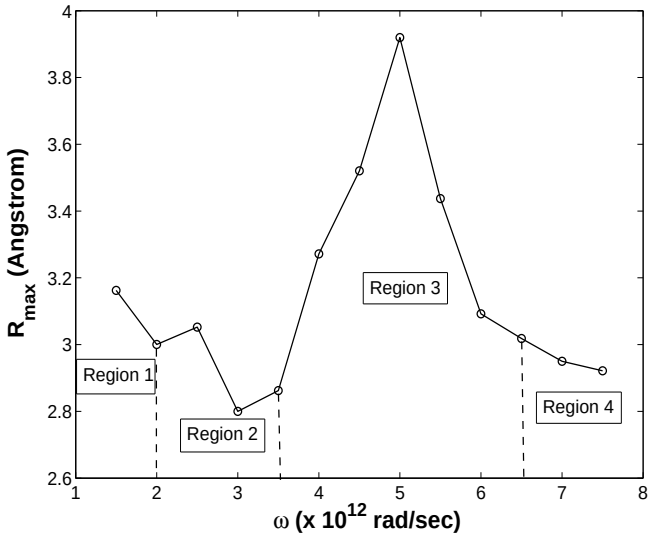

Figure 5.8: Variation of R_{max} (Å) of the shaft atoms as a function of applied frequency. The range is divided into four regions. The field amplitude is kept constant as 1.1×10^{10} V/m. Region 2 is the region of interest where unidirectional motor-like behavior is observed. A sharp peak in R_{max} of 3.92 Å at 5.0×10^{12} rad/sec is observed, which is explained in the text.

we perform a SVD analysis on the MD data for the shaft [73].

MD simulation for the nanomotor with a 'frozen sleeve', under NPT conditions, and without the application of an external field, generates a time series of atomic coordinates for all the atoms in the shaft. This time series data is analyzed using SVD. The SVD gives the modes of the system in the descending order of the amplitudes. We study first ten significant modes in detail and the distortion associated with each mode as in [73]. An ($m_\theta = 0$, $m_z = 1$) mode with radial symmetry is observed at a frequency of 26 cm^{-1} (5×10^{12} rad/sec) as the 4th SVD mode. This mode correspond to the centroid displacement of the individual rings as shown in Fig. 5.10. This centroid displacement is calculated w.r.t to the instantaneous centroid of the ring. Note that the centroid displacement shown in this figure is in arbitrary units.

We then calculate the actual centroid displacement of the individual rings from their own instantaneous centroids from the MD data as in Fig. 5.11. This is calculated for different applied frequencies from 3×10^{12} to 7×10^{12} rad/sec. This centroid

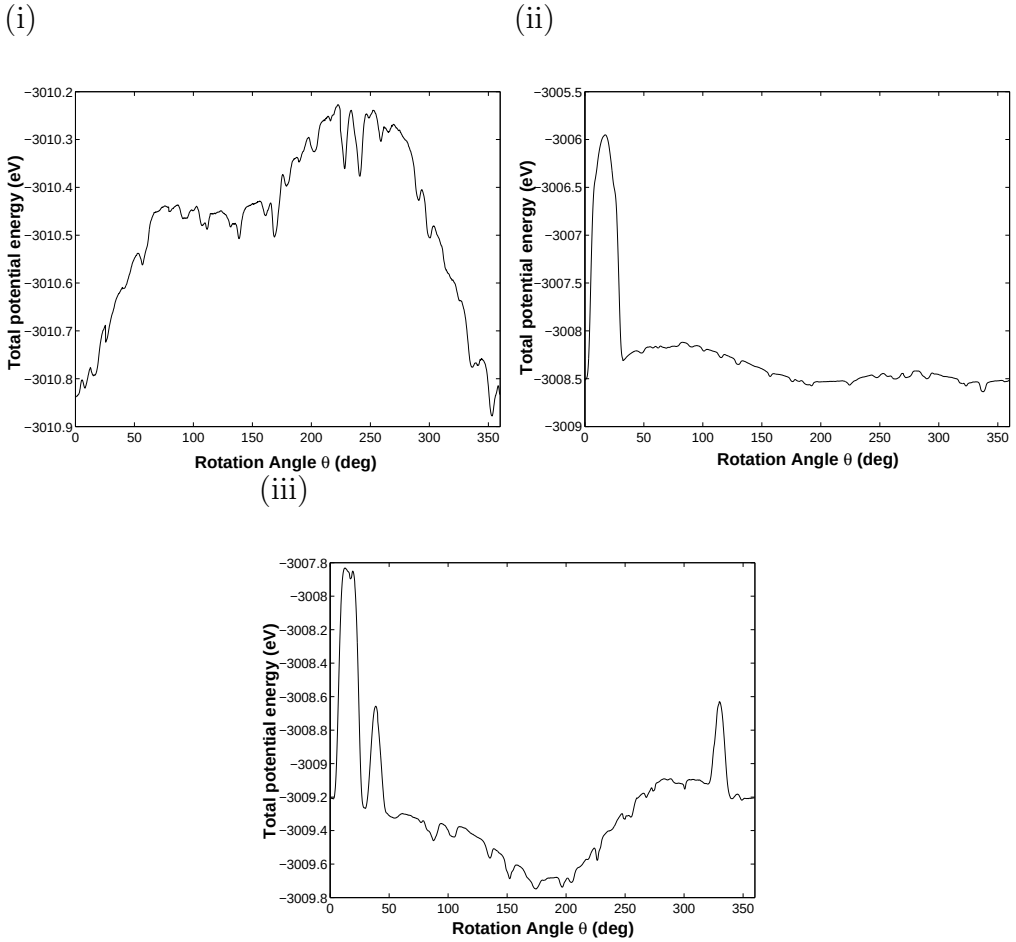

Figure 5.9: PES shown for three different cases of the applied field frequencies (i) 4.5×10^{12} (ii) 5.0×10^{12} and (iii) 5.5×10^{12} rad/sec. Note that the PES is calculated at the point of maximum distortion of the shaft i.e when R_{max} is maximum. A maximum barrier height of 2.5 eV is observed for the case where applied field frequency is 5.0×10^{12} rad/sec.

displacement (in Å) is then added to the average radius of the shaft, $R_{av,init}$, to get the actual displacement of the individual rings due to the excitation of ($m_\theta = 0$, $m_z = 1$) mode. All these values are listed in Table 5.2. A maximum centroid displacement of 1.95 Å is observed for an applied frequency of 5×10^{12} rad/sec. The trend looks qualitatively similar to the trend of R_{max} obtained directly from MD. The slight differences in the numbers could be because of the effect of some other modes at this frequency. The effect of the excitation of this mode can also be seen at nearby frequencies, where a significant increase in R_{max} is seen.

The conclusion is that application of a frequency around 5×10^{12} rad/s resonantly

$\omega_E(\times 10^{12} rad/sec)$	*Maximum barrier height* (eV)
3.5	0.16
4.0	0.36
4.5	0.60
5.0	2.50
5.5	2.00
6.0	1.35

Table 5.1: The maximum height of the potential energy barrier (eV) as a function of applied frequency, for an applied electric field amplitude of 1.1×10^{10}V/m

.

$\omega_E(\times 10^{12}(rad/sec)$	R_{max} ($\mathring{A}$)	$R_{centroid}(\mathring{A}$)	$R_{centroid} + R_{av,init}(\mathring{A}$)
3.0	2.799	1.20	3.38
4.0	3.272	1.42	3.60
5.0	3.919	1.95	4.13
6.0	3.092	1.36	3.54
7.0	2.950	1.20	3.38

Table 5.2: Columns in the table show the applied frequency of the field ω_E, R_{max} directly obtained from the code, displacement in the centroid $R_{centroid}$ and $R_{centroid}$ added to the average equilibrated radius of the shaft $R_{av,init}$. Note that a maximum centroid displacement of 1.95 Å is observed for applied frequency of 5.0×10^{12} rad/sec.

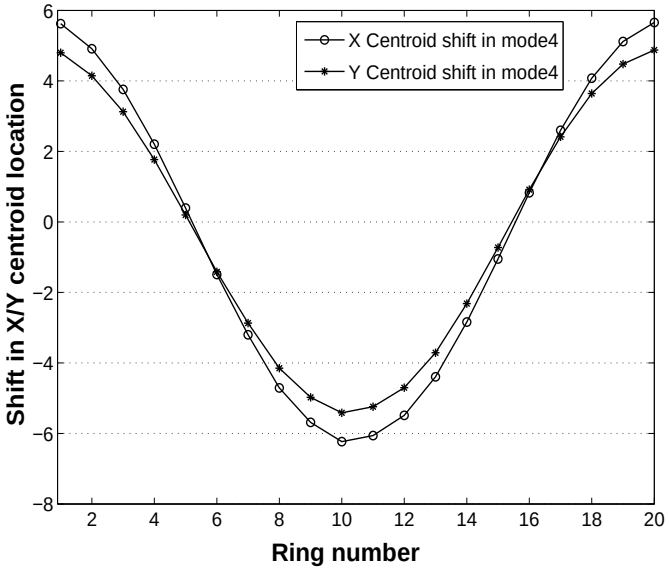

Figure 5.10: X and Y centroid displacement of the individual rings of the shaft as obtained after doing SVD analysis on the MD data. Note that the displacement is in arbitrary units here.

excites a mode corresponding to centroid displacement. This shows up as a peak in R_{max}, even though the actual cause is displacement of an entire CNT ring away from the initial axis.

5.6 Conclusions

A numerical analysis has been performed for a double-walled carbon-nanotube based nanomotor driven by an externally applied sinusoidally varying electric field, in the presence of a 'frozen' sleeve. Our earlier study had shown that distortion of the nanomotor due to the applied field can lead to the production of 'locked' states, where the nanomotor exhibits only intermittent or oscillatory motion. In this Chapter it has been shown that to produce unidirectional (motor-like) rotation, it is necessary to operate over a 'useful' region in the parameter space defined by the amplitude and frequency of the applied electric field.

Firstly, a simple rigid-body rotation model has been used to determine a nominal operating point. This has been followed by a systematic molecular dynamics study around this nominal point. For a given frequency, electric field amplitudes below a threshold are not able to overcome the potential energy barriers due to interaction

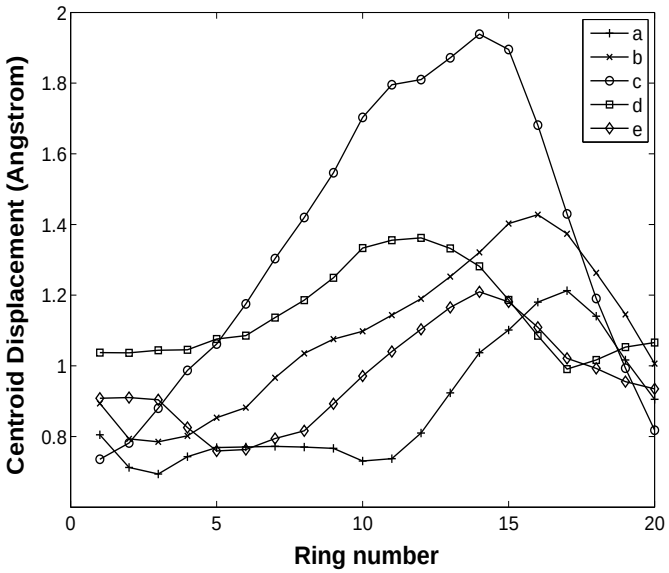

Figure 5.11: Centroid displacement (Å) calculated directly from the MD for individual rings of the shaft. Here (a-e) curves correspond to the applied frequencies $(3-7)\times 10^{12}$ rad/sec. Note that a maximum centroid displacement of 1.95 Å is observed for an applied frequency of 5×10^{12} rad/sec which is explained in the text.

of the rotating shaft with the frozen sleeve. This is followed by a range of amplitudes where unidirectional motion is observed. At still higher amplitudes, distortion of the shaft increases the potential energy barriers to levels higher than those that can be overcome by the electric field. Hence we get three regions during the amplitude scan, only one of which is useful for a nanomotor.

For a given amplitude, as the frequency is varied, more complex behavior is obtained, which can be broken up into four regions. At low frequencies (Region-1), large distortion of the shaft leads to an increase in potential energy barriers, hindering rotation. Over an intermediate range (Region-2), unidirectional motion is observed, since shaft distortions are smaller than in Region-1. This is followed by an anomalous region (Region-3), where resonant excitation of a characteristic mode of the shaft leads to very large distortions, which greatly enhance the barrier. Finally, in Region-4, the distortion again starts falling off with rise in frequency. However, the frequency is now so high that the shaft cannot complete a full rotation before the field reverses sign. Hence unidirectional rotation is not obtained. A detailed physical explanation has been provided for the anomalous behavior in Region-3, in terms of resonant excitation of characteristic modes.

Chapter 6

Molecular Dynamics simulations of a Carbon Nanotube interacting with a Graphite Surface

6.1 Introduction

We have so far determined the useful parameter space of a DWNT-based nanomotor. Depending upon the application, such a nanomotor should be attached to some surface, e.g. a carbon or metal surface. In some cases, it may also be necessary to pass a current through the nanomotor. For example, the high electrical conductivity of CNTs, depending on their diameter and helicity, make them good candidates as nanowires for electrical devices. However, the contact resistance of the CNTs with the electrical device is an important parameter in deciding their suitability for this purpose.

The next step must, therefore, be to understand the interaction of CNTs with other surfaces. To explore such possibilities, as a first step we study the interactions of a Single-walled carbon nanotube with a graphite surface.

Experimental [74] and theoretical [75] studies indicate that the nanotube distortions affect their electronic transport properties. Hertel et al. investigated the interaction of single wall nanotubes (SWNT) and multiwall nanotubes (MWNT) with a graphite surface using both experiments and molecular statics simulations [76].

They used the MM3 force field, which is a Molecular Mechanics based potential and used a Newtons method [77] to minimize the energy of the system so as to attain a ground state configuration of the system. They showed that depending on the tube diameter and number of shells, the Van der Waals interaction between nanotubes and a substrate results in higher binding energies due to which the carbon nanotube acquires a larger contact area over the graphite surface. This is essentially a Molecular statics simulation at 0 K, and higher temperatures effects, as can be expected at the points of contact resistance, do not show up. We therefore perform MD simulations of carbon nanotubes of various diameters interacting with a graphite surface at different temperatures (100 K, 300 K and 500 K) to study the effect of temperature on the interaction. We also study the effect of nanotube-nanotube separation distance on the interaction of CNT with graphite using MD.

6.2 Setting up the MD simulations

In this section we describe the process of setting up our MD simulations. We used armchair carbon nanotubes of diameters 8.105, 13.541, 20.290 and 27.110 Å and length 76.570 Å in our simulations. The number of atoms simulated were 2880-3680 for the simulations.

6.2.1 Structure equilibration

The nanotubes and the graphite structures were relaxed at zero pressure and temperature 100 K using Berendsen's pressure and temperature controls as discussed in earlier chapters. These relaxed SWNTs were then translated and rotated to sit on the top of the graphite structures at a separation distance of 3 Å to get a structure such as that shown in Fig. 6.1. We choose an axis such that the graphene plane lies in the X-Y plane. The Z axis is perpendicular to this graphene plane. The axis of the CNT lies along the X axis of the graphite structure.

6.2.2 Periodic boundary conditions used

Periodic boundary conditions (PBC) are used along X and Y directions to get repetitive structures along these directions. This means that if the distance between the outermost edge of the CNT and the graphite edge is smaller than half the cut off

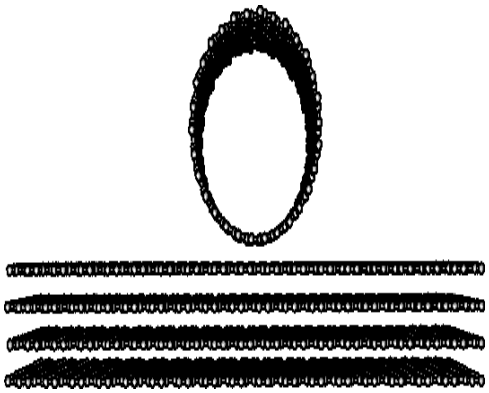

Figure 6.1: CNT translated and rotated to sit on the top of a graphite crystal

distance of the long range interlayer potential term, the CNT will be seeing its opposite edge due to the PBC in the Y direction. Along Z direction we use free boundary conditions.

6.2.3 Types of simulations performed

Two sets of simulations are performed, one set consist of the simulations done at different temperatures (100 K, 300 K and 500 K) to study the dynamics of various sized CNT's interacting with the graphite surface. The second set of simulations were carried out to study the effect of the separation distance between neighboring CNTs. This separation distance was varied by varying the graphite size in the simulations and using PBC along the Y direction. The nanotubes having an initial separation of 51.303, 16.429, 11.175 and 2.667 Å are studied. The MD simulations are performed for 100 pico-seconds with a time step 0.1 fs. The system was allowed to relax to zero pressure using Berendsen pressure control at different temperatures using Berendsen thermostat such that it attains a minimum energy state.

6.3 Results and Discussion

In this section we describe the results of our MD simulations as follows:

- Interaction of SWNTs of different diameters with graphite structure at a constant temperature (100 K).

- The effect of temperature on the contact area between SWNTs and the substrate.
- The effect of separation distance between neighboring SWNTs on their distortions.

6.3.1 Interaction of SWNTs of different diameters with graphite surface at 100 K

The results of the MD simulations at 100 K are as shown in the Fig. 6.2. At 100

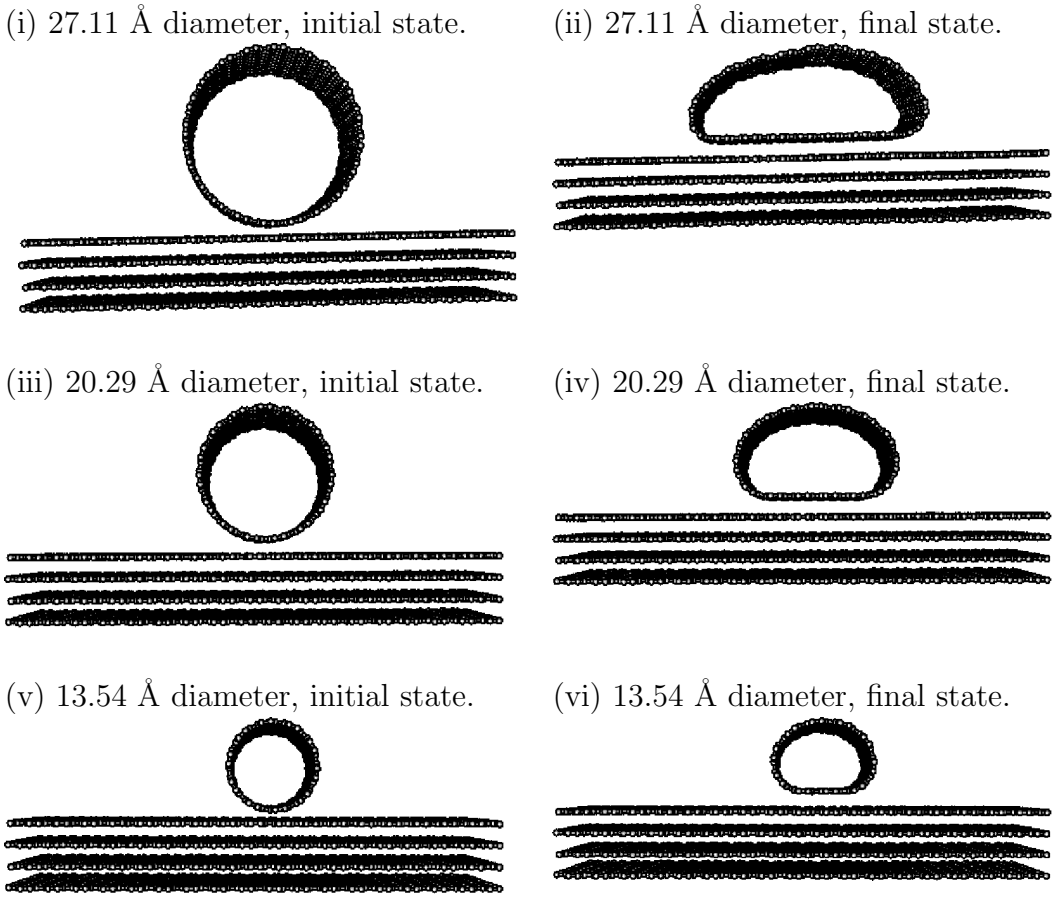

Figure 6.2: The initial and final states of a MD simulation of SWNT of different diameters on graphite at 100 K. Note that the SWNT with larger diameters deform more.

K we observe that the nanotubes of larger diameters acquire larger contact area on the top of the graphite surface. The tubes are seen to deform to have a larger

contact area with the graphite surface and thus have larger binding energy with the graphite surface as they maximize their contact area with the surface. We compare the binding energy per unit length along the axis of the CNT, obtained from our MD calculations at 100 K with that of [76] as shown in Fig. 6.3. The trends are observed

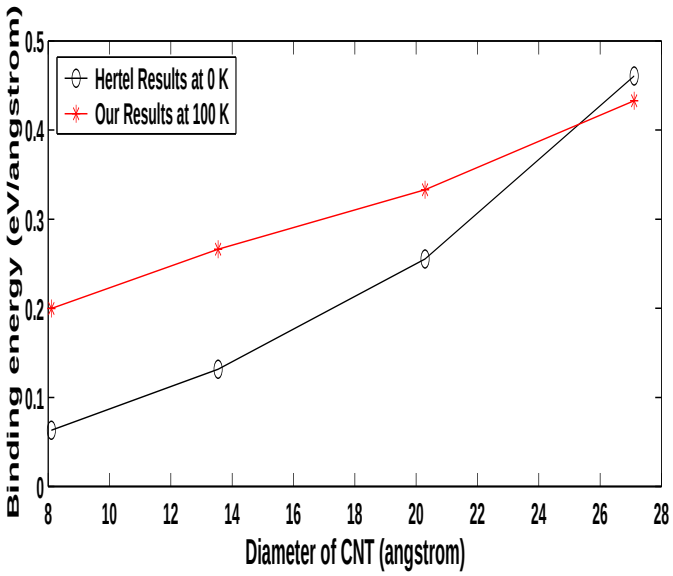

Figure 6.3: Comparison of variation of Binding energy in (eV/Å) as obtained from our MD simulations at 100 K with the results of MM simulations.

to be the same and we see that the binding energy per unit length increases with the diameter of the CNT. There is however a quantitative mismatch which could be due to the different kind of potential used and the effect of temperature. Hertel et. al give the total energy of the system as an integral of the strain energy u(c) and the adhesion energy over the entire tube profile:

$$E = \int ([u(c) + V(z)])dx, \tag{6.1}$$

with c(x) being the local nanotube curvature and V(z(x)) the nanotube-substrate interaction potential at a distance z above the surface (eV/Å). They explain this flattening of the nanotubes as the compensation between the strain energy developed in the nanotube due to deformation and the gain in the binding energy as the tube maximizes its contact area with the substrate. We plot the potential energy of the atoms in the system as shown in the Fig. 6.4. The atoms in yellow and red colors, at the deformed edges of the nanotube, are at a higher potential then the atoms in the blue color.

(a) SWNT of diameter 8.105 Å (b) SWNT of diameter 13.541 Å

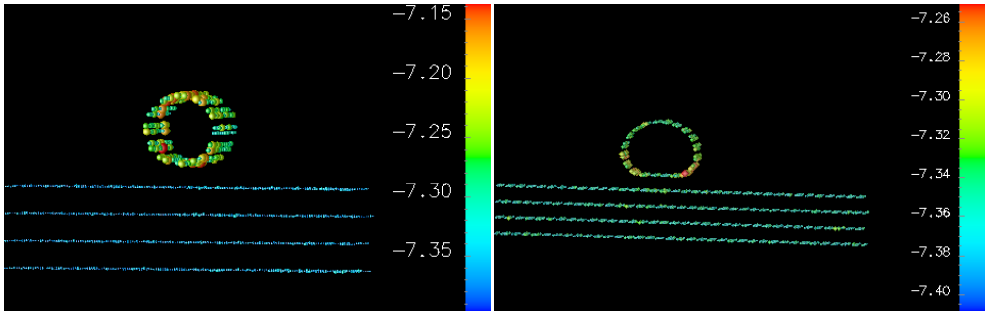

(c) SWNT of diameter 20.290 Å (d) SWNT of diameter 27.110 Å

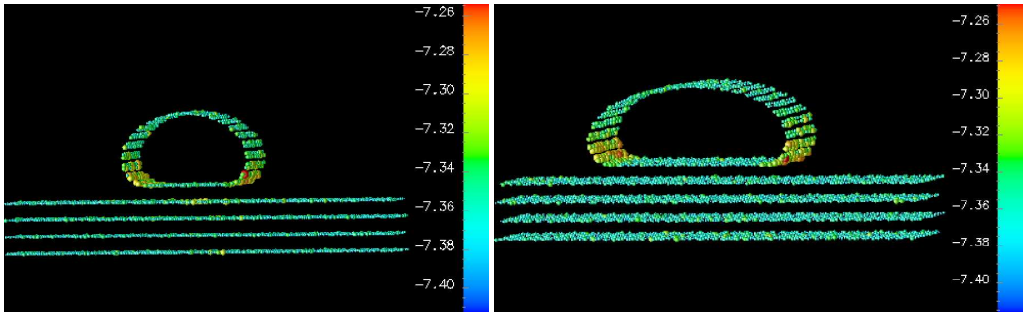

Figure 6.4: The final states of a MD simulation of SWNTs on a graphite surface at 100 K. The colorbar depicts the potential energy of different atoms of SWNT in (eV).

6.3.2 Temperature effects on the interactions of SWNTs and graphite

Temperature seemed to be playing an important role on the contact of different SWNTs with the graphite surface as shown in the Fig. 6.5. We find that the contact area between the nanotube and the graphite surface becomes progressively smaller as the temperature is increased. The higher temperatures imply that the atoms get higher kinetic energies because of which they are able to overcome the interactions between the tube and the graphite. The variation of binding energies with the temperature are as shown in the Fig. 6.6. The plots show that the binding energy per unit length decreases with the temperature, which is also observed in the simulations as the contact area between the tube and the graphite decreases. We notice that the CNT's of smaller diameters (8.105 Å) move away from the graphite surface at a temperature of 500 K as shown in the Fig. 6.7. Note that from (a) to (f) the contact area of the CNT with the graphite surfaces decreases. This flying away of the small

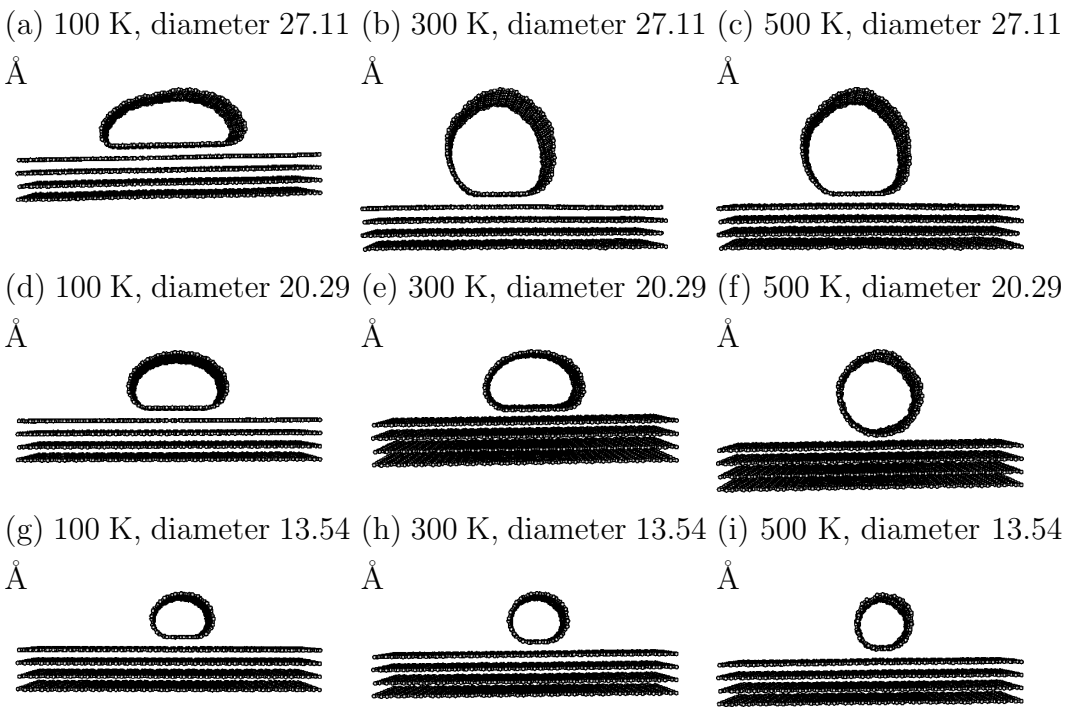

Figure 6.5: The final states of a MD simulation of CNT of diameters 27.11 Å 20.29 Åand 13.54 Å at different temperatures. Note that the deformation of the SWNT decreases with temperature.

sized CNT could be due to some thermal effects which needs further analysis. To summarize, we observe that there is a temperature effect of the binding energy. The binding energy decreases with increase in temperature. This effect is observed to be stronger for lower diameter SWNTs (diameter 8.105 Å). At 300 and 500 K the binding energy for this SWNT becomes nearly zero, as seen in the Fig. 6.6.

6.3.3 Effect of separation distance between neighboring SWNTs on tube distortion

We also study the effect of separation distance between the neighboring CNTs on their flattening on the top of graphite surface. CNT bundles are used to make contacts and here we are exploring a realistic situation where the bundles are beside each other. We are finding maximum distance between CNTs that will give maximum contact area and assure best contact with the graphite. This separation distance is varied by changing the size of the graphite surface used in the simulation. We find that in all the simulations where the neighboring CNTs had a separation

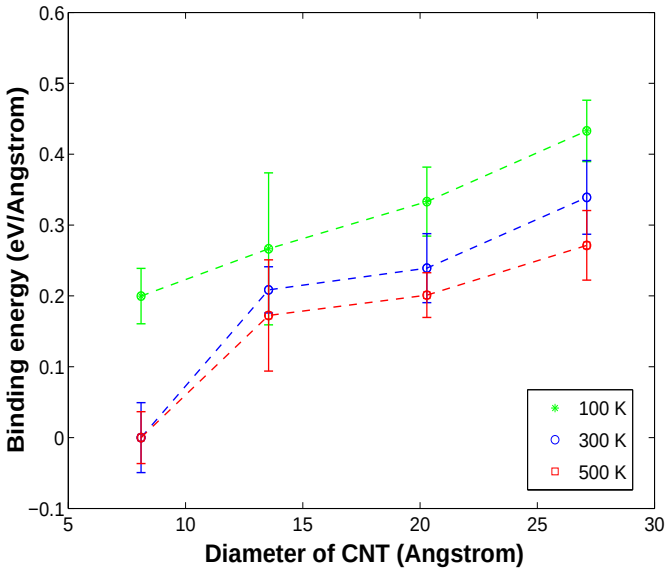

Figure 6.6: Comparison of variation of Binding energy in (eV/Å) as obtained from the MD simulations at different temperatures.

greater than 6.9213 Å show qualitatively good flattening. Nanotubes having a separation of 51.303, 16.429, 11.175 Å before the simulation are observed to have an equilibrium separation of 20.016, 5.929 and 3.023 respectively after a simulation of 100 picoseconds. A contact length of 38.028, 36.68 and 34.017 Å is observed respectively in these cases due to the flattening of the tube on the graphite surface. However when the CNTs were imposed to have a separation distance of 2.667 Å initially, they come as close as 2.054 Å acquiring almost a rectangular shape after the simulation as shown in the Fig. 6.8. In this case a contact length of 29.141 Å and a binding energy per unit length of the nanotube equal to 0.2131 eV/Å is observed. A plot of the potential energy of the atoms in this case is shown in the Fig. 6.9. The figure shows the strain developed on the carbon atoms when the separation distance between the two carbon nanotubes was kept equal to 2.667 Å before the simulation. A variation of the binding energy (eV/Å) developed with the intial nanotube-nanotube separation distance is as shown in the Fig. 6.10. As can be seen from the figure, as the separation distance between the nanotubes decreases the binding energy also decreases.

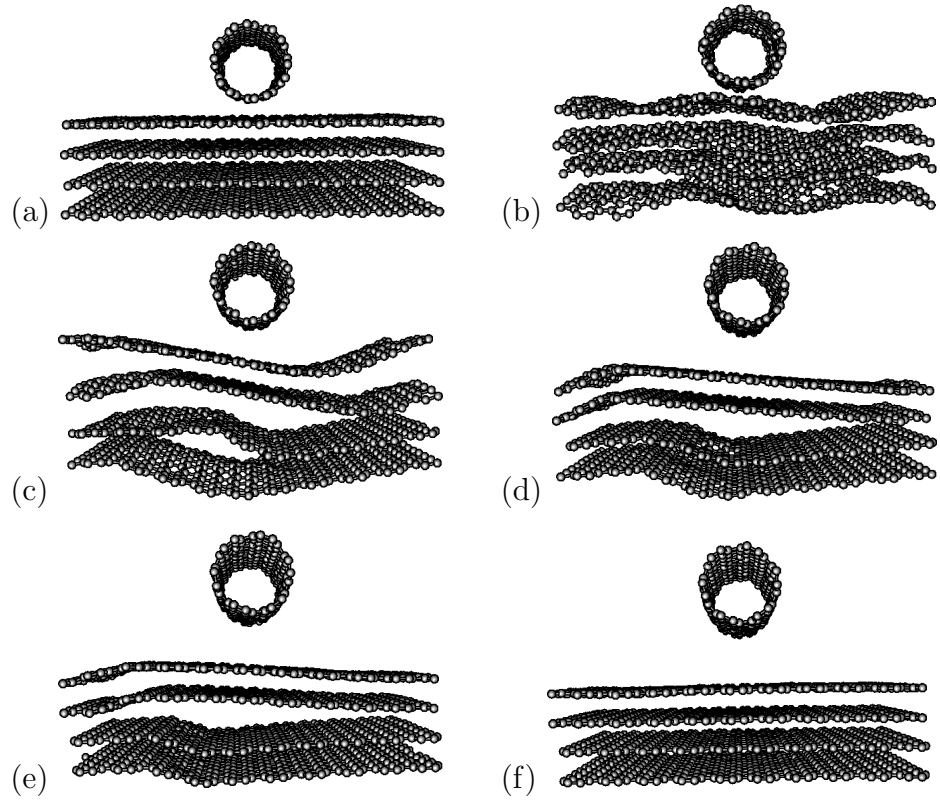

Figure 6.7: Different frames of a movie of a MD simulation of CNT of diameter 8.105 Å on a graphite surface at 500 K (note that from (a) to (f) the contact between CNT with graphite decreases).

6.4 Conclusions

In summary, we have observed that the interlayer forces between the nanotube and the graphite surface gives rise to radial distortions in the nanotube, as reported earlier by Hertel et. al using Molecular Mechanics. The tubes are seen to deform to have a larger contact area with the graphite surface and thus have larger binding energy with the graphite surface as they maximize their contact with the graphite surface. We observe that nanotubes of larger diameters have a larger contact area with the graphite surface, whereas the CNTs of comparatively smaller diameter do not deform to such an extent.

Results at higher temperatures show that the interlayer interactions between the nanotubes and the substrate are overcome by the SWNT which gives rise to a lesser contact area between the tube and the graphite. We observe a decrease in

(i) before simulation. (ii) after simulation.

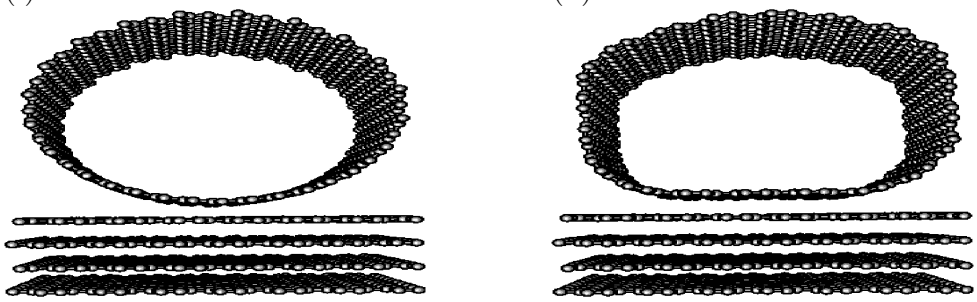

Figure 6.8: The initial and final states of a MD simulation of CNT of diameter 27.110 Å on a graphite surface with a separation of 2.667 Å between CNTs before simulation.

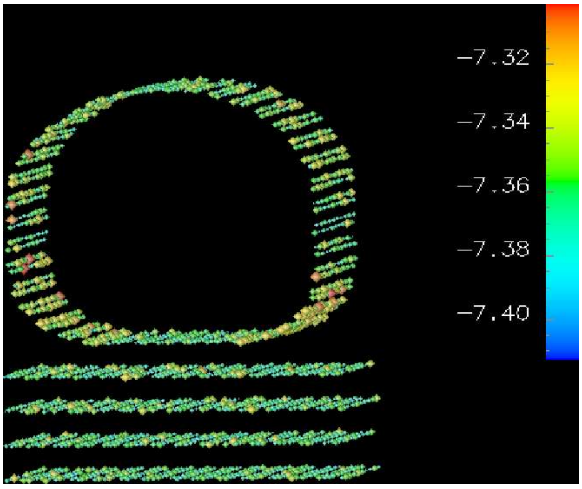

Figure 6.9: Figure showing the strains developed in the nanotube of diameter 27.110 Å with a separation of 2.667 Å between neighboring CNTs before simulation.

the binding energy of the SWNT with graphite with increase in the temperature because of the gain in the kinetic energy acquired by the SWNTs. At a temperature of 500 K, nanotubes of small diameters i.e 8.105 Å are observed to have nearly zero binding energy and fly away from the graphite surface. This needs further analysis. However. such an analysis lies beyond the scope of this thesis.

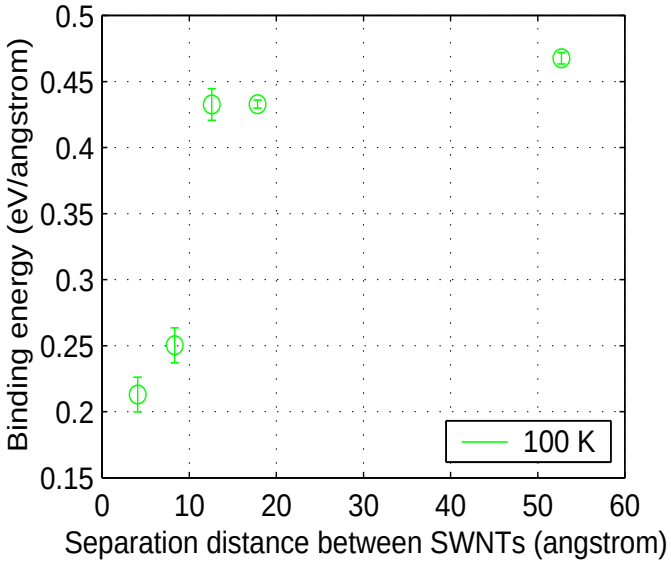

Figure 6.10: Variation of Binding energy in (eV/Å) with the separation distance (in Å) between the nanotubes.

Chapter 7

Conclusions and Future Scope

7.1 Conclusions

Carbon nanotubes have become very important in molecular research because of the various potential applications of nanomachines in the field of computing, electronics, robotics and drug delivery. The high tensile strength and strong mechanical properties of these nanotubes make them a promising candidate for future nanomachinery. These nanometer devices, either alone or attached to a propeller, are a bright candidate for future machines which could be used for medical applications. Nanometer-sized devices, especially nanomotors, based on carbon nanotubes, are of interest for their novel applications in drug delivery techniques.

Other workers have reported the results of Molecular Dynamics simulations of electrically-driven nanomotors based on double-walled carbon nanotubes. Those studies broke new ground and yielded interesting insights into the atomistic level behavior of such nanomotors. However, those studies either did not consider certain aspects of nanomotor operation, or did not investigate them in sufficient detail. Some of those limitations have been addressed in the present thesis.

In this thesis, we report on classical molecular dynamics simulations of a nanomotor based on a DWNT. Two diametrically-opposed atoms at one axial location on the shaft are assumed to have attached charges of equal magnitude but opposite polarity. The application of a linearly-polarized electric field produces a torque, resulting in rotational motion of the shaft with respect to the sleeve. Important results of the study are described below.

7.1.1 Molecular Dynamic simulations of a double-walled carbon nanotube motor subjected to a sinusoidally varying electric field

We performed two sets of simulations. In the first set, where both the shaft and sleeve are free to move, the usual pendulum- and motor-like behavior is observed. Also a simple theoretical model is given. The motion of the shaft and the sleeve obtained from the model matches reasonably well with our MD results, although there are differences of detail.

In the second set of simulations, the sleeve is held fixed. In this case, two locked states, not aligned along the direction of the applied electric field, are observed in the angular orientation of the shaft inside the fixed sleeve. The frequency of shifts between these locked states correspond to the frequency of the applied electric field. These locked states are in contrast to the usual pendulum like motion reported by other workers. The simple theoretical model is incapable of explaining these locked states, An explanation has been found in terms of the radial shape variations of the shaft and shifts in the centroid of the shaft inside the fixed sleeve.

In the limit of no energy losses, i.e., in the absence of any heat bath attached to the system, we observe that the motor breaks apart due to energy acquired from the electric field.

7.1.2 Mode analysis of Carbon Nanotubes based on Molecular Dynamics : A Singular Value Decomposition study

For the first time, the complete set of the characteristic modes of both single-walled and double-walled carbon nanotubes has been extracted using singular value decomposition analysis of molecular dynamics data. For SWNTs, good agreement is observed between the calculated frequency of radial breathing modes and published experimental measurements, as also the inverse scaling of this frequency with tube diameter.

The first part of the study, which focuses on NVE simulations of an isolated SWNT, has been performed with a 5% initial radial stretching given to all its atoms. We find the two strongest modes to involve RBM combined with a very slow rota-

tional motion of individual rings of the nanotube. The coupling between these two motions weakens for a smaller initial perturbation of 1%. The next eight most significant modes consist of two classes, one with $m_z = 0$, i.e.,axial uniformity and the other class has $m_\theta = 0$, with $m_z = 1$ and 2, i.e radial uniformity. For the available cases, the frequencies of the above mentioned modes match well with those in the literature.

Under NPT conditions, similar to laboratory conditions, i.e., at a constant temperature and pressure, mode frequencies change only slightly, but the hierarchy of modes is slightly different.

Resonant excitation of the SWNT is also studied using MD. External excitation produced at one of the mode frequencies, corresponding to centroid motion with ($m_\theta = 0$, $m_z = 1$), shows a significant and steady increase in the amplitude of centroid displacement. Excitation at the second harmonic frequency leads to an initial increase in displacement amplitude, but eventual saturation. These conclusions are important for the application of carbon nanotubes in nano-devices, e.g. as nanomotors.

Similar to the characteristic mode study of an SWNT, the characteristic modes of a DWNT are also studied, for the case where the outer CNT is immobilized. As expected, this geometry produces a higher restoring force, hence it leads to an upshift in the RBM frequency. Also the frequency of some axial modes like (m_θ, m_z) = (0,1) and (0,2), are slightly different from the SWNT case. For some mode numbers (same m_θ & m_z), where an SWNT exhibited a single frequency, a DWNT exhibits more than one peak in the power spectrial density. This is possibly due to coupling between different modes due to interaction with the outer CNT.

7.1.3 Determination of useful parameter space for a double-walled carbon nanotube based motor subjected to a sinusoidally varying electric field

A theoretical model is given which gives a nominal operating point in the amplitude-frequency space where pure unidirectional motor-like behavior of the motor is observed. The full parameter space around this operating point is then explored using molecular dynamics simulations.

For a given applied frequency, electric field amplitudes below a threshold are not able to overcome the potential energy barriers due to interaction of the rotating shaft with the frozen sleeve. This is followed by a range of amplitudes where unidirectional motion is observed. At still higher amplitudes, distortion of the shaft increases the potential energy barriers to levels higher than those that can be overcome by the electric field. Hence we get three regions during the amplitude scan, only one of which is useful for a nanomotor.

For a given amplitude, as the frequency is varied, more complex behavior is obtained, which can be broken up into four regions. At low frequencies (Region-1), large distortion of the shaft leads to an increase in potential energy barriers, hindering rotation. Over an intermediate range (Region-2), unidirectional motion is observed, since shaft distortions are smaller than in Region-1. This is followed by an anomalous region (Region-3), where resonant excitation of a characteristic mode of the shaft leads to very large distortions, which greatly enhance the barrier. Finally, in Region-4, the distortion again starts falling off with rise in frequency. However, the frequency is now so high that the shaft cannot complete a full rotation before the field reverse sign. Hence unidirectional rotation is not obtained. A detailed physical explanation has been provided for the anomalous behavior in Region-3, in terms of resonant excitation of a characteristic mode.

7.1.4 Molecular Dynamic simulations of a Carbon Nanotube interacting with a Graphite Surface

Depending upon the application, such a nanomotor should be attached to some surface, e.g. a metal surface. The next step must be to understand the interaction of these tubes with other surfaces. To explore such possibilities, as a first step we study the interactions of single-walled carbon nanotube with a graphite surface.

At a fixed temperature of 100 K, nanotubes of larger diameters are observed to acquire a large contact area on the top of the graphite surface. The tubes are seen to deform to have a larger contact area with the graphite surface and thus have larger binding energy with the surface. The variation of the binding energy per unit

length along the axis of the CNT, obtained from our MD calculations, matches well with the MM results of the other workers.

The contact area between the nanotube and the graphite surface is observed to become progressively smaller as the temperature is increased because at higher temperatures, the atoms acquire higher kinetic energies, because of which they can overcome the interactions between the tube and the graphite.

We also study the effect of the separation distance between neighboring nanotubes on the contact area between the tube and the graphite surface. All nanotubes having an intial separation greater than 6.9213 Å are observed to show qualitatively good flattening over the graphite surface.

7.2 Future Scope

The present work involves only classical MD simulations. The best way would be to do ab-initio MD simulations of a nanomotor while considering the following points:

- The addition of dopant charges to the shaft will change its electronic configuration and that can affect the behavior of the motor in presence of an external field. So the charge distribution should be computed self-consistently, and as a function of time. We have assumed point charges on only two atoms. Since we expect the charges to be produced by attached groups with different electronegativity, that would also imply a mass, which should be taken into account. Simple simulations done with the MOPAC code show that the attachment of a group leads to appearance of only a fractional charge not just on the specified carbon atom, but also, to a lesser extent, on the nearby atoms. This should be taken into account.

- Finally, the application of a strong electric field, and centrifugal forces during nanomotor operation, would lead to inter-atomic separations that vary in time. That implies that the charges arising due to polarization would also become time-dependent. Ideally, therefore, the charge distribution should be self-consistently evolved during the MD simulation.

- The high amplitude electric field used in our simulations would affect the inter-particle interactions which should be studied in detail.
- For practical applications, such a nanomotor would have joints when attached to a propeller. The behavior of the nanomotor should be studied in presence of such joints with the propeller.
- The present study of characteristic mode analysis of an SWNT and DWNT can be extended to more complex structures like one discussed above.
- For practical applications a nanomotor would likely be immersed in a fluid. Therefore the behaviour of the nanomotor should be studied in presence of a fluid, especially when the fluid enters the inter-CNT gap.

Appendix A

Energy and Pressure Conservation Checks

Before starting a real MD simulation the system is equillibrated at room temperature and pressure as explained in Chapter 2. This is done with an NPT simulation. This equilibration is required to adjust the system according to the potential energy expression used. While doing this equilibration we monitor the temperature of the whole system and see that it fluctuates around the desired 300 K as explained in the subsection 2.1.8.

Apart from monitoring the temperature of the system during these NPT simulations we do two more checks which are as follows:

- Energy conservation - Before starting a real MD simulation we confirm that the total energy of the system is conserved as shown in Fig. A.1(i).
- Pressure fluctuations - Like the total energy, the pressure of the system should also be constant in an NPT simulation. Fig.A.1(ii) shows the pressure variation of the total system during the entire simulation of 100 ps. It can be seen that the total pressure of the system fluctuates around zero throughout the whole NPT simulation.

Both the above mentioned checks were done during all NPT relaxation simulations, before starting a real NPT/NVE MD simulation.

(i)

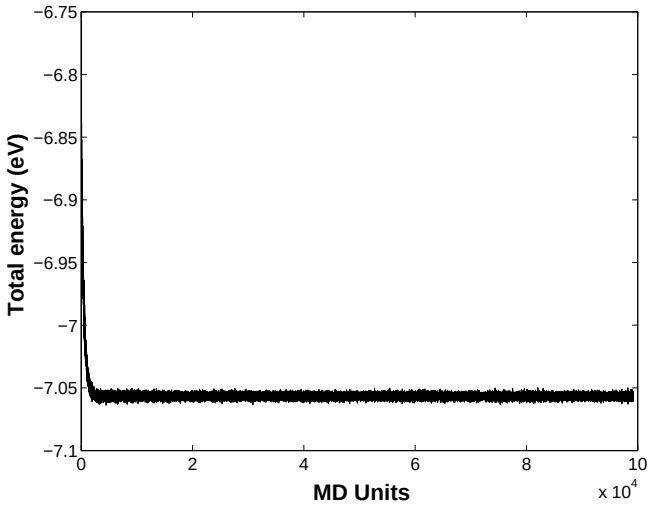

(ii)

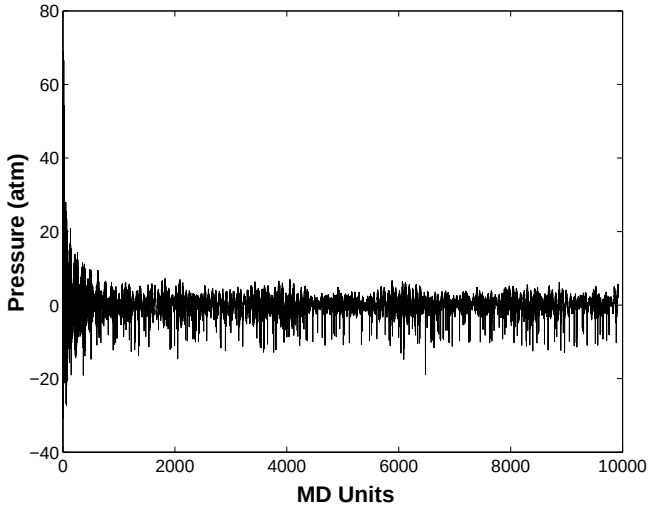

Figure A.1: (i) Temporal variation of the total energy of the system. (ii) Temporal variation of the pressure of the system during an NPT thermalization.

Appendix B

Time Step Calculation

One of the most important criteria in an MD simulation is choosing a right time step. Different type of simulations need different time steps but a general rule of thumb is followed in many cases as discussed in Chapter 2. Based on this rule of thumb we chose a time step of 0.1 fs in most of our simulations. But we chose a different time step for the determination of characteristic modes of the carbon nanotubes. This is because NVE simulations are performed for the determination of the characteristic modes of the carbon nanotubes and thus the total energy of the system should be conserved throughout the simulation. This selection was based on a energy conservation criteria as follows. The largest frequency present in the system is obtained by doing power spectral density (PSD) from the **X** coordinate of one of the atoms of the CNT as seen in Fig.4.1.

As explained in Chapter 4 this PSD shows that the power reduces by 10^{10} times at a frequency of 5×10^3 cm^{-1} and stabilizes after that. We take 10 times of this frequency as the Nyquist frequency so that we don't miss any other higher frequencies present in the system. This gives us a time step of 0.3 fs. It implies that a time step of less than 0.3 fs should give us a good energy conservation in the simulations. So we do energy conservation checks with NVE runs for 2 time steps of 1 fs and 0.2 fs. We monitor the temporal variation of total energy for both these runs. A monotonic variation in total energy is observed for the case with time step of 1 fs as shown in Fig.B.1(i) while the total energy of the system does not change upto second decimal place for a time step of 0.2 fs as shown in Fig.B.1(ii). Hence we perform all our NVE simulations for the characteristic mode determination with a time step of 0.2 fs.

(i)

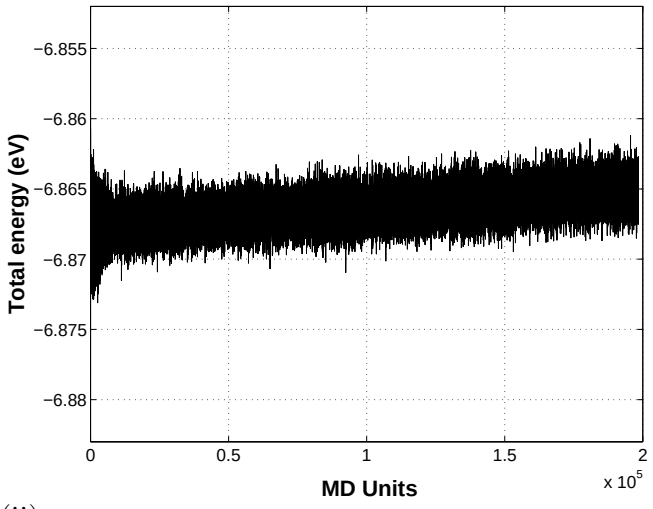

(ii)

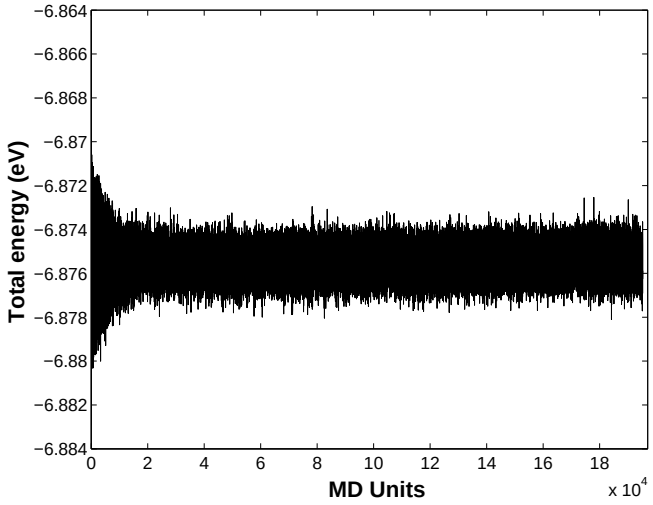

Figure B.1: (i) Temporal variation of the total energy of the system for a time step of 1 fs. A drift in the total energy of the system is clearly seen in this case. (ii) Temporal variation of the total energy of the system for a time step of 0.2 fs.

Bibliography

[1] S. Iijima, "Single shell carbon nanotubes of 1-nm diameter," *Nature*, vol. 354, pp. 56, (1991).

[2] Ray H. Baughman, Anvar A. Zakhidov, and Walt A. de Heer, "Carbon nanotubes–the route toward applications," *Science*, vol. 297, no. 5582, pp. 787–792, 2002.

[3] M. S. Dresselhaus et. al., "Carbon nanotubes synthesis, structure, properties, and applications," *Springer*, 2001.

[4] Kay Hyeok An, Won Seok Kim, Young Soo Park, Jeong-Mi Moon, Dong Jae Bae, Seong Chu Lim, Young Seak Lee, and Young Hee Lee, "Electrochemical properties of high-power supercapacitors using single-walled carbon nanotube electrodes," *Adv. Funct. Mater.*, vol. 11, no. 5, pp. 387–393, (2001).

[5] C. Niu, E. K. Sickel, R. Hoch, D. Moy, and H. Tennent, "High power electrochemical capacitors based on carbon nanotube electrodes," *Appl. Phys. Lett.*, vol. 70, no. 1480, (1997).

[6] C. Niu, J. Kupperschmidt, and R. Hock, ," *Proceedings of the 39th Power Sources Conference*, pp. 314–317, (2000).

[7] Ray H. Baughman, Changxing Cui, Anvar A. Zakhidov, Zafar Iqbal, Joseph N. Barisci, Geoff M. Spinks, Gordon G. Wallace, Alberto Mazzoldi, Danilo De Rossi, Andrew G. Rinzler, Oliver Jaschinski, Siegmar Roth, and Miklos Kertesz, "Carbon nanotube actuators," *Science*, vol. 284, no. 5418, pp. 1340–1344, (1999).

[8] Joseph Wang, "Carbon-nanotube based electrochemical biosensors: A review," *Electroanalysis*, vol. 17, no. 1, pp. 7–14, (2005).

[9] Seung Mi Lee, Ki Soo Park, Young Chul Choi, Young Soo Park, Jin Moon Bok, Dong Jae Bae, Kee Suk Nahm, Yong Gak Choi, Soo Chang Yu, Nam gyun Kim, Thomas Frauenheim, and Young Hee Lee, "Hydrogen adsorption and storage in carbon nanotubes," *Synthetic Metals*, vol. 113, pp. 209–216, (2000).

[10] Yuchen Ma, Yueyuan Xia, Mingwen Zhao, Ruijin Wang, and Liangmo Mei, "Effective hydrogen storage in single-wall carbon nanotubes," *PHYSICAL REVIEW B*, vol. 63, pp. 115422, (2001).

[11] Helena Dodziuk and Grigory Dolgonos, "Molecular modeling study of hydrogen storage in carbon nanotubes," *Chemical Physics Letters*, vol. 356, pp. 79–83, (2002).

[12] W. A. de Heer, A. Chatelain, and D. Ugarte, "A carbon nanotube field-emission electron source," *Science*, vol. 270, no. 5239, (1995).

[13] Andreas Thess, Roland Lee, Pavel Nikolaev, Hongjie Dai, Pierre Petit, Jerome Robert, Chunhui Xu, Young Hee Lee, Seong Gon Kim, Andrew G. Rinzler, Daniel T. Colbert, Gustavo E. Scuseria, David Tomnek, John E. Fischer, and Richard E. Smalley, "Crystalline ropes of metallic carbon nanotubes," *Science*, vol. 269, no. 1550, (1995).

[14] N. S. Lee, D. S. Chung, I. T. Han, J. H. Kang, Y. S. Choi, H. Y. Kim, S. H. Park, Y. W. Jin, W. K. Yi, M. J. Yun, J. E. Jung, C. J. Lee, You J. H, S. H. Jo, C. G. Lee, and J. M. Kim, "Application of carbon nanotubes to field emission displays," *Diamond Relat. Materials*, vol. 10, no. 2, pp. 265–270, (2001).

[15] Y. Saito and S. Uemura, "Field emission from carbon nanotubes and its application to electron sources," *Carbon*, vol. 38, no. 2, pp. 169–182, (2000).

[16] R. Rosen, W. Simendinger, C. Debbault, H. Shimoda, L. Fleming, B. Stoner, and O. Zhou, "Application of carbon nanotubes as electrodes in gas discharge tubes," *Appl. Phys. Lett.*, vol. 76, no. (1668), pp. 126130, 2000.

[17] H. Sugie, M. Tanemura, V. Filip, K. Iwata, K. Takahashi, and F. Okuyama, "Carbon nanotubes as electron source in an x-ray tube," *Appl. Phys. Lett.*, vol. 78, no. 2578, (2001).

[18] W. Zhu, C. Bower, O. Zhou, G. Kochanski, , and S. Jin, "Large current density from carbon nanotube field emitters," *Appl. Phys. Lett.*, vol. 75, no. 873, (1999).

[19] Jean-Marc Bonard, Thomas Stckli, Frdric Maier, Walt A. de Heer, and Andr Chtelain, "Field-emission-induced luminescence from carbon nanotubes," *Phys. Rev. Lett.*, vol. 81, no. 81, pp. 1441–1444, (1998).

[20] M. S. Fuhrer, J. Nygard, L. Shih, M. Forero, Young-Gui Yoon, M. S. C. Mazzoni, Hyoung Joon Choi, Jisoon Ihm, Steven G. Louie, A. Zettl, and Paul L. McEuen, "Crossed nanotube junctions," *Science*, vol. 288, no. 5465, pp. 494–497, (2000).

[21] Thomas Rueckes, Kyoungha Kim, Ernesto Joselevich, Greg Y. Tseng, Chin-Li Cheung, and Charles M. Lieber, "Carbon nanotube-based nonvolatile random access memory for molecular computing," *Science*, vol. 289, no. 5476, pp. 94–97, (2000).

[22] A. Bachtold, P. Hadley, T. Nakanishi, and C. Dekker, "Logic circuits with carbon nanotube transistors," *Science*, vol. 294, no. 5545, pp. 1317–1320, (2001).

[23] Robert E Tuzan, Donald W Noid, and Bobby G Sumpter, "Dynamics of a laser driven molecular motor," *Nanotechnology*, vol. 6, pp. 52–63, (1995).

[24] Deepak Srivastava, "A phenomenological model of the rotation dynamics of carbon nanotube gears with laser electric field," *Nanotechnology*, vol. 8, pp. 186–192, (1997).

[25] A. Lohrasebi and H. Rafii-Tabar, "Computational modeling of an ion-driven nanomotor," *Journal of Molecular Graphics and Modelling*, vol. 27, pp. 116–123, (2008).

[26] P. Gaspard J. Servantie, "Rotational dynamics and friction in double-walled carbon nanotubes," *Physical Review Letters*, vol. 97, pp. 186106, (2006).

[27] Jeong Won Kang and Ho Jung Hwang, "Gigahertz actuator of multiwall carbon nanotube encapsulating metallic ions : molecular dynamics simulation," *JOURNAL OF APPLIED PHYSICS*, vol. 96, no. 7, pp. 3900–3906, (2004).

[28] A.M. Fennimore, T.D Yuzvinsky, Wel-Qlang Han, M.S. Fuhrer, J. Cumings, and A. Zettl, "Rotational actuators based on carbon nanotubes," *Nature*, vol. 424, pp. 408–410, (2003).

[29] Bertrand Bourlon, D. Christian Glaattli, Csilla Miko, Laszlo Forro, and Adrian Bachtold, "Carbon nanotube based bearing for rotaional motions," *Nano Letters*, , no. 4, pp. 709–712, 2004.

[30] Jindong Tan Huaming Li, "Dynamic modeling and analysis of a swimming microrobot for controlled drug delivery," *Proceedings of the 2006 IEEE, International Conference on Robotics and Automation*, pp. 1768–1773, (2006).

[31] R. Saito, G. Dresselhaus, and M. S. Dresselhaus, "Physical properties of carbon nanotubes," *Imperial College Press*, (1998).

[32] Marie Brown, "Resonance raman spectroscopy of single-walled carbon nanotubes," *Massachusetts Institue Of Technology*, (2000).

[33] R. A. Jishi, L. Venkataraman, M. S. Dresselhaus, and G. Dresselhaus, ," *Chem. Phys. Lett.*, vol. 209, pp. 77–82, (1993).

[34] D. W Brenner, "Empirical potential for hydrocarbons for use in simulating the chemical vapour deposition of diamond films," *Phys. Rev. B*, vol. 42, pp. 9458, (1990).

[35] K. Nordlund, J. Keinonen, and T. Mattila, "Formation of ion irradiation induced small-scale defects on graphite surface," *Phys. Rev. Lett*, vol. 77, pp. 699, (1996).

[36] Yang Zhao, Chi-Chiu Ma, GuanHua Chen, , and Quing Jiang, "Energy dissipation mechanism in carbon nanotube oscillators," *Phys. Rev. Lett*, vol. 91, pp. 17, (2003).

[37] X. Sun, C.-H Kiang, M. Endo, K. Takeuchi, T. Furuta, and M. S Dresselhaus, "Stacking characteristics of graphene shells in carbon nanotubes," *Physical Review B*, vol. 54, pp. 18, (1996).

[38] Dominik Marx and Jurg Hutter, ," *Modern Methods and Algorithms of Quantum Chemistry*, vol. 3, pp. 329–477, (2000).

[39] Kai Nordlund, "Basics of md,initialization,time step choice,speedup methods," *http://beam.acclab.helsinki.fi/ knordlun/atomistiset/*, (2000).

[40] *http* : *//www.ch.embnet.org/MD*$_t$*utorial/pages/MD.Part*1.*html*, ," .

[41] J. Tersoff, "Modeling solid-state chemistry: Interatomic potentials for multi-component systems," *Physical Review B*, vol. 39, pp. 8, (1989).

[42] D. Porezag, Th. Frauenheim, Th. Kohler, G. Seifert, and R. Kaschner, "Construction of tight-binding-like potential on the basis of density-functional theory: Application to carbon," *Physical Review B*, vol. 51, no. 19, (1994).

[43] D. C Rappaport, "The art of molecular dynamics simulations," *Cambridge university press*, (1995).

[44] H. J. C. Berendsen, J. P. M. Postma, W. F. Van Gunsteren, A. DiNola, and J. R. Haak, "Molecular dynamics with coupling to an external bath," *J. Chem. Phys.*, vol. 81, no. 8, pp. 3684–3690, (1984).

[45] *http* : *//www.mpipmainz.mpg.de/andrienk/journalclub/thermostats.pdf*, ," .

[46] W. H. Press et. al., "Numerical recipes in fortran," *Cambridge University Press*, (1998).

[47] C. Nardone, "Multichannel fluctuation data analysis by the singular value decomposition method. application to mhd modes in jet," *Plasma Physics and Controlled Fusion*, vol. 34, no. 9, pp. 1447–1465, (1992).

[48] Robert E Tuzan, Donald W Noid, and Bobby G Sumpter, "The dynamics of molecular bearing," *Nanotechnology*, vol. 6, pp. 64–74, (1995).

[49] Harish M. Manohara, Michael J. Bronikowski, Michael Hoenk, Brian D. Huntand, and Peter H. Siegel, "High-current-density field emitters based arrays of carbon nanotube bundles," *J. Vac. Sci. Technol. B*, vol. 23, no. 1, (2005).

[50] Zhuang Liu, Scott Tabakman, Kevin Welsher, and Hongjie Dai, "Carbon nanotubes in biology and medicine: In vitro and in vivo detection, imaging and drug delivery," *Nano Res*, vol. 2, pp. 85–120, (2009).

[51] Jeong Won Kang and Ho Jung HWang, "Fluidic gas-driven carbon nanotube motor : Molecular dynamics simulations," *Journal of the Korean Physical Society*, vol. 45 (2), no. 573576, (2004).

[52] *http : //www.mse.ncsu.edu/CompMatSci/maketube.f*, ," .

[53] Jeno Kurti, Viktor Zolyomi, Miklos Kertesz, and Guangyu Sun, "The geometry and radial breathing mode of carbon nanotubes:beyond the ideal behaviour," *New Journal of Physics*, vol. 5, pp. 125, (2003).

[54] Merkle R C, "A proof about molecular bearings," *Nanotechnology*, vol. 4, pp. 86, (1993).

[55] S. Negi, M. Warrier, S. Chaturvedi, and K. Nordlund, "Molecular dynamics simulations of a double walled carbon nanotube motor subjected to a sinusoidally varying electric field," *Computational Material Science*, vol. 44, pp. 979–987, (2009).

[56] Shigeo Maruyama, "A molecular dynamics simulation of heat conduction in finite length swnts," *PHYSICA B*, vol. 323, pp. 193–195, (2002).

[57] Rols S., "Phd. thesis," *University of Montpellier II*, 2000.

[58] H. J. Liu and C. T Chan, "Properties of 4 åcarbon naotubes from first-principles calculations," *Physical Review B*, vol. 66, pp. 115416, (2002).

[59] A. M. Rao, E. Richter, Shunji Bandow, Bruce Chase, P. C. Eklund, K. A. Williams, S. Fang, K. R. Subbaswamy, M. Menon, A. Thess, R. E Smalley, G. Dresselhaus, and M. S Dresselhaus, "Diameter-selective raman scattering from vibrational modes in carbon nanotubes," *Science*, vol. 275, no. 187, (1997).

[60] S. Costa, E. Borowiak-Palen, M. Kruszynska, A. Bachmatiuk, and R. J. Kalenczuk, "Characterization of carbon nanotubes by raman spectroscopy," *Materials Science-Poland*, vol. 26, no. 2, (2008).

[61] R. Saito, T. Takeya, and T. Kimura, "Raman intensity of single-wall carbon nanotubes," *Physical Review B*, vol. 57, no. 7, (1997).

[62] Nachiket R. Raravikar, Pawel Keblinski, Apparao M. Rao, Mildred S. Dresselhaus, Linda S. Schadler, and Pulickel M. Ajayan, "Temperature dependence

of radial breathing mode raman frequency of single-walled carbon nanotubes," *Physical Review B*, vol. 66, pp. 235424, (2002).

[63] A. Kasuya, Y. Sasaki, Y. Saito, K. Tohji, and Y. Nishina, "Evidence for size-dependent discrete dispersions in single-wall nanotubes," *Phys. Rev. Lett.*, vol. 78, no. 23, pp. 4434–4437, (1997).

[64] Valentin N. Popov and Philippe Lambin, "Radius and chirality dependence of the radial breathing mode and the g-band phonon modes of single-walled carbon nanotubes," *Physical Review B*, vol. 73, no. 0855407, 2006.

[65] E. Dobardi, J. Maultzsch, I. Miloevi, C. Thomsen, and M. Damnjanovi, "The radial breathing mode frequency in double-walled carbon nanotubes: an analytical approximation," *Phys. stat sol.*, vol. 237, no. 2, (2003).

[66] Ludger Wirtz and Angel Rubio, ," *Solid State Communications*, vol. 131, pp. 141–152, (2004).

[67] V. A. Schweigert and F. Peeters, "Classical double-layer atoms: Artificial molecules," *Phys. Rev. B*, vol. 51, no. 7700, (1995).

[68] H. Kuzmany et. al, "Effect of dimensionality in polymeric fullerenes and single-wall nanotubes," *Physica B: Condensed matter*, vol. 244, pp. 186–191, 1998.

[69] A. Melzer, M. Klindworth, and A. Piel, "Normal modes of 2d finite clusters in complex plasmas," *Phys. Rev. Lett.*, vol. 87, no. 115002, (2001).

[70] A. Melzer, "Mode spectra of thermally excited two-dimensional dust coulomb clusters," *Phys. Rev. E*, vol. 67, no. 016411, (2003).

[71] R. Ichiki, Y. Ivanov, M. Wolter, Y. Kawai, , and A. Melzer, "Melting and heating of two-dimensional coulomb clusters in dusty plasmas," *Phys. Rev. E*, vol. 70, no. 066404, (2004).

[72] Yuriy Ivanov and Andr Melzer, "Melting dynamics of finite clusters in dusty plasmas," *PHYSICS OF PLASMAS*, vol. 12, no. 072110, pp. 1–11, (2005).

[73] S. Negi and S. Chaturvedi, "Normal mode analysis of a single walled carbon nanotube based on molecular dynamics : A singular value decomposition study," *International Journal of Nanoscience*, vol. 9, pp. 1–16, (2010).

[74] A. Bezryadin, A. R. M. Verschueren, S. J. Tans, and C. Dekker, "Multiprobe transport experiments on individual single-wall carbon nanotubes," *Phys. Rev. Lett*, vol. 80, pp. 4036, (1998).

[75] A. Rochefort, D. R Salahub, and Ph. Avouris, "Effects of finite length on the electronic structure of carbon nanotubes," *Chem. Phys. Lett.*, vol. 103, no. 4, pp. 641–646, (1999).

[76] Tobias Hertel, Robert E. Walkup, and Phaedon Avouris, "Deformation of carbon nanotubes by surface van der walls forces," *Phys. Rev. B*, vol. 58, no. 20, pp. 13870–13873, (1998).

[77] J. W. Ponder and F. M. Richards, "An efficient newton-like method for molecular mechanics energy minimization of large molecules," *J. Comput. Chem.*, vol. 8, pp. 1016, (1987).